MEASUREMENT OF $W + \gamma$ PRODUCTION IN PROTON-ANTIPROTON COLLISIONS AT $\sqrt{s} = 1.96$ TEV

by

Michael H Kirby

Department of Physics
Duke University

Date:_____

Approved:

_____

Dr. Alfred T. Goshaw, Supervisor

_____

Dr. Thomas J. Phillips

_____

Dr. Harold U. Baranger

_____

Dr. Ashutosh V. Kotwal

_____

Dr. M. Ronen Plesser

Dissertation submitted in partial fulfillment of the
requirements for the degree of Doctor of Philosophy
in the Department of Physics
in the Graduate School of
Duke University

2004

ABSTRACT

(Physics - High Energy)

MEASUREMENT OF $W + \gamma$ PRODUCTION IN PROTON-ANTIPROTON COLLISIONS AT $\sqrt{s} = 1.96$ TEV

by

Michael H Kirby

Department of Physics
Duke University

Date:_____
Approved:

_____
Dr. Alfred T. Goshaw, Supervisor

_____
Dr. Thomas J. Phillips

_____
Dr. Harold U. Baranger

_____
Dr. Ashutosh V. Kotwal

_____
Dr. M. Ronen Plesser

An abstract of a dissertation submitted in partial fulfillment of
the requirements for the degree of Doctor of Philosophy
in the Department of Physics
in the Graduate School of
Duke University

2004

Abstract

We present a measurement of the $\bar{p}p \to W\gamma + X \to e\nu\gamma + X$ production cross section using data from the Collider Detector at Fermilab. The $p\bar{p}$ collisions were provided by the Tevatron Collider at a center of mass energy of 1.96 TeV. Electroweak theory includes the trilinear vector boson coupling, $WW\gamma$, which contributes to the $e\nu\gamma$ final state. The electron decay channel of the W provides a clean sample to study the production of diboson pairs. The measurement of the production cross section tests the structure of the non-Abelian character of Electroweak theory.

The data presented is from approximately 200 pb^{-1} of integrated luminosity collected with the upgraded Collider Detector Facility at the Fermilab Tevatron. The electron decay products of Ws are selected in the central ($|\eta_e| < 1.0$) and forward ($1.2 < |\eta_e| < 2.6$) detector regions, and a well-separated, isolated photon ($|\eta_\gamma| < 1.0, E_T^\gamma > 7$ GeV, $\Delta R(e, \gamma) > 0.7$) is required for an event to be selected as a $W\gamma$ candidate. 131 central electron candidates are observed, with 64 candidate events found with forward electrons.

We calculate a Standard Model prediction for $\bar{p}p \to W\gamma + X \to e\nu\gamma + X$ using generated events from a Leading Order (LO) $W\gamma$ calculation and a detailed detector simulation. Using an $\mathcal{O}(\alpha_s)$ $W\gamma$ calculation, a correction is applied to the LO production to account for QCD corrections to $W\gamma$ production. The Standard Model prediction for the $\bar{p}p \to W\gamma + X \to e\nu\gamma + X$ cross section for $E_T^\gamma > 7$ GeV and $\Delta R(e, \gamma) > 0.7$ is 19.3 ± 1.4 pb.

The background to the $W\gamma$ signal comes from jets faking photons in W events and from Standard Model processes. A jet $\rightarrow$ photon fake rate is determined in the data and then applied to the $W+jets$ data to estimate the background contribution. The contribution of the two processes, $W\gamma \rightarrow \tau\nu\gamma \rightarrow e\nu\nu\nu\gamma$ and $Z\gamma \rightarrow ee\gamma$, is calculated using Standard Model theory and a simulated detector response. We calculate the central electron background to be 32.1% of the expected events and the forward electron background to be 39.5% of the expected events.

The measured cross section for $\bar{p}p \rightarrow W\gamma + X \rightarrow e\nu\gamma + X$ in the kinematic region ($E_T^\gamma > 7$ GeV and $\Delta R(e, \gamma) > 0.7$) is 20.1 $\pm$ 3.9 pb in the central electron sample and 18.4 $\pm$ 5.2 pb in the forward electron sample. Combining this result with the results of a $W\gamma \rightarrow \mu\nu\gamma$ analysis gives a measured $W\gamma \rightarrow l\nu\gamma$ cross section of 18.1 $\pm$ 3.1 pb. We compare the kinematic distributions for the candidate events with the Standard Model and find them in good agreement.

Dedicated to my family, Linda, David, and Jennifer.

Acknowledgements

I would like to thank my family first and foremost. David, Linda, and Jennifer, you have provided me with all of the love, support, and encouragement I could have ever wanted and more. Through all of the years of missed calls, missed birthdays, and missed holidays, your understanding has been amazing. I owe you more than I can repay. Thank you, and I love you.

Lauren, words cannot express the gratitude that I owe you. You helped me through the darkest time of my life, reminded me how cool physics is, and inspired me to strive to greatness. I can honestly say that I would have never accomplished this thesis without you in my life.

I thank my advisor Al Goshaw for his guidance, teaching, and support during the completion of this analysis. Our conversations about physics inspired me even more than our discussions of Duke basketball. You on more than one occasion showed me that sitting down with pencil and paper is still the best way to understand and learn physics.

I would also like to thank my advisor Thomas Phillips for all of the help on this thesis and while working on the COT. The time that I spent understanding the details of getting the detector to work have been invaluable.

Thanks to the best working group ever: Beate Heinemann, Naho Tanimoto, and Helen Hayward. I only hope that in the future I get a chance to work with physicist who are as dedicated, smart, and as good of friends as all of you.

A huge thanks goes to Doug Benjamin, Heather Gerberich, Chris Hays, Ashutosh Kotwal, and Pete Tamburello, who as part of the Duke group, helped me to understand what it was I was doing, and made coming into work a pleasure. Thanks to Sebastian Carron and Dean Hidas for sharing a cubicle with me and putting up with me. Heather, thanks for letting me dog sit for you. Thanks to Chris Hays and Chris Neu for letting me sit in on Quarterback Club, and helping me to become a Sox fan no matter the color. Thanks to Bill Orejudos for all the help with the TDCs. Thanks to Mike Hornish for hosting me during Duke basketball games and taking me to the Green Room.

To my housemates: Andy Haas, Mike Mulhearn, Marumi Kado, Kenichi Hatakeyama, and Kike Palencia. Thanks for all of the great times at the Compound. Thanks especially to Leon and Ellen Lederman for letting us live in their amazing house, and for the hospitality in Idaho. It was a time I will never forget.

To Dinner Club: Andy, Olga, Daniel, Katrine, Ben, Florencia, Giulia, Rolf, Nate, Kathy, Cigdem, Eva, Chris, Liz, Mike, Mila, Greg, Mila, Sondra. My time in Chicago has been blessed with phenomenal friends, and sharing my life and experiences with you all has been a true joy.

To Jen Raaf: you always helped me to keep sane, to realize when I was being an idiot, and to remember how to spell. Thank you for your amazing friendship, now just quit following me.

And thanks Dan for: getting passed by your muffler, helping work on the kart brakes, and all the time spent racing. Without all this I'm sure I would have graduated years earlier, but then I would not have Bessie.

Thanks to all of the support staff in the Duke Physics department, especially

Pat Hoyt who kept all of us "missing" grad students connected and in line. Thanks also to the support staff and technicians at CDF who make sure that the detector doesn't suffer too greatly at the hands of the physicists.

Contents

List of Figures

List of Tables

xxiv

Chapter 1

Introduction

The quest to understand the fundamental constituents of the universe is a human endeavor more than two millennia old. While theories have abounded throughout this time, a significant milestone was achieved at the end of the 19th century with the discovery of the electron by Thompson. This first "elementary" particle marked the beginning of an era of experimental discovery using naturally occurring cosmic rays and radioactive sources. But the experimental power of such natural sources was quickly realized, and in 1927 Ernest Rutherford called for "a copious supply" of particles more energetic than naturally occurring particles [1]. With the development of the cyclotron [2] in the 1930s, the possibility of probing matter with a high-intensity, high-energy particle beam became a reality. Since that time, experiments have sought to explore matter using higher and higher energy particle beams. And with higher energy, experiments are able to probe smaller and smaller distances and identify finer structure within matter. Currently, the Tevatron is the highest energy particle accelerator that is used to explore the structure and interactions of matter.

The elementary particles in nature are divided into two groups: fermions and bosons. Fermions have half-valued intrinsic angular momentum, or spin, and it is these particles (quarks and leptons) that are the constituents of all matter. Each of

1

these fermions has a corresponding anti-particle with identical mass, but opposite
quantum numbers. The other set of elementary particles, bosons, have integer spin,
and the exchange of a characteristic boson mediates interactions between particles.
The interactions of these particles are described by four forces: electromagnetic,
weak, strong, and gravitational. The first three of these forces are described by the
Standard Model [3], the most prevalent physical theory for describing elementary
particles and their interactions.

1.1 Elementary Particles

The six leptons observed in nature are grouped into three "generations" with each
charged lepton paired with its corresponding neutrino. The generation and prop-
erties of each lepton are shown in Table 1.1 [4]. Leptons carry a quantum number
associated with its generation, $e.g.$ the electron has $L_e = 1$ and the positron $L_e = $
-1. Prior to recent results from neutrino experiments, this quantum number was
believed to be conserved in all interactions. It now appears that within the neutrino
sector, there can be mixing or oscillations between the three neutrino generations.

Table 1.1: Properties of leptons. The spin, charge (e), mass (MeV/c^2), and anti-
particle (AP) are listed for each particle.

	Particle	Spin	Q (e)	Mass (MeV/c^2)	AP
1st generation	e^-	1/2	-1	0.510998901± 0.000000044	e^+
	ν_e	1/2	0	< 0.003	$\bar{\nu}_e$
2nd generation	μ^-	1/2	-1	105.6583692±0.0000094	μ^+
	ν_μ	1/2	0	< 0.19	$\bar{\nu}_\mu$
3rd generation	τ^-	1/2	-1	1776.99±0.29	τ^+
	ν_τ	1/2	0	< 18.2	$\bar{\nu}_\tau$

The other group of fermions, quarks, are also grouped into three generations with six different quark flavors. The generations and properties of each quark are shown in Table 1.2. Quarks have never been observed as "free" particles in nature. With the exception of the top quark, quarks are always found in bound states (hadrons) of either two quarks (mesons) or three quarks (baryons). The top quark is unique, because when produced in high energy collisions it decays before hadronization. This effect is due to the large mass of the top, ≈ 175 GeV/c^2. This property of the top quark allows for a direct measurement of its mass, while the mass of the other quarks must be measured indirecty. These indirect mass measurements result in large errors on the lightest five quark masses. As with the leptons, the quarks carry a quantum number based upon their flavor ("strangeness","charm", etc.). This quantum number is conserved in all strong interactions but is not conserved for weak interactions.

Table 1.2: Properties of quarks. The spin, charge (e), current mass (MeV/c^2), and anti-particle (AP) are listed for each particle. Additionally, each quark flavor carries three colors (red, green, blue) from Quantum Chromodynamics which is discussed later in this chapter.

	Particle	Spin	Q (e)	Mass (MeV/c^2)	AP
1st generation	u	1/2	+2/3	1.5 - 4.0	$\bar{u}$
	d	1/2	-1/3	4 - 8	$\bar{d}$
2nd generation	c	1/2	+2/3	1150 - 1350	$\bar{c}$
	s	1/2	-1/3	80 - 130	$\bar{s}$
3rd generation	t	1/2	+2/3	174300$\pm$5100	$\bar{t}$
	b	1/2	-1/3	4100 - 4400	$\bar{b}$

The bosons, or integer spin particles, are the propagators of the four forces mentioned previously. The bosons are the photon (γ), the neutral weak boson (Z), the charged weak boson (W), gluons (g), and the graviton. The photon transmits

the electromagnetic force, the W and Z particles mediate the weak force, and the gluons propagate the strong force. The familiar gravitational force is believed to be mediated by the exchange of gravitons, although no consistent quantum theory of gravity exists currently. The existence of all the bosons have been confirmed experimentally except for the graviton. A summary of the bosons and their properties is given in Table 1.3.

Table 1.3: The elementary bosons. These particles mediate the four fundamental forces: electromagnetic, weak, strong, and gravitational.

Boson	Force	Spin	Mass[GeV/c^2]	Q[e]	Range[fm]
γ	Electromagnetic	1	$< 6 \times 10^{-23}$	0	∞
W	Charged Weak	1	80.425 ± 0.038	± 1	$\approx 10^{-3}$
Z	Neutral Weak	1	91.1876 ± 0.0021	0	$\approx 10^{-3}$
g	Strong	1	0^1	0	$< \sim 1$
Graviton	Gravity	2	0	0	∞

1.2 Elementary Forces

The four known forces in nature are the electromagnetic, weak, strong and gravity. The electromagnetic force affects any particle that carries electric charge and is described by Quantum Electrodynamics (QED). The weak force in kind affects particles that carry weak charge. In the 1960's, the electromagnetic and weak forces were unified by Glashow, Salam, and Weinberg [5] into a single electroweak theory propogated by the photon, W, and Z gauge bosons. The unified electroweak theory is described by the gauge group $SU_L(2) \times U_Y(1)$, where L represents the left-handed weak isospin group and Y represents hypercharge. The other completely described

---

[1]Theoretical value. A gluon mass of a few MeV may not be precluded.

force is quantum chromodynamics (QCD) which characterizes the strong force between quarks by the $SU_c(3)$ gauge group. The combination of the electroweak and strong forces is commonly referred to as the Standard Model. The codification of these theories into the Standard Model is based strongly on the work of Feynman, Schwinger, and Tomonaga in developing the quantum gauge theory of electrodynamics (QED) [6]. The last of the four forces is gravity, which is described classically by General Relativity. Because the masses of the individual particles are so small, gravitational effects can be ignored in collider interactions. It has yet to be shown how a quantum theory of gravity can be successfully unified with the other forces of the Standard Model. While all forces are of great consequence within the universe, the electroweak force dominates the diboson production studied in this thesis. The Standard Model theory of $e\nu\gamma$ production will be discussed in detail after a survey of the Electroweak and Strong forces.

1.3   Electroweak Interactions

Electroweak theory is an example of a Yang-Mills gauge field theory [7] that unifies the electrodynamic (QED) and weak interactions. The unified theory is a locally gauge invariant quantum field theory with a $SU_L(2) \times U_Y(1)$ symmetry. Prior to unification, the electromagnetic group has a $U_Q(1)$ symmetry generated by electric charge, Q. The weak group has a $SU_L(2)$ symmetry from the charged and neutral current interaction, where L signifies that the weak bosons couple only to left-handed fermions. Handedness refers to the orientation of the particle's intrinsic spin in relation to the particle's momentum. For massless left-handed particles, the spin is opposite the momentum. In order to preserve the $SU_L(2)$ symmetry when constructing the isospin triplet of weak currents, it becomes necessary to modify

the $U(1)$ electromagnetic group generator to account for right-handed interactions. The new weak hypercharge, Y, is introduced and replaces electric charge as the group generator. Y is defined from

$$Q = T_3 + \frac{Y}{2} \tag{1.1}$$

where Q is the electric charge and T_3 the third component of the weak isospin of the particle. The electric charge, weak isospin, the isospin projection, and hypercharge of fermions and bosons are shown in Table 1.4. The electroweak theory is then based around the conservation of weak isospin and hypercharge, with the Lagrangian invariant under the local gauge transformation $SU_L(2) \times U_Y(1)$.

Table 1.4: The Electroweak quantum numbers for the fermions and bosons. The electric charge, (Q), weak isospin (T), its projection (T_3), and weak hypercharge $(Y)$are listed. The fermions are divided between quarks and leptons where the subscript denotes if the particle is right-handed or left-handed. The electroweak bosons are listed, but the propagators of the strong force (gluons) have been excluded since they have no electroweak interactions.

Particle	Q	T	T_3	Y
u_L, c_L, t_L	+2/3	1/2	+1/2	+1/3
d_L, s_L, b_L	-1/3	1/2	-1/2	+1/3
u_R, c_R, t_R	+2/3	0	0	+4/3
d_R, s_R, b_R	-1/3	0	0	-2/3
e_L^-,μ_L^-,τ_L^-	-1	1/2	-1/2	-1
ν_e,ν_μ,ν_τ	0	1/2	+1/2	-1
e_R^-,μ_R^-,τ_r^-	-1	0	0	-2
W^+	+1	1	+1	0
W^-	-1	1	-1	0
Z	0	1	0	0
γ	0	0	0	0

The gauge invariance of the Electroweak Lagrangian is complicated by the fact

that the weak gauge bosons $(W^\pm, Z)$ have non-zero masses. The addition of the simplest mass term of the form $-m\bar{\psi}\psi$ to the Lagrangian introduces terms that are not gauge invariant. To overcome this limitation, the mechanism of spontaneous symmetry breaking [8] is introduced using four real scalar fields. This new potential generates a particle, the Higgs boson (the only unconfirmed particle of the Standard Model). The Higgs mechanism then generates the large masses for the weak gauge bosons ($m_W \approx 80$ GeV/c^2, $m_Z \approx 91$ GeV/c^2) due to the large coupling of the bosons to the Higgs. The large masses for the weak bosons explains the shorter range of the weak force.

1.4 Quantum Chromodynamics

Quantum Chromodynamics (QCD) describes the interaction between color charged particles. Within QCD, there are three charges (Red, Green, and Blue) that are carried by quarks and gluons. Each quarks carries a single color, and with three colors there are actually three quarks of each flavor (*i.e.* red up, blue up, and green up) for a total of 18 quarks. The interactions between the color carrying quarks are mediated by the exchange of bicolored gluons. The octet of possible gluons is $(R\bar{G}, R\bar{B}, G\bar{R}, G\bar{B}, B\bar{R}, B\bar{G}, \sqrt{\frac{1}{2}}(R\bar{R} - G\bar{G}), \sqrt{\frac{1}{6}}(R\bar{R} + G\bar{G} - 2B\bar{B}))$. The color singlet does not contribute to strong interactions since it does not carry color and is unable to mediate forces between color charges.

One of the critical principles of strong interactions is the conservation of color charge. While the flavor of a quark cannot change in strong interactions, the color of each quark may change by emission of a gluon, but the color of the entire system is conserved. In order to accomplish this conservation theoretically, the QCD Lagrangian is constructed to be invariant under both global and local gauge trans-

formations. For global gauge invariance the interactions must be unchanged after a constant phase is added to the particle wave function, $\psi \to e^{i\phi}\psi$. Local gauge invariance is constructed by allowing the phase from point to point to vary with the Lagrangian remaining the same. With these two constructs contained within QCD theory, color charge is conserved in all interactions.

Since the QCD propagator is a massless boson, the short range of the strong force must be explained from other properties of the theory. The potential for strong interactions at short distances ($r \leq 0.1$ fm) is given by

$$V(r) = -\frac{4}{3}\frac{\alpha_s}{r} \tag{1.2}$$

The separation between the two color charged particles is given by r, and α_s is the strong coupling constant. But the strong coupling constant is not a constant value, but scales depending upon the momentum exchange between the color charged particles. α_s can be written as [9]

$$\alpha_s(Q^2) = \frac{12\pi}{(33 - 2n_f)log(\frac{Q^2}{\Lambda^2})} \tag{1.3}$$

Here n_f is the number of quark flavors, Q^2 the momentum transfer between the particles, and Λ is the renormalization scale. The scale Λ must be determined by experiment and has been measured to be approximately 200 MeV. The strong coupling constant then becomes small for large momentum transfer ($\alpha_s \to 0$ as $Q^2 \to \infty$), and a perturbative description of the strong force in term of quarks and gluons is possible. When Q^2 is of the same order as Λ, this perturbative description is no longer valid as the quarks and gluons have organized into strongly bound hadrons. Then, from the running value of the strong coupling constant,

the asymptotic freedom of quarks at short distances and strong binding at large distances (quark confinement) is understood.

For larger separations of quarks ($r \geq 0.1$ fm), the strong potential changes as gluon self coupling begins to dominate. This new form of the potential is a linear function, $V(r) \approx \lambda r$. Here, λ is a constant on the order of 1 GeV/fm. When two quarks become separated by a large enough distance, it is energetically more favorable that a quark-antiquark pair be produced from the vacuum. These newly produced quarks will then form colorless hadrons with the original quark pair. This linear potential for large separation and the strong quark confinement at short distances conspire so that quarks are always contained within hadrons. Therefore, no bare color exists in a stable state and only colorless objects are observed in nature. The combination of colors in baryons is colorless, and contains color charges of either RGB or $\bar{R}\bar{G}\bar{B}$. The configurations of charges in mesons combine to be colorless in the form of $R\bar{R}$, $G\bar{G}$, or $B\bar{B}$.

Using QCD and Electroweak theory, $q\bar{q} \rightarrow W\gamma + X$ production can be described. A detailed discussion of the production is presented in Chapter 2. This thesis measures $W\gamma + X$ production using proton-antiproton collisions. Since the proton and antiproton are composite particles, in order to be able to theoretically calculate this interaction, the internal structure of the proton and antiproton must be considered. This requires modeling the kinematics of elementary particles within the proton. These elementary particles are referred to as partons, and the parton distribution function for the proton and antiproton are discussed in the next section.

1.5 Parton Distribution Functions

The interactions between two baryons must be described using parton distribution functions. A high momentum baryon is comprised of a collection of partons, and the energy distributions of these partons are described by parton distributions functions (PDF). For this analysis, the baryons of interest are the proton and antiproton. The partons within a proton or antiproton are the valence quarks, gluons and sea quarks. The valence quarks are the bound-state quarks that define the quantum numbers of the baryon, while sea quarks are a virtual quark-antiquark pair produced from the splitting of a gluon.

The PDF gives the probability that a specific parton will have a fraction, x, of the baryon momentum. Then for an interaction between two partons, the square of the scattering partons energy is $x_1 \cdot x_2 \cdot s$, where s is the square of the center-of-mass energy of the colliding particles. For collisions at the Fermilab TeVatron between protons and antiprotons, each of the incident baryons has as energy of 980 GeV. The square of the center-of-mass energy is $(1.96 \text{ TeV})^2$ and the square of the energy between the two interacting partons in a collision given by

$$\hat{s} = x_1 \cdot x_2 \cdot (1.96 \ TeV)^2 \tag{1.4}$$

The structure of the proton that dominates any interaction is dependent upon the energy regime of the probe. The characteristic length of any probe may be calculated as the de Broglie wavelength from

$$\lambda = \frac{hc}{p} \tag{1.5}$$

Here, p is the momentum transfer, q, of the interaction. In the low energy regime (< 1 GeV), the proton interacts predominantly as a single particle. At medium energy (< 100 GeV), the composite nature of the proton is apparent, and the valence quarks make the largest contribution to the interaction probed (uud for the proton). At higher energy, the probability distribution function is dominated by gluons and sea quarks. The electroweak interactions measured in this thesis require a momentum transfer near the W mass ($\approx 80 \, \mathrm{GeV/c}^2$). From the previously defined equation, this limits the value of $x_1 \cdot x_2$ to greater than 0.0017, or x greater than 0.04 in a symmetric collision. For these values of x, the production of electroweak interactions will be dominated by contributions from valence quarks.

The probability distribution functions must obey several normalization rules. The function, $f_a^p(x, q^2)$, gives the probability that a parton of flavor a within the proton will have the momentum fraction x for momentum transfer in the interaction of q^2. The function, $f_a^{\bar{p}}(x, q^2)$, is the mirror case for an antiproton. Since the proton is constructed of two valence u quarks, the integral of the u and $\bar{u}$ distribution must be equal to 2. This is shown symbolically as

$$\int_0^1 [f_u^p(x, q^2) - f_{\bar{u}}^p(x, q^2)]dx = 2 \tag{1.6}$$

As well, with one d valence quark in the proton

$$\int_0^1 [f_d^p(x, q^2) - f_{\bar{d}}^p(x, q^2)]dx = 1 \tag{1.7}$$

The contribution of the anti-particles in these equations come from sea quarks generated in gluon splitting. Corresponding rules apply to the parton distribution function of the antiproton which is constructed of $\bar{u}\bar{u}\bar{d}$. Finally, the total contribu-

tion of the momentum fraction of all parton flavors must be unity.

$$\sum_a \int_0^1 x f_a^p(x, q^2) dx = 1 \tag{1.8}$$

where a is u, d, c, s, t, b and the corresponding anti-particles. The proton PDF used is this analysis is shown in Figure 1.1.
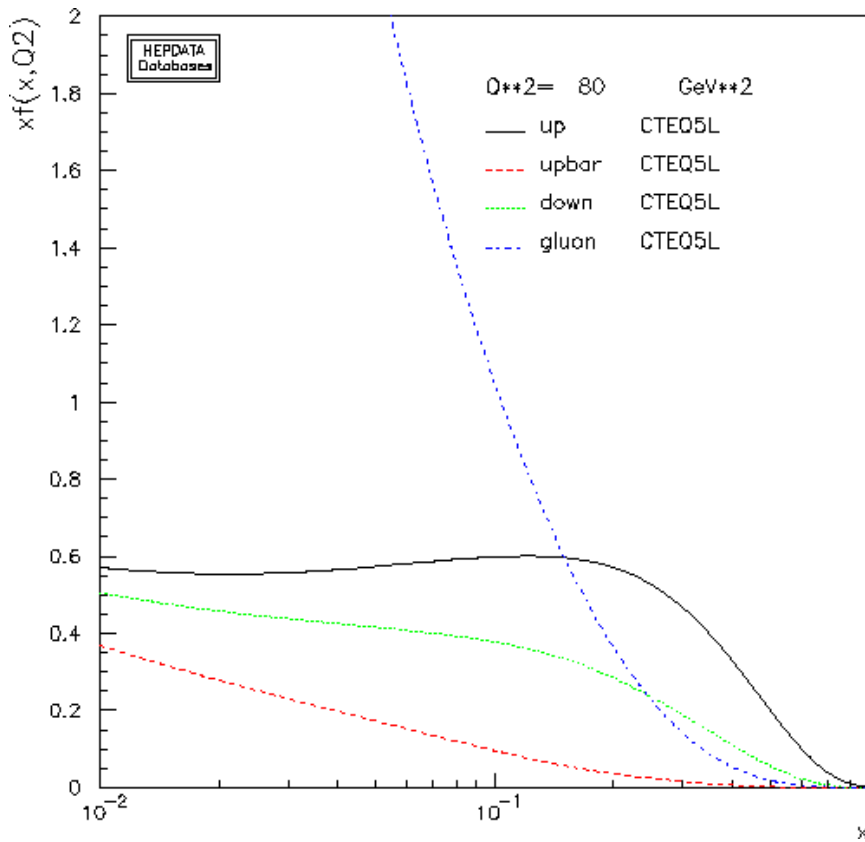
Figure 1.1: The CTEQ5L parton distribution for the proton [40]. The contribution from u, d, and $\bar{u}$ quarks are shown along with the gluon contribution. For x values above $\approx$0.15, valence quarks dominate the distribution and are the largest contribution to hard interactions involving the proton.

Any specific parton distribution function is a multi-parameter fit to a large number of experiments (see discussion in [10]). A comparison of three fits for the u

and d contributions to the proton parton distribution functions are shown in Figure 1.2 and the effect of this variations on the Standard Model prediction is discussed in Chapter 6.
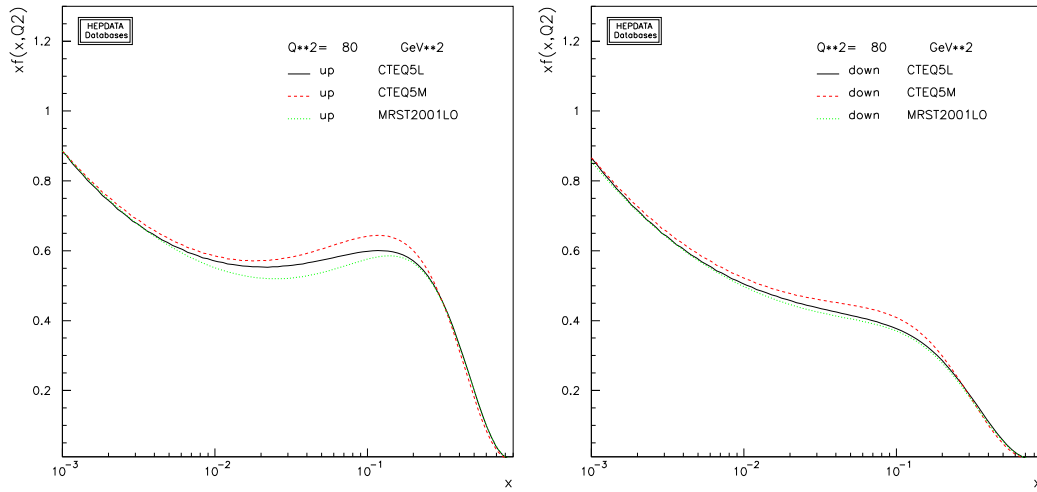
Figure 1.2: A comparison of the u and d quark contributions to the proton parton distribution function for three different parameterizations (CTEQ5L, MRST2001, and CTEQ5M [40, 43]). The first two parton distribution functions are based upon Leading Order parameterizations to data while the third is a Next-to-Leading Order parameterization. Leading Order or Next-to-Leading Order refers to the number of Feynman diagrams included in the calculation, with Leading Order containing only tree-level terms.

To calculate the cross section of an interaction between a proton and antiproton, all of the different parton flavors and momenta must be weighted by the parton distribution function and integrated over all phase space. For a two-body parton interaction $(ab \rightarrow cd)$, there will be two weighting factors from the appropriate PDF. The differential cross section of the interaction $ab \rightarrow cd$ is given by

$$d^2\sigma(ab \rightarrow cd) = \hat{\sigma}(ab \rightarrow cd)f_a^p(x_1, q^2)f_b^{\bar{p}}(x_2, q^2)dx_1 dx_2 \tag{1.9}$$

Here $\hat{\sigma}$ is the matrix element cross section for the parton interaction $ab \rightarrow cd$. The full cross section for a proton-antiproton interaction $p\bar{p} \rightarrow cd$ is calculated by the sum over all quark flavors $(u, d, c, s, t, b, \bar{u}, \bar{d}, \bar{c}, \bar{s}, \bar{t}, \bar{b})$ and integral over all momenta $(x_1$ and $x_2)$ shown here:

$$\sigma(p\bar{p} \rightarrow cd) = \sum_a^p \sum_b^{\bar{p}} \int_0^1 \int_0^1 d^2\sigma(ab \rightarrow cd) \qquad (1.10)$$

Using these parton distribution functions, the composite structure of the proton and antiproton are accounted for when predicting the interactions in hadron collisions.

In this thesis, the process $p\bar{p} \rightarrow W\gamma + X$ is studied in the $W \rightarrow e\nu$ decay channel. This process provides a measure of the interaction between the W and γ bosons which are themselves force carriers in nature. The interaction in the $W\gamma$ system provides an opportunity to probe for new physics while measuring a precisely described interaction in the Standard Model. Anomalous $W\gamma$ production would suggest the possibility of internal structure or an excited state of the W. Using Standard Model theory, precise predictions are made for the production rate and kinematics of the interactions. The details of the Electroweak theory describing this interaction are presented in the next chapter, and a survey of experimental measurements of boson self couplings is presented in Chapter 3. A description of the experimental apparatus used to produce the $p\bar{p}$ collisions and detect the resulting particles is then given. Next, the details of the $e\nu\gamma$ event selection, predicted event rate, and backgrounds are presented. Finally, the measured cross section for $W\gamma$ events is presented along with a discussion of comparison to the Standard Model prediction.

Chapter 2

Standard Model $W\gamma$ Production

After spontaneous symmetry breaking and the addition of at least one scalar boson, H^0, the Standard Model electroweak theory contains a single massless vector boson, γ, and three massive vector bosons, $W^\pm$ and Z. These bosons are the propagators of the electromagnetic current and the weak charged and neutral currents, respectively. That the weak field is non-Abelian is of interest since this leads to the electroweak prediction of boson self-couplings.

The most general gauge invariant Lagrangian for boson self-couplings is [11]

$$L_{vector} = -\frac{1}{4}W_{i\mu\nu}W^{i\mu\nu} - \frac{1}{4}B_{\mu\nu}B^{\mu\nu} \tag{2.1}$$

where

$$W_{i\mu\nu} \equiv \partial_\mu W_{i\nu} - \partial_\nu W_{i\mu} - g\epsilon_{ijk}W_\mu^j W_\nu^k \tag{2.2}$$

$$B_{\mu\nu} \equiv \partial_\mu B_\nu - \partial_\nu B_\mu \tag{2.3}$$

Here W_i is the ith component of the non-Abelian weak current and B is the Abelian electromagnetic current. g is the weak coupling constant, and ϵ_{ijk} is the completely anti-symmetric unit tensor. This term contains both the triple and quartic gauge boson couplings such as $WW\gamma$, ZWW, $WWWW$, and $WWZ\gamma$. While indirect limits on these couplings are possible from high-precision measurements, these lim-

its are model dependent. The direct measurement of these self-coupling terms would help to confirm that the electroweak group is described by a spontaneously broken, non-Abelian theory. This thesis focuses on the measurement of $WW\gamma$ production and the comparison of the measured distributions with the Standard Model predictions.

2.1 $W\gamma$ Couplings

$W\gamma$ production occurs through several mechanisms, and for the W electron decay channel the tree-level Feynman diagrams are shown in Figure 2.1. Feynman diagrams show particle interactions graphically, but each diagram also represents an individual amplitude in the complete matrix element calculation. The diagram of greatest interest is the s-channel diagram since it contains the triple gauge coupling $WW\gamma$. The u- and t-channel diagrams represent initial state photon radiation from the incident quark or anti-quark respectively. Additionally, final state radiation, or inner bremsstrahlung, from the W decay products also contributes to the lepton-neutrino-photon final state. In order to ensure gauge invariance, all four terms must be summed coherently when calculating the matrix element.

The generalized gauge invariant Lagrangian for the $WW\gamma$ vertex can be written as

$$
\begin{aligned}
L_{WW\gamma} &= -ie(W^\dagger_{\mu\nu}W^\mu A^\nu - W^{\mu\dagger}A^\nu W_{\mu\nu} + \kappa W^\dagger_\mu W_\nu F^{\mu\nu} \\
&+ \frac{\lambda}{M_W^2}W^\dagger_{\lambda\mu}W^\mu_\nu F^{\lambda\nu} + \tilde{\kappa}W^\dagger_\mu W_\nu F'^{\mu\nu} + \frac{\tilde{\lambda}}{M_W^2}W^\dagger_{\lambda\mu}W^\mu_\nu F'^{\lambda\nu}
\end{aligned} \tag{2.4}
$$

where W^μ and A^μ are the charged electroweak and photon fields respectively. The

A)u-channel

B)t-channel

C) s-channel

D)Inner Bremsstrahlung
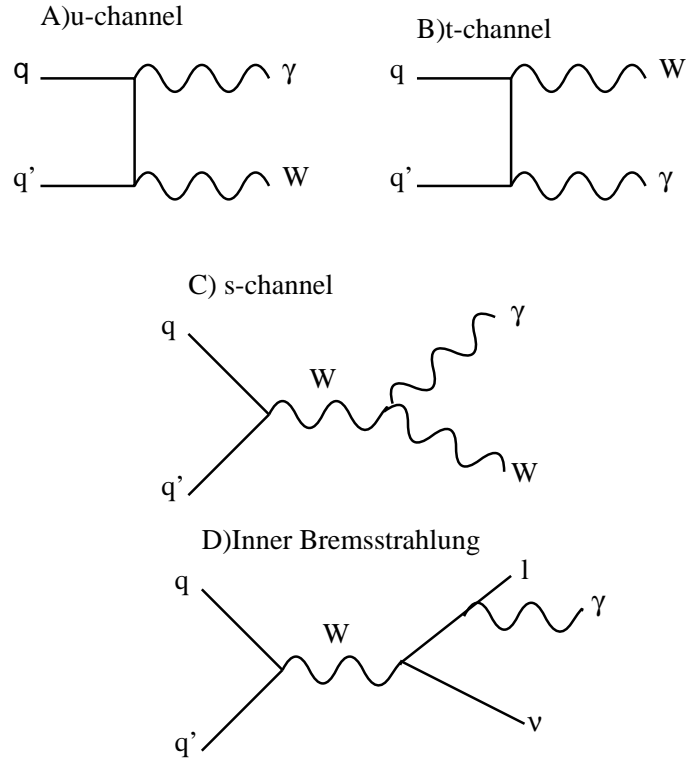
Figure 2.1: The tree level Feynman diagrams for $W\gamma$ production with the W decaying to an electron and neutrino.

previously mentioned current B has been replaced using the relations

$$A_\mu = B_\mu \cos\theta_W + W_\mu^3 \sin\theta_W$$

$$Z_\mu = -B_\mu \sin\theta_W + W_\mu^3 \cos\theta_W \tag{2.5}$$

$$\tag{2.6}$$

Here the tensors are defined as

$$W_{\mu\nu} \equiv \partial_\mu W_\nu - \partial_\nu W_\mu \tag{2.7}$$

$$F_{\mu\nu} \equiv \partial_\mu A_\nu - \partial_\nu A_\mu \tag{2.8}$$

$$F'_{\mu\nu} \equiv \frac{1}{2}\epsilon_{\mu\nu pq}F^{pq} \tag{2.9}$$

with $\epsilon_{\mu\nu pq}$ the completely anti-symmetric tensor and F^{pq} the generalized electro-magnetic field tensor. e is the charge of the electron, and in the Standard Model the terms $\kappa - 1 \equiv \Delta\kappa = \lambda = \tilde{\kappa} = \tilde{\lambda}=0$. These four terms are anomalous couplings incorporating possible extensions of the Standard Model. These coupling parameters are related to the structure of W boson in Section 2.3. All four of the couplings have a value of zero in the Standard model, but the definition of $\Delta\kappa$ should be noted. This parameter is defined as $\Delta\kappa = \kappa - 1$ as a matter of convenience so that any non-zero measurement of the parameter would signify a deviation from the Standard Model. For a $WW\gamma$ coupling constructed from only the $U_{EM}(1)$ group generator, $\Delta\kappa = -1(\kappa = 0)$. Therefore agreement between data and Standard Model prediction gives strong evidence that the unified $SU_L(2) \times U_Y(1)$ group must be used to describe electroweak interactions.

2.2   Radiation Amplitude Zero

One of the interesting aspects of coherently combining all of the Feynman graphs describing $W\gamma$ production is the presence of a Radiation Amplitude Zero (RAZ). The u- and t-channels of $W\gamma$ production destructively interfere with the s-channel production, and at tree-level this interference causes the differential cross section to vanish for a certain point in phase space. This vanishing differential cross section

is the RAZ and occurs at a scattering angle calculated from [11]

$$cos(\theta^*) = \frac{q_1 + q_2}{q_1 - q_2} = -\frac{1}{3} \tag{2.10}$$

Here, θ^* is the opening angle between the photon and the incoming quark in the W center-of-mass frame. q_1 and q_2 are the charges of the incoming quarks. Gauge cancellations such as this have been shown to be a possibility within any factorizable gauge theory with $W\gamma$ being one of the first such calculated RAZ. When more than the tree level terms are considered, the RAZ in the differential cross section is partially filled in due to the finite width of the W, parton distribution functions, and higher-order electroweak and QCD contributions. Contributions to the $W\gamma$ production from anomalous couplings would also destroy the exact cancelation of the tree-level calculation.

In the case of a hadron collider such as the Tevatron, the W center-of-mass frame cannot be exactly reconstructed and θ^* is indeterminate for $W\gamma$ events. Fortunately, for the x values probed at the Tevatron, $W\gamma$ production is dominated by valence quark contributions and there is an asymmetry in W production. The W^+ is produced dominantly in the proton direction, and the W^- production is in the antiproton direction. Taking advantage of this production asymmetry, the RAZ can be seen in the quantity $Q\Delta\eta_{l\gamma}$ [12].

$$Q\Delta\eta_{l\gamma} = Q_{lepton} \cdot (\eta_\gamma - \eta_{lepton}) \tag{2.11}$$

This is the charge-signed rapidity difference between the photon and the lepton. The charge, Q_{lepton}, is from the lepton and determines the sign of the W produced in the event. η is the psuedorapidity of the photon or lepton and is defined in

Chapter 4. The charge-signed rapidity difference for Standard Model production after detector simulation is shown in Figure 2.2. The effect of initial state QCD radiation from the incident partons is included in the distribution. The predicted minimum in the distribution occurs at -1/3, and the effect of the RAZ is seen in this distribution. The asymmetric W production is visible from the larger signal in the positive $Q\Delta\eta_{l\gamma}$ region of the distribution. The Radiation Amplitude Zero has yet to be conclusively resolved in experimental data.
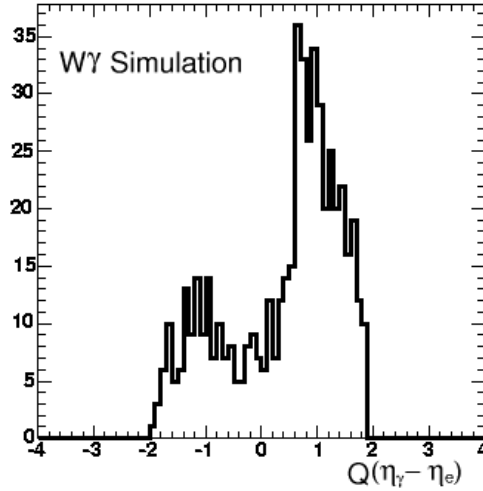
Figure 2.2: The Radiation Amplitude Zero shown in the charge-signed rapidity difference of simulated $W\gamma$ events. The effect of detector resolution and the initial parton distribution function is seen as a smearing of the zero. The RAZ is predicted to appear at $Q\Delta\eta_{l\gamma} = $ -1/3, but is smeared and has limited significance for the current data size. If there were no interference, the distribution would be peaked and centered at 0. The distribution is normalized to the integrated luminosity of the current dataset.

2.3   Anomalous Couplings in the $WW\gamma$ Vertex

The possible anomalous couplings for the $WW\gamma$ vertex are shown in the generalized Lagrangian (Eq. 2.4). These couplings are form factors, and take the generalized dipole form

$$\alpha(P^2 = \hat{s}, q_1^2 = M_W^2, q_2^2 = 0) = \frac{\alpha_0}{(1 + \frac{\hat{s}}{\Lambda^2})^2} \qquad (2.12)$$

where α_0 is one of the four dimensionless anomalous couplings ($\Delta\kappa, \lambda, \tilde{\kappa}, \tilde{\lambda}$), P^2 is the momentum exchange between the incident partons, $\hat{s}$ is the square of the center-of-mass energy, and q the four momentum of the two bosons. The contribution of the anomalous couplings is suppressed by Λ which is the characteristic energy scale where the non-Standard Model physics begins to contribute to the $W\gamma$ production. The introduction of the scale Λ is necessary in order to ensure unitarity of the s-channel contribution at high energy. The value of Λ can be viewed as the scale at which W compositeness might become apparent.

All of the factors are invariant under charge conjugation. The factors $\Delta\kappa$ and λ are also invariant under the parity operator, and so are CP-conserving. The terms $\tilde{\kappa}$ and $\tilde{\lambda}$ are parity odd and are then CP-violating.

In terms of W compositeness, the anomalous couplings can be related to the classical electromagnetic multipole moments of the W in the limit where the photon

energy goes to 0. The equations are given by [13]

$$\mu_W = \frac{e(1 + \kappa + \lambda)}{2M_W} \tag{2.13}$$

$$Q^e_W = \frac{-e(\kappa - \lambda)}{M^2_W} \tag{2.14}$$

$$d^e_W = \frac{e(\tilde{\kappa} + \tilde{\lambda})}{2M_W} \tag{2.15}$$

$$Q^m_W = \frac{-e(\tilde{\kappa} - \tilde{\lambda})}{M^2_W} \tag{2.16}$$

$$\tag{2.17}$$

with $\hbar = c = 1$. μ_W is the magnetic dipole moment, Q^e_W the electric quadrupole moment, d^e_W the electric dipole moment, and Q^m_W the magnetic quadrupole moment. The anomalous couplings can also be related to the mean-squared charge radius of the W

$$< R^2_W > = \frac{\Delta\kappa + \lambda}{M^2_W} \tag{2.18}$$

For Standard Model couplings, both the magnetic dipole moment and electric quadrupole moment of the W are non-zero while the electric dipole and magnetic quadrupole moments are zero.

The four anomalous coupling parameters listed earlier are the complete set needed to describe all of the possible interactions between the W and γ. This is apparent when considering the helicity combinations of the W and γ bosons. As both are vector bosons, the W and γ each have spin 1. But considering the helicity of particles (the dot product of the momentum and the spin, β), the massless photon has only + and - states, while the massive W has three possible helicity states: +, 0, and -. The possible combinations are shown in Figure 2.3 [15]. As the initial state W has spin 1, conservation of angular momentum requires that the only allowed

states (β_γ, β_W) after the photon production are (+,-), (+,0), (-,0), and (-,+). Only these states can have total angular momentum of 1, while the states (+,+) and (-,-) have total angular momentum 2. This leaves four possible interactions and four free parameters to describe the interactions. The anomalous contributions to $W\gamma$ production can be represented in term of these helicity states. The contributions to the $W\gamma$ production from the individual anomalous couplings are written in terms of the helicity states as $\Delta M_{\beta_\gamma, \beta_W}$ with

$$\Delta M_{\pm 0} = \frac{e^2}{sin\theta_W}\frac{\sqrt{\hat{s}}}{2M_W}[\Delta\kappa + \lambda \mp i(\tilde{\kappa} + \tilde{\lambda})\frac{1}{2}(1 \mp cos\theta^*) \tag{2.19}$$

$$\Delta M_{\pm\pm} = \frac{e^2}{sin\theta_W}\frac{1}{2}[\frac{\hat{s}}{M_W^2}(\lambda \mp i\tilde{\lambda}) + (\Delta\kappa \mp i\tilde{\kappa})]\frac{1}{\sqrt{2}}(sin\theta^*) \tag{2.20}$$

$$\tag{2.21}$$

Here, θ^* is the previously defined angle from Equation 2.10 and θ_W is the electroweak mixing angle.

For the Standard Model couplings, the photon transverse energy distribution is sharply peaked at low energy. The presence of the gauge cancellation discussed previously contributes to the rapid fall of this distribution. But the addition of anomalous couplings causes the cancellation to be incomplete and increases the $W\gamma$ production in the previously suppressed high-E_T^γ region. These effects combine to make the photon transverse energy spectrum harder for models containing anomalous couplings. This harder photon transverse energy distribution can be seen in Figure 2.4. Therefore, the presence of an excess of high transverse energy photon candidates would suggest the possible presence of anomalous couplings. Additionally, the existence of non-Standard Model couplings would cause the measured cross section to be larger than expected.

Allowed States
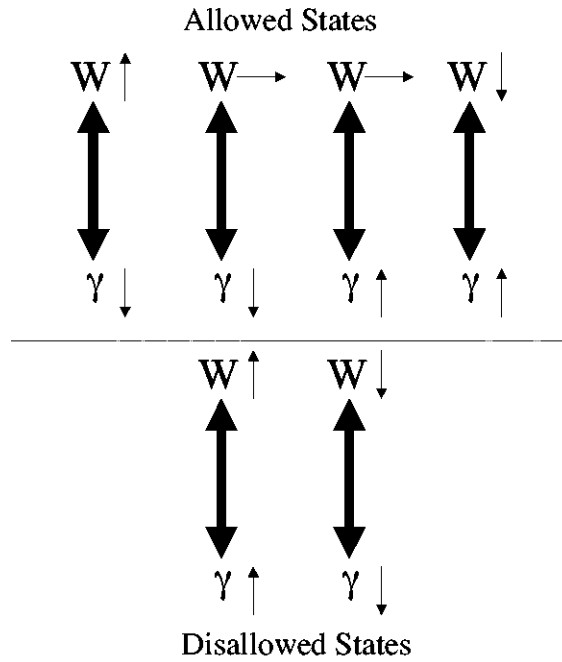
Disallowed States

Figure 2.3: The possible spin states for the s-channel production of $W\gamma$ events. Assuming that the W is a spin 1 particle, then there are four allowed spin states of the γ and W, [(+,-),(+,0),(-,0), and (-,+)]. The disallowed states on the bottom of the plot would violate angular momentum conservation as they have a total spin of 2, while the initial W state has a spin of 1.

Using the Electroweak theory, simulated $\bar{p}p \rightarrow W\gamma + X$ signal samples are generated for comparison with collider data. The implementation of this generation process is discussed in detail in Chapter 6.
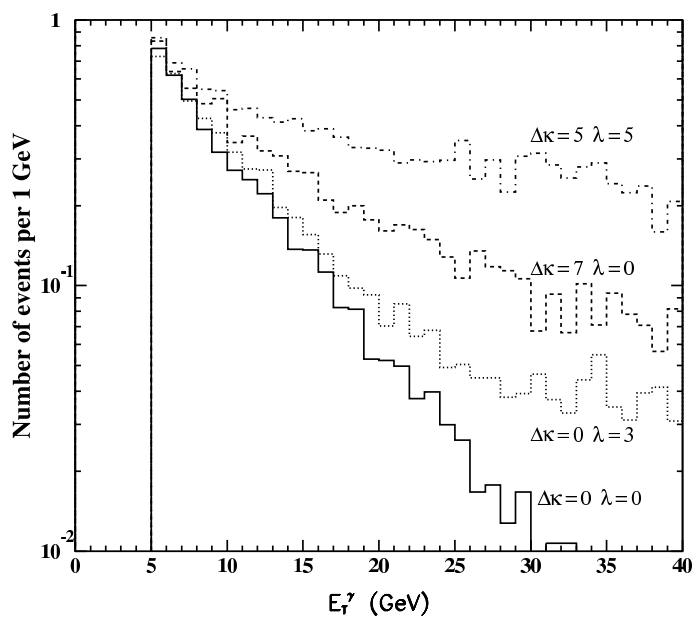
Figure 2.4: Photon transverse energy (GeV) distribution for $W\gamma$ events with Standard Model couplings and several examples of anomalous couplings. The enhancement of the production rate at high transverse photon energy can be seen for models containing anomalous couplings. The samples were generating with a form factor scale of $\Lambda = 1.5$ TeV.

Chapter 3

Present Experimental Knowledge

Since the discovery of the W boson and the Z boson in 1983, the production of diboson events has been a topic of great interest and numerous measurements. Limits on the couplings between bosons have been determined from both direct and indirect measurements. While extractions of limits from indirects means are possible in the low energy regime, the energy needed to probe directly the $WW\gamma$ vertex is only achievable at collider facilities. Therefore, the direct results are limited to experiments at the Large Electron Positron Collider 2 (LEP2) at CERN, and the Tevatron collider at Fermilab. The four LEP2 experiments (ALEPH, DELPHI, L3, and OPAL) have each measured the Triple Gauge Couplings (TGCs) of the $WWV(V = Z/\gamma)$ vertex. With a center-of-mass energy of 183 GeV or greater, the collisions at the LEP2 collider are well above the two W on-shell energy threshold. The Tevatron $p\bar{p}$ collisions open up the possibility of $W + \gamma$ final states allowing measurements of the $WW\gamma$ vertex with no contribution from WWZ. Both the CDF and D0 experiments at the Tevatron at Fermilab measured the cross section at the Run I energy of $\sqrt{s} = 1.8$ TeV and placed limits on the Trilinear Gauge Couplings for $WW\gamma$. The results of these experiments are summarized and their significance within the Standard Model discussed.

3.1 LEP2 Results

The LEP2 collider is an electron-positron collider which a center-of-mass energy ranging from 183 GeV to 209 GeV. Some relevant tree-level diagrams for the LEP2 analyses are shown in Figure 3.1 and include W-pair, single photon, and single W production. The channel with the largest production rate is the W-pair production, and the analysis of these events is the most significant for extracting limits on trilinear gauge couplings. The dominant channel used in the analyses is that where one W decays leptonically and one hadronically. The details of each of the four experimental results (ALEPH, DELPHI, L3, and OPAL) are not discussed below as all take similar analysis strategies. One of the limitations of the LEP2 results is that there is an explicit assumption that the couplings $\Delta\kappa$ and λ are the same for the $WW\gamma$ and WWZ vertex. The analyses fit $\Delta\kappa$ and λ to the total cross-section, along with additional fits to W production angle and lepton angle when applicable.
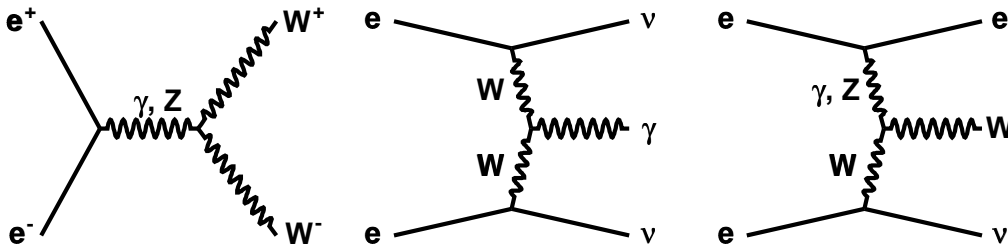
Figure 3.1: Feynman Diagrams for studying TGCs at LEP2

The results from the four LEP2 [16–19] experiments are listed in Table 3.1. The analyses use the optimal observable technique [20] that takes advantage of kinematic fits to each event to perform a χ^2 fit to the data and expectation. From these best fits, limits on the anomalous couplings in the WWZ/γ system are calculated. All of the parameters and limits reported here are from single parameter fits where all

other parameters are set to their Standard Model values of 0. The results for $\Delta\kappa_\gamma$ and λ_γ are consistent with the Standard Model prediction of 0 for both parameters. The uncertainties are about 2.5% and 5.5% for λ_γ and $\Delta\kappa_\gamma$ respectively. The results have been combined [21] together to make the most accurate fits to the trilinear gauge couplings. The limits on the TGCs at the 95% confidence level are -0.005 $< \Delta\kappa < 0.069$ and $-0.059 < \lambda < 0.026$. Additionally, the OPAL experiment has calculated the limit on the radius of the W boson from a multiparameter fit to the hadronic, semi-leptonic, and single W leptonic channel with a result of $R_W < 0.3 \pm 0.19 \times 10^{-19}m$. Because the $WW\gamma$ vertex is studied in W-pair events for a electron-positron collider, there is no sensitivity to the $WW\gamma$ Radiation Amplitude Zero at LEP2.

	λ	$\Delta\kappa$
ALEPH	$0.101^{+0.069}_{-0.069}$	$0.075^{+0.061}_{-0.061}$
DELPHI	$0.015^{+0.045}_{-0.042}$	$-0.043^{+0.099}_{-0.096}$
L3	$-0.088^{+0.064}_{-0.061}$	$-0.076^{+0.064}_{-0.061}$
OPAL	$-0.061^{+0.035}_{-0.034}$	$-0.12^{+0.09}_{-0.08}$
COMBINED LEP (LEP EWK 2003)	$-0.016^{+0.021}_{-0.023}$	$0.016^{+0.042}_{-0.047}$

Table 3.1: Values for λ_γ and $\Delta\kappa_\gamma$ for the four LEP experiments from data at several energies ($\sqrt{s} = 183 \rightarrow 209$ GeV and the preliminary combined value using all of LEP II presented by the LEP Electroweak Working Group in 2003.

3.2   Tevatron Results

Both the CDF and D0 experiments measured the production of $W\gamma$ events in $p\bar{p}$ collisions at $\sqrt{s} = 1.8$ TeV at the Tevatron in the dataset taken in 1992-1995 [22,23].

The integrated luminosities of the datasets studied are 92.8 pb^{-1} for D0 and 67 pb^{-1} for CDF. For both experiments, the $W\gamma$ events were selected based upon the electron and muon decay of the W. The photons were selected with transverse energy $E_T^\gamma > 7$ GeV at CDF, and $E_T^\gamma > 10$ GeV at D0. The measured cross sections for the $W\gamma$ production are shown in Table 3.2.

Table 3.2: The $W\gamma$ cross section times the leptonic branching ratio for $E_T^\gamma > 10$ GeV (D0) and $E_T^\gamma > 7$ (CDF) as measured in the Tevatron Run 1 datasets. The photon is required to be separated from the lepton in $\eta - \phi$ space by $\Delta R > 0.7$. The errors shown are combined systematic and statistical followed by the luminosity error.

	CDF ($\int \mathcal{L} = 67pb^{-1}$)	D0$\int \mathcal{L} = 92.8pb^{-1}$)
$E_T^\gamma >$	7 GeV	10 GeV
$\sigma \cdot BR$	$20.7 \pm 2.9 \pm 0.7$pb	$11.3 \pm 2.2 \pm 0.6$pb
$\sigma \cdot BR(SM)$	18.6 ± 2.9pb	12.5 ± 1.0pb

To set limits on the anomalous couplings, a binned maximum likelihood fit was performed on the E_T^γ spectrum. Form factors with a scale of $\Lambda = 1.5$ TeV were used in the event generation to determine the likelihood function. The resulting limits on the trilinear gauge couplings $\Delta\kappa$ and λ are listed in Table 3.3. The limits are significant because these are the first direct limits on $\Delta\kappa$ to exclude the $U_{EM}(1)$ couplings where the electromagnetic force is not unified with the weak force.

Using the same assumption used at LEP2 that the couplings for $WW\gamma$ are equal to the WWZ couplings, a combined fit to WW, WZ and $W\gamma$ data can be performed at the Tevatron. The D0 experiment performed such a simultaneous fit to the $W\gamma \rightarrow l\nu\gamma$, $WW \rightarrow$ dilepton, $WW/WZ \rightarrow e\nu jj$, $WW/WZ \rightarrow \mu\nu jj$, and $WZ \rightarrow$ trilepton data samples [23] from the data collected during Run I operation. The published limits are

$$\Delta\kappa = -0.08 \pm 0.34 \qquad (3.1)$$

Table 3.3: The 95% confidence limits on the anomalous couplings $\Delta\kappa$ and λ from the CDF and D0 $W\gamma$ analyses in Run 1 at the Tevatron. The fits come from a binned maximum likelihood fit to the photon transverse energy spectrum. The anomalous coupling form factor scale used for the generation of non-Standard Model samples was $\Lambda = 1.5$ TeV.

	$\lambda = 0$	$\Delta\kappa = 0$
CDF	-1.8< $\Delta\kappa$ <2.0	-0.7< λ <0.6
D0	-0.93< $\Delta\kappa$ <0.94	-0.31< λ <0.29

and

$$\lambda = 0.00^{+0.10}_{-0.09} \tag{3.2}$$

These limits are not yet competitive with the LEP limits discussed above due to the limited statistics.

3.3 Current Experimental Goals

The measurement presented in this thesis extends the current knowledge of W boson self couplings and is sensitive to new physics that might appear in the $e\nu\gamma$ final state. This analysis extends upon this current experimental knowledge by using higher energy collisions and a larger data sample. The measurement of the $W\gamma$ production cross section uses the highest energy proton-antiproton collisions in the world to study these fundamental particles and the forces between them. The center-of-mass energy increase of more than 8% increases the predicted production cross section of $W\gamma$ from the previous Run I value and probes a slightly different region of phase space. Of greater importance is the larger data sample with the integrated luminosity analyzed increased by over a factor of two.. This larger data sample increases the sensitivity to any new physics appearing in the $W\gamma$ or $e\nu\gamma$ final

states. The details of the upgraded Tevatron and Collider Detector at Fermilab are discussed in the next chapter.

Chapter 4

Experimental Design

4.1   Introduction to Experiment

The experimental apparatus is located at the Fermi National Accelerator Laboratory (Fermilab) in Batavia, Illinois. Two main components constitute the experiment: the Tevatron Accelerator and the Collider Detector at Fermilab (CDF). The Tevatron is a 1 km radius $p\bar{p}$ collider that creates the highest-energy man-made collisions in the world. These collisions occur at the center of two general-purpose particle detectors, the CDF and D0 detectors. These detectors record data describing the particles generated along with the $p\bar{p}$ remnants. This chapter discusses the details of the Tevatron operation and the CDF detector used in the analysis.

4.2   Accelerator Operation

The center piece of the Fermilab facility, the Tevatron accelerator, is a 1.96 TeV proton-antiproton synchrotron accelerator creating collisions at two points on the ring. Six cardinal points, A0 through F0, define the Tevatron ring, while the full accelerator chain is shown graphically in Figure 4.1. The acceleration process begins in the Cockroft-Walton, and then continues to the Linac, Booster, Main Injector,
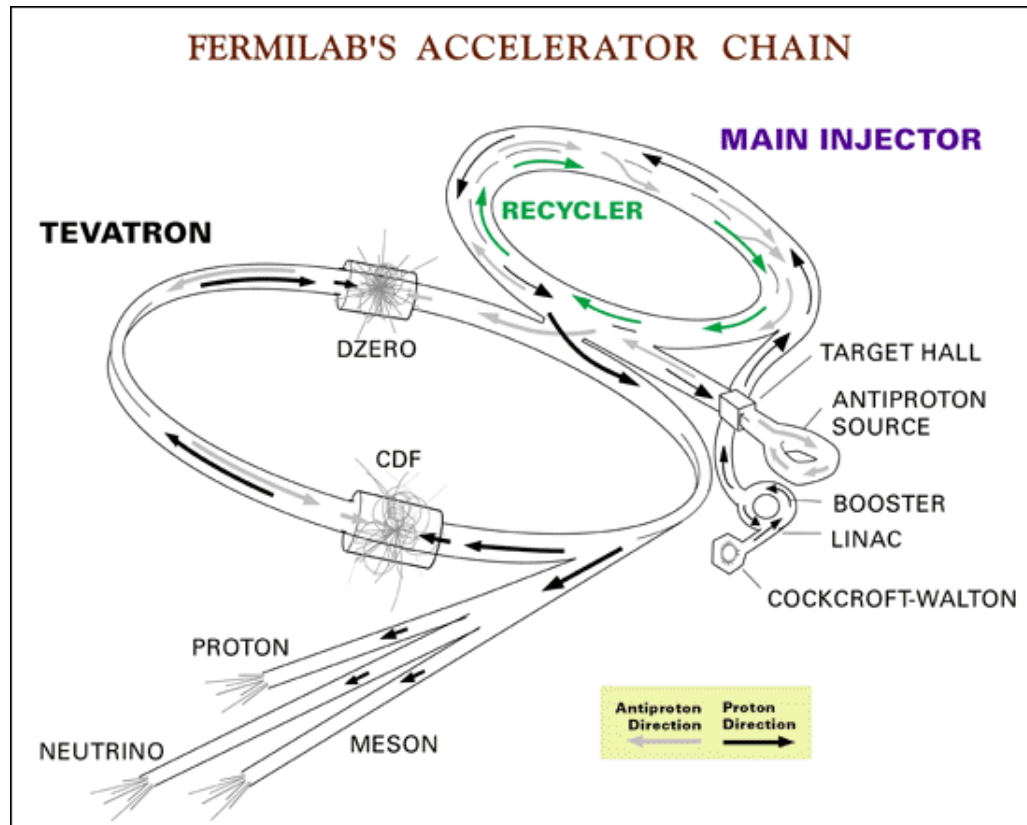
Figure 4.1: The Ferimlab Tevatron accelerator chain.

and ends with collisions in the Tevatron. Antiprotons are not readily available in nature, and must be generated in the AntiProton Source. Once antiprotons have been created in the AntiProton Source, they continue on to the Main Injector and the Tevatron. Finally, the protons and antiprotons are focused into collisions in the Tevatron ring and interact through a variety of high energy processes.

4.2.1   Proton Production

The accelerator process begins with the generation of low-energy protons. The Cockroft-Walton pre-accelerator is the initial step in generating these particles. Using hydrogen gas as a source, the Cockroft-Walton is a small electrostatic accelerator

that creates hydrogen ions by giving atomic hydrogen an additional electron. With
the additional negative charge, a constant positive electric potential then accelerates
the ions to an energy of 750 keV. The ions leaving the Cockroft-Walton are injected
into the linear accelerator (LINAC). The LINAC is a 150 m long sequence of radio-
frequency (RF) cavities. The ions entering the LINAC experience an oscillating
electromagnetic field that is varied such that the ions are continuously accelerated.
In this process, the ions ride the leading edge of the oscillating field similar to a
surfer on a wave. At the end of the LINAC, the ions exit in bunches with a kinetic
energy of 400 MeV. The grouping of particles in bunches is both a consequence
and a necessity when using an RF cavity. At this stage, the ions are directed onto
a carbon foil target which strips the hydrogen of its electrons. Such a manipula-
tion is necessary in order to overcome the broad phase space occupied by particles
leaving the LINAC. This large phase space volume is incompatible with the design
of the higher energy synchrotrons that come later in the accelerator chain. From
Louisville's Theorem, the phase space occupied by an ensemble cannot be changed
by any reversible process. But since stripping the electrons is an irreversible process,
the spatial distribution of the protons can be manipulated at this point without con-
sequences to the momentum distribution. Thus after stripping the hydrogen ions of
both electrons, what remains is a tightly packed, low-dispersion beam of protons.

For the next stage, the protons are injected into the 75 m radius BOOSTER
synchrotron where the kinetic energy is raised from 400 MeV to 8 GeV. The pro-
tons traverse the BOOSTER approximately 20000 times, with each pass adding
more energy from short linear sections of electric potential. After transfer from
the BOOSTER the 8 GeV protons are destined either for collisions or antiproton
generation. The two paths are discussed in the next section which describes the

recently commissioned Main Injector.

4.2.2 Main Injector

The Main Injector is the largest upgrade to the Tevatron facility for the Run 2 experiment. It replaces the Main Ring, a the synchrotron located within the Tevatron ring and immediately above the Tevatron. The Main Ring is no longer in use for collider physics. The Main Injector (MI) is a 3 km circumference synchrotron located southwest of the Tevatron main ring and tangent to the F0 location. The Main Injector accelerates, coalesces, and stores protons that will be used in the Tevatron or for producing antiprotons. Protons headed for the Tevatron are transfered from the BOOSTER into the Main Injector 7 bunches at a time with each bunch containing $\approx 6 \times 10^{10}$ particles. These bunches are accelerated to an energy of 150 GeV while being coalesced into a single bunch with an emittance of 30π mm-mr before transfer to the Tevatron. Emittance measures the cross sectional size of a particle beam, determining the smallest aperture the beam can pass through. Similarly, an accelerator or storage ring has an admittance, which is the largest size beam that can be used within the accelerator. The low emittance beam produced from the Main Injector matches the Tevatron admittance better than the previously used Main Ring, and allows the bunches to be more stable once transfered to the Tevatron. The process of coalescing, accelerating, and transferring is repeated 36 times, creating the 36 proton bunches in the Tevatron.

The other possible path for protons in the MI is to produce antiprotons. For this task, the protons are accelerated from 8 GeV to 120 GeV in the Main Injector. They are then incident upon a nickel target where these collisions result in a large variety of outgoing secondary particles including antiprotons. Using a lithium lens, the

secondary particles are focused and aligned in parallel trajectories. The antiprotons exit the lens with a wide distribution of energy, but a peak value near 8 GeV. The antiprotons at a momentum of 8 GeV/c are selected using a pulsed dipole magnet. The selected particles are fed into the Debuncher where the process of stochastic cooling reduces the energy spread while maintaining the central value of 8 GeV/c. While stochastic cooling gives particles a tight energy distribution, the longitudinal position distribution is extended producing a continuous beam. Since both the Main Injector and Tevatron use RF cavities, the continuous beam must be separated back into bunches. The Accumulator takes the continuous beam of antiprotons from the Debuncher and stacks them back into bunches. Once a sufficiently large stack of antiprotons have been accumulated ($\approx 100 \times 10^9$ particles), the 8 GeV antiprotons are injected into the MI and coalesced into 4 bunches separated by 396 ns. These 4 bunches are accelerated up to 150 GeV and injected into the Tevatron orbiting oppositely to the previously injected protons. This step is repeated 9 times until there are 36 bunches of antiprotons in the Tevatron.

4.2.3   Tevatron

The final stage of the accelerator complex is the super-conducting Tevatron ring. The Tevatron is a 1 km radius ring composed of super-conducting dipole, quad-rupole, and sextapole magnets located approximately 10 m below ground. Bunches of protons and antiprotons are transfered from the Main Injector into the Teva-tron in opposite directions, with protons traveling clockwise; antiprotons counter-clockwise. The beams are accelerated to a final energy of 980 GeV and travel on helical orbits that intertwine with each other similar to the double helix of DNA. Using RF separators, the two orbits do not intersect except at two points, B0 and

D0, where the two beams are focused into collisions using the low beta quadrupole magnets. During the low beta squeeze, the helical orbit is changed and the transverse beam size is reduced to bring the beams into collisions. The store, defined as the 36 bunches of protons and 36 bunches of antiprotons, is maintained until the collisions and beam decay reduce the luminosity enough to mandate another store. The average length of a store is approximately 18 hours, if there are no technical malfunctions. Table 4.1 lists the operational parameters and performance of the Tevatron.

Table 4.1: The Tevatron operational parameters and performance during the March 2002 and September 2003 data taking period.

$\sqrt{s}$	1.96 TeV
N bunches	36
Bunch Spacing	396 ns
Store lifetime	18 hrs
Highest $\mathcal{L}$	$4.06 \times 10^{31} cm^{-2} s^{-1}$
Average Initial $\mathcal{L}$	$3 \times 10^{31} cm^{-2} s^{-1}$

4.2.4 $p\bar{p}$ Collision Properties

Three basic machine parameters define the performance and capabilities of an accelerator: the center of mass energy of the colliding particles $\sqrt{s}$, the instantaneous luminosity, and bunch spacing. The most important parameter is $\sqrt{s}$. For particles with the same lab frame energy this is $E_1 + E_2$. At the Tevatron, the proton and antiproton have equal energy of 980 GeV, giving a $\sqrt{s} = 1.96$ TeV. But due to the composite nature of hadrons, the energy involved in the interaction is not $\sqrt{s}$. Since hadrons consist of quarks, anti-quarks, and gluons, each parton will carry some fraction, x_i of the total hadron energy of 980 GeV. (For a full discussion of

parton distribution functions see Section 1.5.) Therefore the energy involved in the interaction is the energy from these two partons, $\sqrt{\hat{s}} = \sqrt{sx_px_{\bar{p}}}$. From conservation of energy and special relativity, this energy determines the highest mass particles that can be created from the particles collisions. As well, cross sections and event yields for processes depend upon the energy in the collision. Since the distribution of $\sqrt{\hat{s}}$ is determined by and cannot exceed $\sqrt{s}$, in large part the available physics reach of an accelerator is defined by $\sqrt{s}$.

The second machine parameter is the luminosity of the two colliding beams of particles. Luminosity $\mathcal{L}$ is defined by

$$\mathcal{L} = f\frac{n_pn_{\bar{p}}}{4\pi\sigma_p\sigma_{\bar{p}}} \tag{4.1}$$

where f is the frequency of crossing for bunches containing n_p protons and $n_{\bar{p}}$ anit-protons, and the Gaussian transverse beam profiles are given by σ_p and $\sigma_{\bar{p}}$. The conventional unit for luminosity is $cm^{-2}s^{-1}$. Multiplying $\mathcal{L}$ by the inelastic cross section of $p\bar{p}$ interactions gives the rate of collisions. In general terms, $\mathcal{L}$ measures how large of a "target" one beam of particles encounters as it passes through the other beam and how often a collision will occur during that crossing time. As of early 2004, the Tevatron is operating at an instantaneous luminosity of $4 \times 10^{31}cm^{-2}s^{-1}$, with the goal of reaching $8 \times 10^{31}cm^{-2}s^{-1}$ by the end of 2004. Integrating the luminosity over an entire data collection period gives the integrated luminosity, $\int \mathcal{L}dt$. When multiplied by the cross section of a given process, the integrated luminosity gives the predicted number of events, N_i

$$N_i = \sigma_i \times \int \mathcal{L}dt \tag{4.2}$$

from process i that occurred during data taking. It should be noted that some of values listed in Equation 4.1 are not easily measurable, and the luminosity must be measured experimentally during data taking. This will be discussed further in the description of the CDF detector.

The final machine parameter is the bunch spacing, or the time between two bunches crossing at the collision point. This is $1/f$, where f was defined previously for $\mathcal{L}$. The Tevatron currently operates at a bunch spacing of 396 ns. Along with determining $\mathcal{L}$, the bunch spacing defines the time the detector has to collect and store information about produced particles. Therefore, a detector capable of operating under these conditions and a data acquisition system with enough bandwidth to store interesting event data must be constructed around the collision point.

Using these three parameters, $\sqrt{s}$, $\mathcal{L}$, and f, predictions were made for the experimental reach of the Tevatron, and the potential for exploring the Standard Model and physics beyond the Standard Model. Additionally, the CDF detector was designed and constructed to match the experimental conditions described by these parameters.

4.3 Detector Design

The Run 2 Collider Detector at Fermilab (CDF) is a general purpose particle detector constructed around a super-conducting solenoid. See Figure 4.2 for a three dimensional rendering of the detector. The cylindrically symmetric detector contains components for measuring the energy, momentum, and identity of the particles produced by $p\bar{p}$ collisions. The CDF detector is constructed of three primary subsystems: tracking, calorimetry, and muon systems. A more detailed elevation view labeling the different components is shown in Figure 4.3. The diagram in Figure
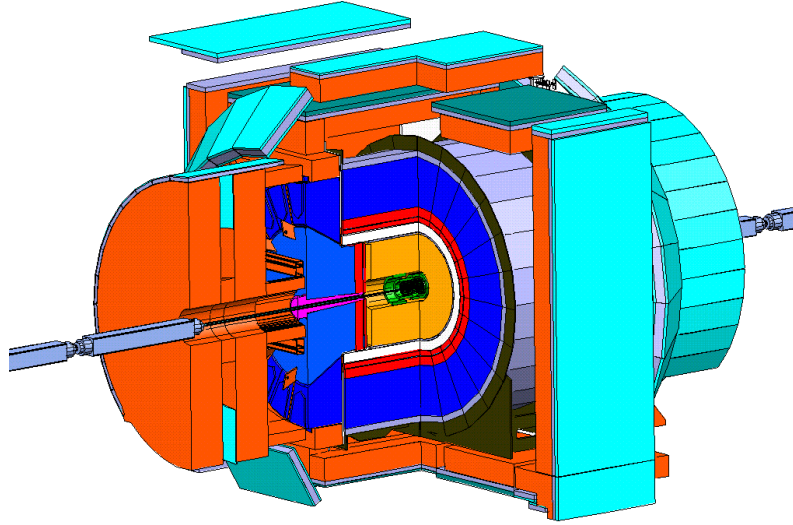
Figure 4.2: An isometric view of the CDF detector with one quarter removed to see the tracking volume.

4.4 shows a generalized detector component response to several particles.

Due to the high rate of collisions and the large amount of data, a three-level triggering system is used to filter and collect interesting events. In the subsequent sections, each of the subsystems will be described along with a description of the Data Acquisition (DAQ) system that collects and records the selected events. After defining the coordinate system, the description starts at the inside of the detector and progresses outward.

4.3.1 CDF Coordinate System

The CDF coordinate system is defined with the clockwise travel of the protons being the positive z direction. The positive y axis is chosen to be upward, and the positive x axis defined from the traditional right handed vector cross product, $\vec{x} \times \vec{y} = \vec{z}$. The angles ϕ and θ are then defined as the azimuthal angle from the
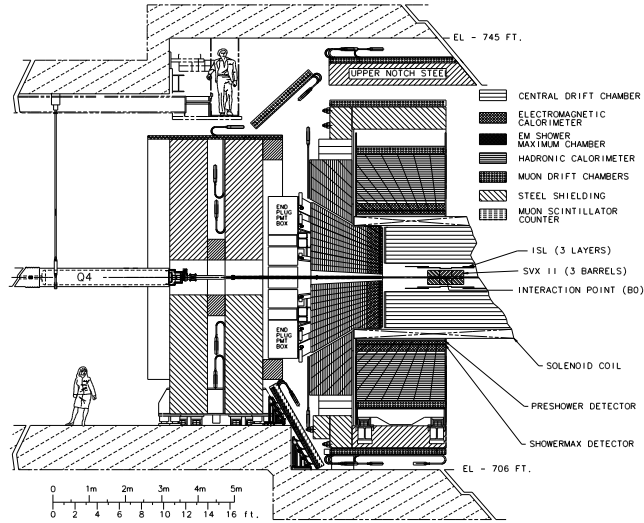
Figure 4.3: An elevation view of the Collider Detector at Fermilab.
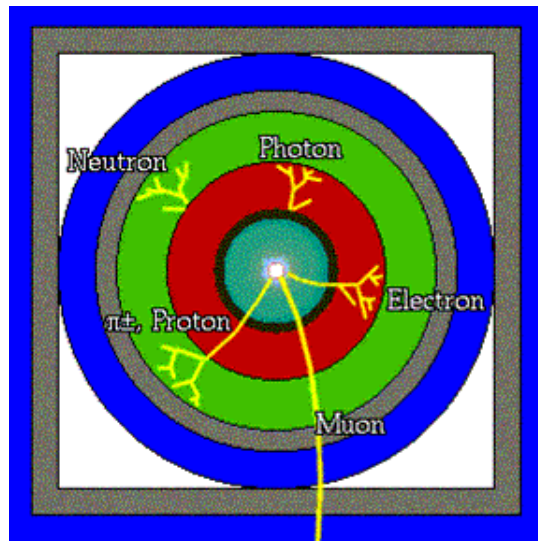
Figure 4.4: A diagram showing the generalized detector response to various particles produced during collisions.

$+x$ axis and the polar angle from the z axis respectively. An additional angular
measure, psuedorapidity, is defined as

$$\eta = -\ln\left(\tan\frac{\theta}{2}\right) \tag{4.3}$$

Here, psuedorapidity is the zero-mass limit of the invariant quantity rapidity given
by

$$y = \frac{1}{2}\ln\frac{E+p_z}{E-p_z} \tag{4.4}$$

Frequently, it is important to refer to the transverse component of momentum or
energy. The transverse plane is perpendicular to the z axis and passes through the
interaction point. A schematic showing the coordinate system is shown in Fig 4.5.
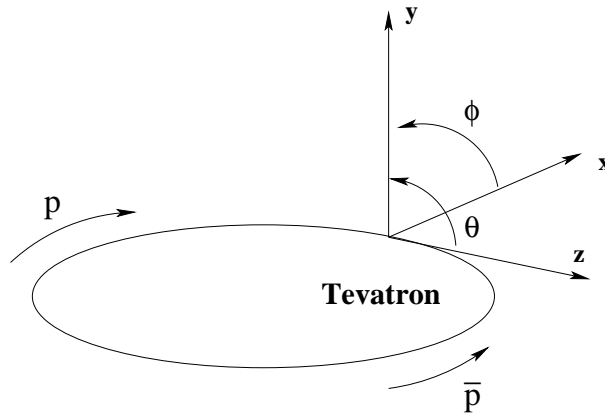
Figure 4.5: The coordinate system used by the CDF experiment.

4.3.2   Luminosity Monitoring

The instantaneous luminosity, $\mathcal{L}$, was previously defined in Equation 4.1, but the
factors in the definition cannot be measured with sufficient precision. Since mea-
suring the integrated luminosity is necessary to predict event yields and monitoring

the instantaneous luminosity critical to detector operation, a custom detector must be used to determine the luminosity. For Run 2, CDF uses a Cherenkov Luminosity Counter (CLC) to measure the instantaneous luminosity [25]. The CLC has two modules, each located in the small 3° conical hole in the high η region of the forward calorimeter. The luminosity monitor is constructed of an array of segmented counters, with each counter being 2 m long and several cm in diameter. The counters are constructed of aluminized mylar and filled with Isobutane gas. A fast PhotoMultiplyer Tube (PMT) at the end of each counter collects the Cherenkov light from charged particles radiating in the gas, and gives a timing resolution of better than 100 ps. This resolution is needed for coincidence measurement between the two CLC modules. A schematic of one CLC module in the detector is shown in Figure 4.6. The projective design of the counters means that they have reduced sensitivity to secondary particles produced in the detector or from beam pipe interactions. The CLC is also not sensitive to beam halo particles since they hit the CLC from behind generating Cherenkov light going away from the PMTs. Measuring the number of hits in the CLC allows calculation of the instantaneous $\mathcal{L}$ as defined by Eq. 4.5.

$$\mathcal{L} = \frac{f_{BC}}{\sigma_{in}\varepsilon_\alpha}\frac{<N_H>_\alpha}{<N_H^1>_\alpha} \tag{4.5}$$

Here f_{BC} is the bunch crossing frequency, and σ_{in} the inelastic $p\bar{p}$ cross section. Given the selection criteria α, ε_α is the CLC efficiency, $<N_H>_\alpha$ the number of hits in the CLC for the bunch crossing, and $<N_H^1>_\alpha$ the number of hits in the CLC for a single $p\bar{p}$ collision. The measured error on the acceptance of the CLC is 4%, and along with the error on the measured inelastic $p\bar{p}$ cross section of 4%, gives an integrated luminosity error of 6% for Run 2 data collection.
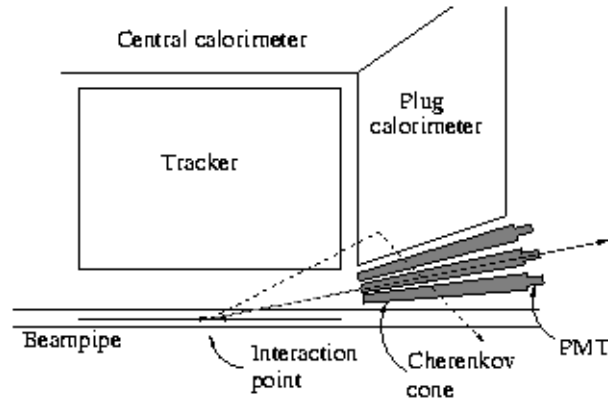
Figure 4.6: A schematic view of the CLC in the 3° hole of the forward calorimeter. Two particle paths are shown exhibiting the limited sensitivity to secondary particles.

4.3.3 Tracking System

The tracking system is the central component of the CDF detector. Surrounded by a super-conducting magnet, the Silicon Vertex Tracker (SVX II) and the Central Outer Tracker (COT) are the main detectors of the tracking system. These detectors record the paths of charged particles produced during collisions. With tracking coverage $|\eta| < 2.0$, the SVX II and COT tracking coverage has increased by 50% compared to Run 1, while maintaining good momentum resolution. Both systems can be used stand alone or in conjunction to produce three dimensional tracks of charged particles. The coverage of the tracking volume is shown in Figure 4.7.

Central Magnet

The entire tracking volume of the CDF detector is contained within a super-conducting magnet constructed of NbTi/Cu. The solenoid is 1.5 m in radius and 5 m in length, producing a uniform magnetic field of 1.4 Tesla along the incident
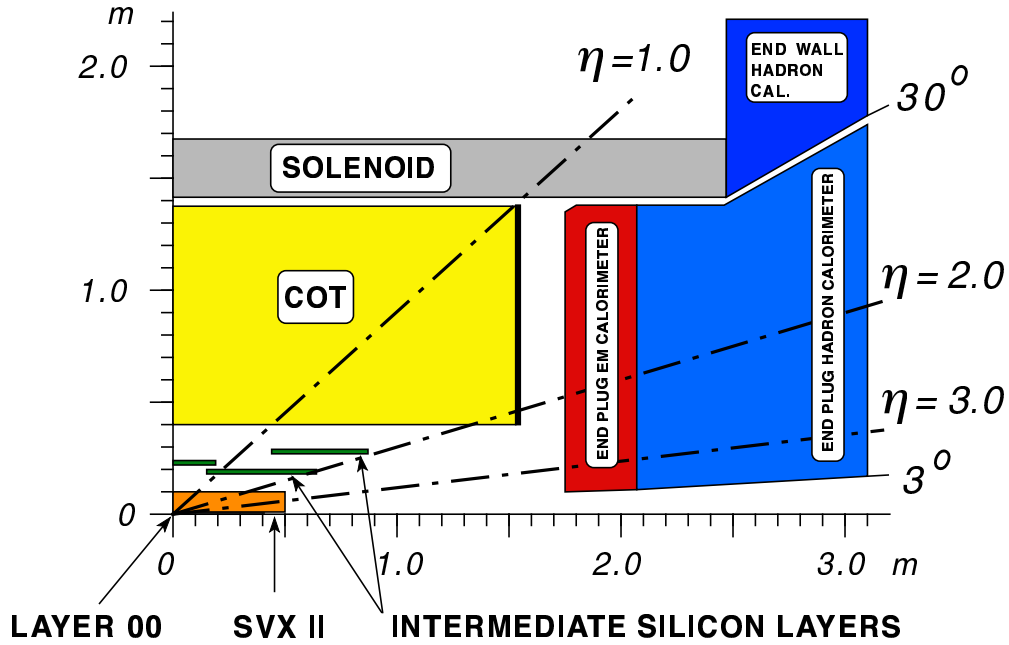
Figure 4.7: One quadrant of the CDF tracking volume.

beam direction. Such a field is necessary in order to measure the momentum of
a charged particle traversing the detector. As a charged particle travels through
the magnetic field, the trajectory is curved in the $r - \phi$ plane by the Lorentz force,
while maintaining a constant velocity in the z direction. The result is a helical flight
path through the tracking volume with approximately constant $|\vec{p}|$. Some energy
loss does occur during flight, and this $\frac{dE}{dX}$ is modeled and accounted for in the track
reconstruction. Using the position measurements from the tracking chambers, the
flight path of a particle is reconstructed by connecting hits together, the details are
discussed in Section 5.2.3. Once the helical path is reconstructed, using the classical
equations of electrodynamics gives the transverse momentum in MeV/c as

$$p_\perp = 3.00 B \rho \tag{4.6}$$

where B is the magnetic field in Telsa, and ρ is the radius of curvature in centimeters. Thus, given ρ for a track, the azimuthal angle (ϕ) and the polar angle (θ,) the initial momentum is calculated for each charged particle. The factors defining the momentum resolution on the track are the single hit position resolution and the tracker lever arm. As the lever arm of the tracker increases for a constant position resolution, the momentum resolution improves. For CDF, the large lever arm is provided by the COT, while the SVXII provides precision position measurement near the production collision point.

Silicon Vertex Detector

The silicon strip detector at the center of the CDF detector is an extremely high precision tracker. Using depleted silicon wafers, the tracker measures the location and amount of charge deposited by particles passing through the sensors. The primary goal of the silicon detector is to reconstruct tracks for use in the pattern recognition of displaced secondary vertices. These secondary vertices are created from the decay of long lived particles and help in the identification of charm and beauty hadrons. In order to accomplish the position resolution, the detector is located very close to the interaction region. As well, to aid in pattern recognition, small angle stereo and 90° layers were added to the detector design to reconstruct three dimensional tracks. The silicon strip detector has three components each with somewhat different function: Layer 00, Silicon Vertex Detector (SVXII), and the Intermediate Silicon Layers (ISL). Figure 4.8 shows an $r - \phi$ view of all three sub components.

The primary technology behind silicon strip detectors is the same used in common semi-conductors. Using 300μ m thick silicon wafers, depletion regions are
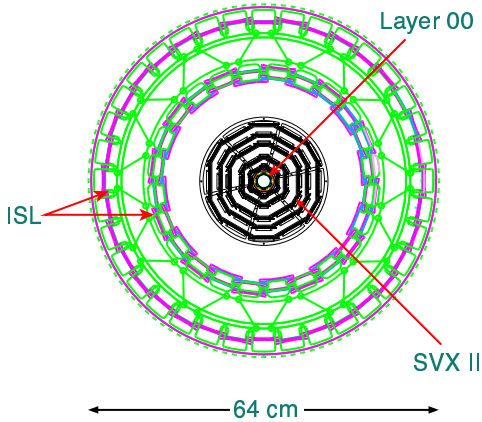
Figure 4.8: The CDF Silicon detector end view showing the layering and space frame used to mount the detector.

constructed by applying a high voltage across the semi-conductor junction. The high voltage accumulates "holes" at the p junction, with the free electrons at the n junction. The region in the center of the silicon strip is then free of charge carriers. As a charged particle passes through the detector, it ionizes the material in the depletion regions and the generated "holes" and free electrons drift to the junctions. The charge generated in this way can then be read out through the DAQ electronics, and digitized into the data stream. This design is used in all three systems in the CDF silicon and is common to all silicon strip detectors.

To describe the structure of the silicon detector, we must define the parts from which it is constructed. Each sub detector is comprised of barrels, layers, ladders, half-ladders, and strips proceeding from largest to smallest component. A strip is a single channel of silicon with the active sensor width equal to the pitch. These strips are deposited on wafers of semi-conductor that when combined with the readout processor, form a half-ladder. Two half-ladders are bonded together into a full ladder which is the smallest complete detector component containing high voltage and data aquisition functionality. These ladders are then mounted onto the silicon

space frame in layers, where a single layer is defined as a collection of ladders of the same radius. Finally, a silicon barrel is a z section of the detector containing the full complement of layers. Having defined the components of the silicon, the details of Layer 00, the SVXII, and the ISL are discussed.

Layer 00 resides closer to the interaction point than any other part of the CDF detector; it is mounted directly onto the Beryllium beam pipe. The beam pipe is 2.2 cm in diameter and a detailed view of the Layer 00 mounting is shown in Figure 4.9. The Layer 00 structure consists of two different widths of strips (8.4 mm and 14.6 mm) interleaved in a 12 sided pattern. This provides complete ϕ coverage, and z coverage extending ±78.4 mm from $z = 0$. The readout pitch of the silicon sensors is 50μm with the spacial resolution of a hit being $\approx 15\mu$m. Since it is mounted so close to the interaction region, Layer 00 was constructed of single sided p-in-n silicon wafers. Single sided sensors allow for higher bias voltages and greater radiation resistance from the intense environment close to the interaction region. Layer 00 is designed to be radiation hard up to $3fb^{-1}$ of delivered luminosity.

The SVX II detector is the primary piece of the CDF silicon detector, and includes the next five detector layers. The SVX II is constructed of three identical barrels, and 12 detector ladders per layer. An end view of the SVX II bulkhead with the layer and ladder layout is shown in Figure 4.8. Each ladder is 29 cm long and constructed of two double-sided half ladders. In order to provide z position information, each half-ladder has an axial side and a stereo side. The double sided design provides information about $r - \phi$ and z position while occupying the small footprint of a single sensor. The stereo side of layers 0,1, and 3 are perpendicular to the z axis, while the stereo angle of layers 2 and 4 are $-1.2°$ and $+1.2°$ respectively. Using the z position information, a 3D helix for each track can be reconstructed.
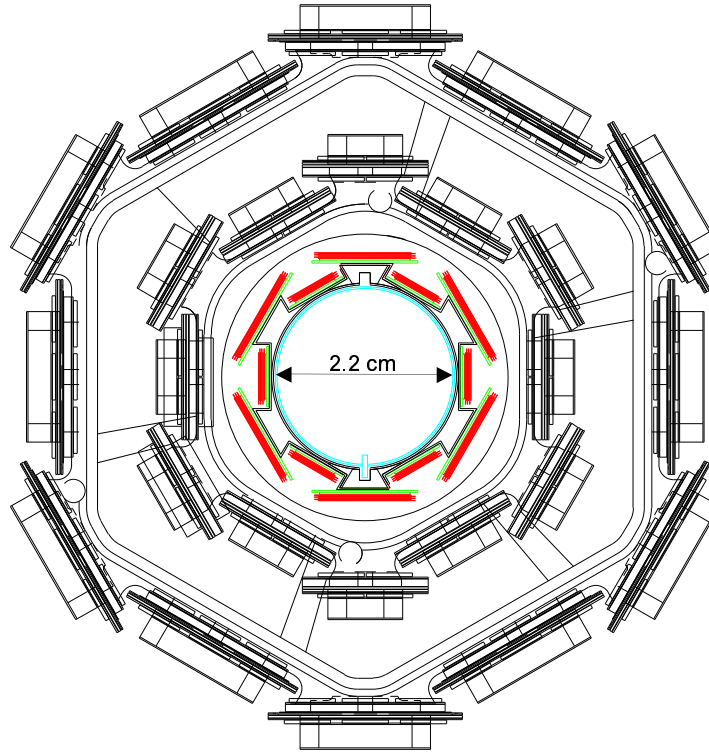
Figure 4.9: Detail of the Layer 00 Silicon along with the two innermost layers of the SVX Silicon.

The double sided technology of each sensor is accomplished by having the p-strips on the axial side and the n-strips on the stereo side. The axial strips have a pitch of 60 to 65μm with a position resolution of $\approx 20\mu$m.

The outermost three layers of the silicon tracker are the Intermediate Silicon Layer (ISL). These layers of silicon are constructed out of three barrels of double sided ladders constructed with axial and 1.2° stereo readout. The strip pitch for both sides of the ladder is 112 μm. Unlike the SVX ladders, the ISL ladders are constructed with three sensors per half ladder for a total of six sensors per ladder. The three barrels can be seen in Figure 4.7 and allow for stand alone silicon tracking out to an η of 2.0. This extended tracking region coupled with the relatively large

lever arm of the ISL allows for enhanced forward tracking.

Central Outer Tracker

The Central Outer Tracker (COT) is a 96-layer open-cell drift chamber used for charged particle tracking in the $|\eta| < 1.1$ region. The COT surrounds the silicon detector and extends to a radius just inside of the Time-of-Flight system. The mechanical structure of the COT is defined by two 1.4 m radius aluminum endplates separated by 310 cm in z. The inner and outer walls of the COT cylinder are made of 0.25 *in* aluminum sheet with the inner radius at 0.4 m. The tracking volume is divided into 8 super layers (SL), 4 axial layers (for $r - \phi$ measurement) and 4 stereo layers (for z measurement) with the structure shown in Figure 4.10. Each SL is then subdivided into cells by gold covered Mylar field sheets strung between the end plates. A cell contains twenty five 51μm diameter gold-plated copper-beryllium wires that alternate between potential and sense wires. The wire spacing is about 7.5 mm in all SL. Each wire is strung between the two endplates with a tension of 1.3 N, giving a total load on the endplates of 40 tons from all of the wires. At the center of the COT, a mylar wire support is epoxied to all of the sense and potential wires to provide additional electrostatic stability. The spacing between wires and the field sheets is just under 1 cm and varies slightly between SL. The design of three cells from SL2 can be seen in Figure 4.11. Ar-Ethane gas (60 : 40 mixture) fills the active chamber volume and both provides a source of ionized electrons and defines the drift velocity of the gas.

From the drift velocity and maximal path length, the maximum drift time is calculated. For the COT, the maximum drift time of about 100 ns, which is less than the proposed minimum Run 2B bunch spacing of 132 ns. The short drift time

1/6th East Endplate(s)
Units: centimeters [inches]

Layer #	1	2	3	4	5	6	7	8
	46.976 [18.494]	58.534 [23.045]	70.295 [27.675]	82.055 [32.305]	93.815 [36.935]	105.580 [41.567]	117.340 [46.197]	129.100 [50.827]
Cells	168	192	240	288	336	384	432	480
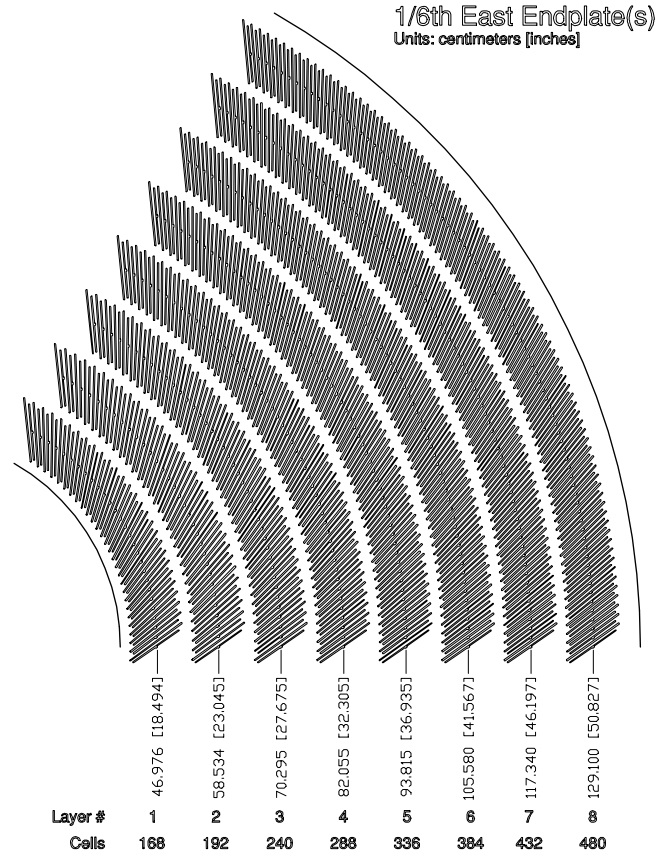
Figure 4.10: One eighth of the east COT endplate showing the cell configuration.

of the COT reduces the problem of shadowing hits. This occurs when a hit on a wire is missed due to occupancy from a previous event. Another consideration for constructing a drift chamber is the path the ionized particles will take in the static potential. Since the COT is contained within a magnetic field, electrons accelerated towards the sense wires by the high voltage will also experience a Lorentz force. In order to keep the path linear and azimuthal, the cells are tilted at an angle of 37°. This angle matches the angle at which the force from the magnetic field is completely canceled by the radial component of the electric field. The drift time resolution is better than 2 ns giving a single hit resolution of 150 μm. This hit resolution,
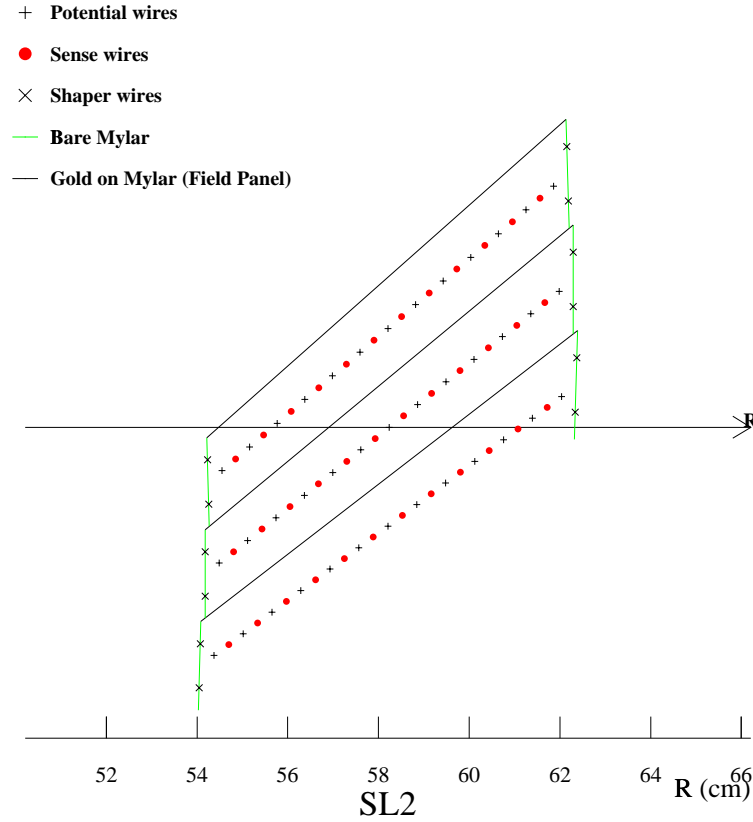
Figure 4.11: Three cells from super layer 2 of the COT. The wire spacing along with the Lorentz angle tilt is shown.

combined with the large lever arm, give the COT a momentum resolution of

$$\frac{\sigma_{p_T}}{p_T^2} = 0.15\% \tag{4.7}$$

where the momentum is in units of GeV/c. The large coverage of the COT along with the excellent momentum resolution make the COT the primary tracker for event reconstruction and triggering.

4.3.4 Calorimeter

Surrounding the tracking volume and solenoid, the CDF calorimeter modules measure the energy of particles produced from the $p\bar{p}$ collisions. Additionally, the segmentation of the detector provides a coarse position measurement. All of the calorimeters in CDF are based upon sandwiching scintillating material between layers of heavy material. As an electron or photon enters the electromagnetic calorimeter, it interacts with the heavy material generating a shower of photons, electrons and positrons. Similarly a pion, kaon, or hadron creates a shower of hadrons, mesons, and photons in the hadronic calorimeter. As the shower crosses the scintillating material, it excites the atoms of the scintillator which then radiate photons as they return to their ground state. The photons are collected using acrylic light guides leading to photomultiplier tubes (PMT). Integrating the charge collected in the PMT gives a measure of the energy deposited in the calorimeter. While the tracking system detects only charged particles, both neutral and charged particles are detected in the calorimeter. Specific showering materials allow sensitivity to either electromagnetic (high Z material) or hadronic (high A material) particles. In the CDF detector, the electromagnetic calorimeters are immediately followed by hadronic calorimeters. The calorimeter is divided into a central calorimeter covering $|\eta| < 1.1$, and a forward calorimeter providing coverage out to $|\eta| < 3.6$. A summary of the sub systems is given in Table 4.2, while the details of each are discussed in the following paragraphs.

The central calorimeter is the same detector as was used in the CDF Run 1 experiment. It is a cylindrically symmetric detector divided in half at $\eta = 0$. The two halves of the calorimeter are then segmented into 24 wedges of 15° in ϕ for a total of 48 modules. Finally, each wedge is divided into 10 projective towers such

Sub Detector	CEM	CHA	WHA	PEM	PHA
Coverage	$|\eta| < 1.1$	$|\eta| < 0.9$	$0.7 < |\eta| < 1.3$	$1.1 < |\eta| < 3.6$	$1.1 < |\eta| < 3.6$
Modules	48	48	48	24	24
η towers per module	10	8	6	12	10
Layers	31	32	15	23	23
Material	Lead	Steel	Steel	Lead	Iron
Radiation Length	$18\chi_\circ$	$4.7\lambda_\circ$	$4.5\lambda_\circ$	$21\chi_\circ$	$7\lambda_\circ$
Energy Resolution	$1.7\% + \frac{13.5\%}{\sqrt{E}}$	$\frac{80\%}{\sqrt{E}}$	$\frac{80\%}{\sqrt{E}}$	$1\% + \frac{16\%}{\sqrt{E}}$	$5\% + \frac{80\%}{\sqrt{E}}$

Table 4.2: Summary of the CDF calorimeters. The different components CEM, CHA, etc. are described in the text.

that each tower is 0.1 wide in η. Each central wedge contains an electromagnetic section followed by a hadronic section directly outside the electromagnetic. The central electromagnetic calorimeter (CEM) wedge contains 31 layers of 0.125 in lead interleaved with 5.0 mm polystyrene scintillator giving a total radiation length of 18 χ_0.

At the location of the shower maximum (6 χ_0), an Ar/CO_2 proportional strip detector has been inserted into each wedge. A view of one wedge of the central EM calorimeter is shown in Figure 4.12. This shower maximum detector contains orthogonal strips and wires, with the wires running parallel to the beam axis. The shower signal provides greatly improved shower location information than would be available simply from the towers of the wedge. In addition, the shower shape information from the detector can help in distinguishing single particle showers from multi-particle final states. This plays an important role in distinguishing the two photon decay of a π° from final state photons. In front of the CEM wedge, another proportional chamber, the central preradiator (CPR), measures the shower development of particles entering the calorimeter. This acts as a second discriminator
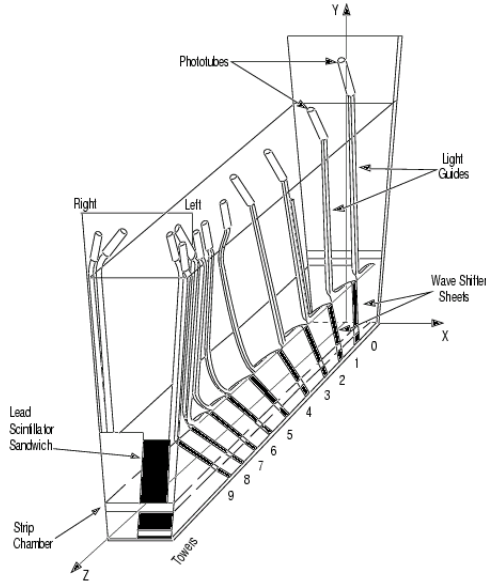
Figure 4.12: A central wedge showing the EM calorimeter segmentation and light collection.

between single and multi-particle final states which have a higher probability of radiating in the solenoid. Behind the CEM, the central hadronic calorimeter (CHA) is constructed of 32 layers of 2.5 cm steel interleaved with 1.0 cm scintillator. The segmentation of the CHA is exactly the same as the CEM, 15° in ϕ with 10 projective towers in η. Since the CHA is at a larger radius than the CEM, at higher η the CHA depth is not complete. In order to replace this missed coverage, the endwall hadron calorimeter (WHA) was constructed to fill the gap between $0.7 < |\eta| < 1.1$. For the WHA, 15 layers of 5.0 cm steel and 1.0 cm scintillator are used provided the same radiation depth as the CHA. The total hadronic absorption length is $\approx 4.7\Lambda_0$ for both the CHA and WHA. The energy resolution of the CEM is measured to be $1.7\% + \frac{13.5\%}{\sqrt{E}}$ as listed in Table 4.2.

4.3.5 Forward Calorimeter

The forward calorimeter is a completely new calorimeter for the more active environment of the Tevatron Run 2 and provides coverage in the region $1.1 < |\eta| < 3.6$. Two mirror pieces make up the calorimeter, one for the east side of the CDF detector and one for the west side. Figure 4.13 is a cross section of the top half of the west forward calorimeter showing how the calorimeter fits inside the endwall of the detector. Just as in the central calorimeter, an electromagnetic calorimeter (PEM)
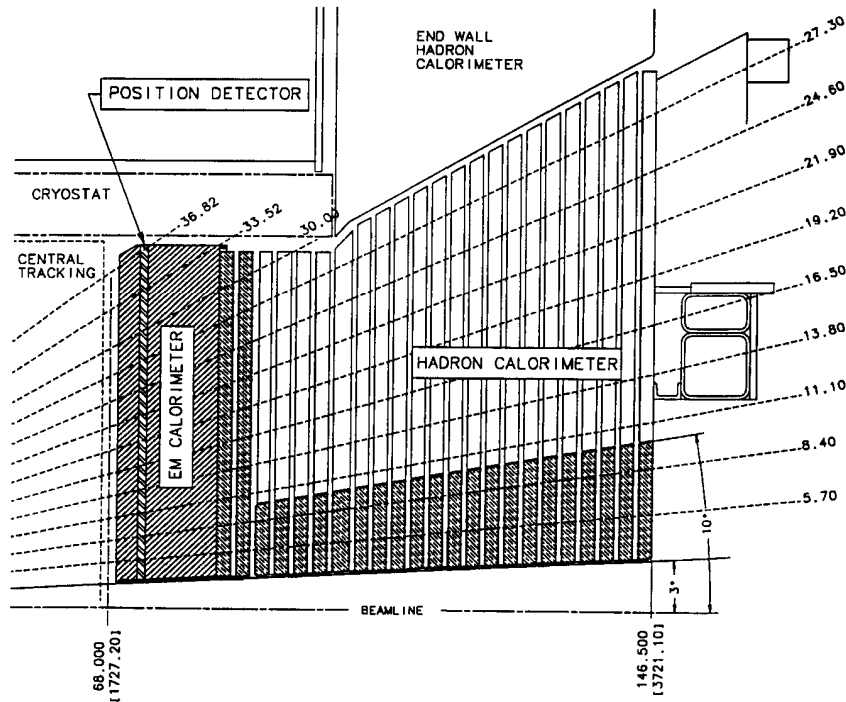
Figure 4.13: The forward calorimeter schematic.

is located in front of a hadronic calorimeter (PHA). Both the electromagnetic and hadronic sections have identical ϕ segmentation in the form of wedges, with each wedge covering $30°$. The transverse segmentation for the EM and hadron compart-

ments is identical and is shown for one wedge in Figure 4.14. The electromagnetic
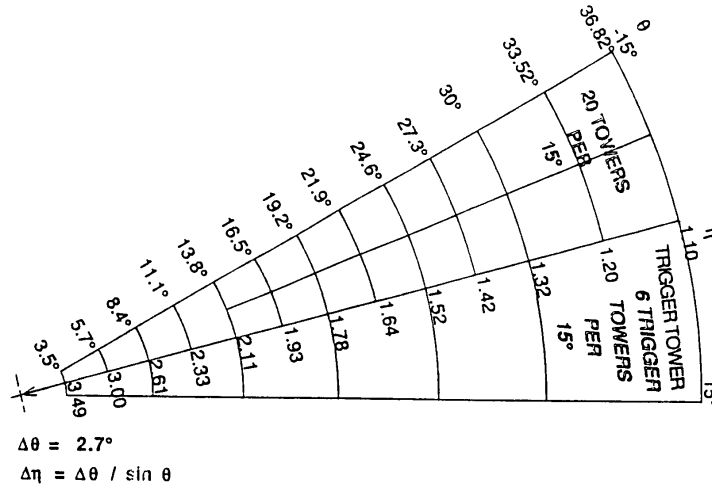
Figure 4.14: The transverse segmentation of a 30° section of the forward calorimeter. The upper wedge shows the physical segmentation, while the lower wedge shows the segmentation used in the trigger system.

section is constructed from 4.5 mm lead and 4.0 mm scintillator, with 23 layers giving a total radiation depth of $21\chi_0$. The hadronic section also has 23 layers but is made of 2.0 in iron and 6.0 mm scintillator with an absorption length of $7.0\Lambda_0$. This design gives an EM energy resolution of $16\%/\sqrt{E} \oplus 1\%$ for single electrons, and a hadronic resolution of $80\%/\sqrt{E} \oplus 5\%$ for single pions.

Similar to the central calorimeter, a shower maximum detector (PES) is located within the PEM. The PES is located in the fifth sampling slot, or at $\approx 6\chi_0$. It is constructed in 45° sectors with two layers, U and V, of 5 mm wide by 6 mm thick scintillating strips with varying lengths. The strips are aligned at $+22.5°$ and $-22.5°$ from the radial direction, see Figure 4.15. The high η region of the PES is also segmented from the low η region at $|\eta| = 2.60$. The higher η region has an occupancy two to four times higher than the low η section, thus demanding the
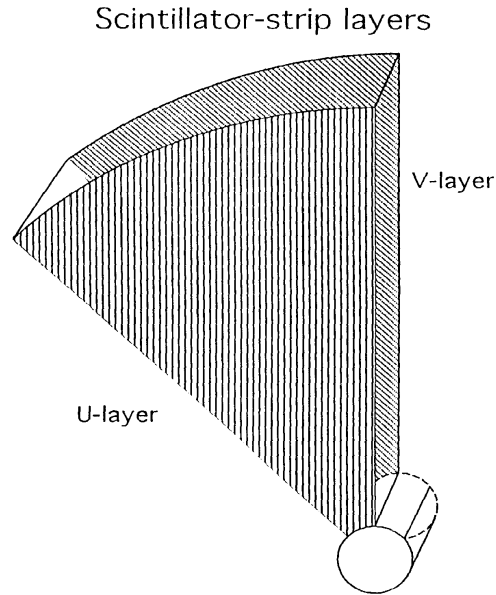
Figure 4.15: The geometry of the forward shower maximum detector showing alignment of the U and V layers.

division to avoid shadowing. Implanted in a grove in each scintillating strip is a 0.83 mm wavelength shifting fiber, which is grouped together with other fibers and readout by 16 channel PMTs. Table 4.2 contains a summary of the properties of the forward calorimeter.

4.3.6   Muon System

Outside of all other sub detectors is the CDF muon system. As can be seen from the generalized detector response in Figure 4.4, a high P_T muon will leave a track in the tracking volume but very little energy deposition in the calorimeter. This is due to the $\frac{1}{M^2}$ suppression of EM Bremsstrahlung [26] and the weak interaction of the muon. In order to distinguish muon tracks from electrons and pions that escaped the detector through cracks, drift chambers and scintillators are constructed behind the

calorimeter. Short track segments are reconstructed from the hits in these detectors and then matched to tracks in the tracking chamber. The muon system coverage is shown in Figure 4.16.
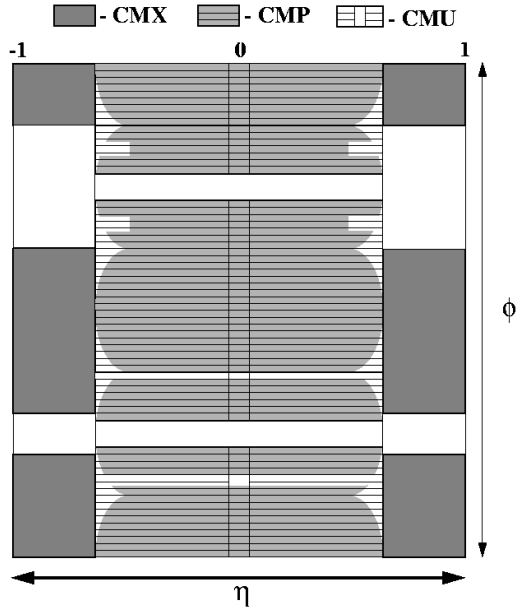
Figure 4.16: The muon system coverage for CDF Run 2.

4.3.7 Trigger and Data Acquisition

Since the Tevatron is a hadron collider with a huge interaction rate, CDF must use a filtering system to select scientifically interesting events from all of the events that take place during $p\bar{p}$ collisions. While hadron colliders have a higher available energy than comparably-sized electron colliders, this increased energy comes with the consequence that a bunch crossing will not always result in high P_t products since the interacting particles are composite particles. As well, the collision environment is very active due to the large number of hadronic remnants from the incident

proton and antiproton. In order to control the collection of information, and to not exceed the current data acquisitions limitations, a triggering system is used to filter and synchronize the recording of events. At CDF, a three-level deadtime-less online trigger has been integrated with the data acquisition system. The trigger allows for the event storage rate to be reduced from the bunch crossing rate of 2.5 MHz, to a rate within the limits of the DAQ system, 100 Hz. The structure of the trigger is shown in Figure 4.17 and the details of each level of the trigger will be discussed next.

Level 1

The Level 1 (L1) trigger uses custom designed hardware and low level information to make the most primitive decisions about events. Within the DAQ electronics of each detector component, there is a 42 bucket data pipeline. The pipeline is synchronized with the Tevatron master clock which has a period of 132 ns. For each crossing, data enters the pipeline and a trigger decision must be made before the data reaches the end of the pipeline. Otherwise if no decision is made, the data is lost. This translates to a decision time of $5.544\mu s$ for the Global L1 Trigger. During this decision time, uncalibrated data is collected from the calorimeter, COT, and the muon detector and fed to three possible synchronous streams. The calorimeter stream decision is based upon the energy deposited in calorimeter cells, along with the magnitude of unbalanced transverse energy. The eXtremely Fast Tracker (XFT) uses information from the COT to reconstruct tracks and makes decisions based on the number and transverse momentum of tracks. Finally, the muon stream uses information from the XFT to match tracks to muon stubs in order to trigger on muon candidates. The dataset used in this analysis was collected while the Tevatron operated in 36

**Dataflow of CDF "Deadtimeless"
Trigger and DAQ**

Detector

7.6 MHz Crossing rate
132 ns clock cycle

**L1 Storage
Pipeline:**
**42 Clock
Cycles Deep**

L1 trigger

Level1:
7.6 MHz Synchronous pipeline
5544ns latency
<20 kHz Accept rate

L1 Accept

L2 Buffers:
4 Events

L2 trigger

Level 2:
Asynchronous 2 stage pipeline
~20μs latency
300 Hz Accept Rate

L2 Accept

L1+L2 rejection: 20,000:1

DAQ Buffers

L3 Farm

**Mass
Storage**

PJW 10/28/96

Figure 4.17: The three level deadtime-less trigger used to control the DAQ of the CDF detector.

bunch mode, meaning that the bunch spacing was 396 ns. The maximum accept rate for the L1 trigger is $20kHz$, but the nominal accept rate during data taking was $12kHz$.

Level 2

Having passed the requirements of a L1 trigger, an event is then passed to the Level 2 (L2) trigger. As opposed to using a data pipeline, at L2 data is written into one of four data buffers within the DAQ electronics of each detector component. These buffers differ from a data pipeline in that the data is resident in the buffer until a decision is made, and will not be lost. So while the data in a buffer is being processed, it cannot be overwritten by another event accepted from L1. If a L1 accept does occur while all four L2 buffers are occupied, then deadtime is incurred. In order to minimize deadtime, the latency of the L2 decision must be less than approximately 80% of the average time between L1 accepts. Therefore, the L2 latency is designed to be $20\mu s$. In order to achieve this, two asynchronous processes have been programmed on a custom Alpha processor, with each process having a decision time of $10\mu s$. The L2 trigger uses all of the data collected for the L1 trigger along with information from the shower maximum and SVX detectors. The data is also processed with higher granularity giving better resolution and identification than that available at L1. Using the improved resolution, more stringent cuts are applied to the identification of particles along with a jet clustering algorithm. The L2 trigger is designed to work with a maximum accept rate of 300 Hz, while the accept rate during data taking varied from 100 Hz to 300 Hz depending on the instantaneous luminosity.

Level 3

The Level 3 (L3) trigger consists of two components, the event builder and the L3 processing farm. The event builder consists of custom built hardware used to assemble and package all of the information from a single event. The L3 processing farm is composed of 16 different subfarms, with each subfarm containing 16 dual CPU processing nodes. These components, along with the ethernet infrastructure, constitute the L3 trigger. Once a L2 accept has been issued, the data in the L2 buffers are collected from the Front End crate and sent over fiber optic lines to the event builder. The digital information from each detector are then collected and the information aligned based upon the bunch counter. This critical step makes sure that the information from different bunch crossing is not mixed together. Once the entire event has been packaged together, the data is fed to the farm of processors for complete event reconstruction. While at L1 and L2 the data are resident in the readout crate, at L3 all of the data for an event are together in one processor. As well, the designed latency for the L3 trigger is a full second, meaning that a full event reconstruction can take place as opposed to a decision based on primitives. With the greater processing time, calibration information is applied to the data in order to give the best possible resolution. A trigger decision is then made based upon detailed particle identification and event topology. Details of the event reconstruction will be discussed later. Once an event is accepted, the event is sent from the L3 processing node to permanent storage for later complete offline reconstruction. The accept rate from the L3 trigger is determined by the rate at which data can be written to tape, and was approximately 75 Hz during the current data period.

4.3.8 Data Processing

All events passing a L3 trigger are collected from the detector and processed with the CDF Offline reconstruction. The reconstruction software applies the calibration information to the raw data from each subdetector and uses the calibrated data to reconstruct detector objects such as silicon and wire chamber tracks, calorimeter clusters, and muon stubs. These detector objects are next associated together to form candidates for physics objects such as electrons, muons, jets, etc. A custom software framework written using the C++ programming language was designed to perform these tasks for every event. Once the raw data of an event has been reconstructed, the event is written to magnetic tape for permanent storage. The event is then ready to be analyzed in order to search for a specific final state produced from the $p\bar{p}$ collisions. The details of the analysis and selection of $p\bar{p} \rightarrow W \rightarrow e\nu + \gamma + X$ events are described in the Chapter 5.

Chapter 5

Data Sample, Reconstruction, and Selection

From the collisions generated in the Tevatron, events matching the $W\gamma$ final state are filtered and selected for analysis. This analysis focuses on the electron decay of the W, and uses a high transverse-momentum (P_T) electron trigger that selects events containing electron candidates. Once in permanent storage, an object-oriented offline reconstruction program analyzes each event, generating physics objects from the detector data. $W\gamma$ candidate events are selected from reconstructed events with high-P_T electrons in the central and forward calorimeters, while the photon selection is limited to the central calorimeter. The details of the trigger, event reconstruction and event selection are discussed in this chapter.

5.1 Trigger

In order to filter events containing a $W\gamma$ boson pair from other interactions, a trigger path was chosen based upon high-P_T electrons from the decay $W \rightarrow e\nu$. Of the three final state particles, the γ, ν, or electron, it is the last two objects that are the most viable for triggering. The γ is a poor choice, since the analysis covers events with photon transverse energies as low as 7 GeV, and these are easily

faked in the low resolution of the hardware trigger. A photon trigger threshold low enough to accept all of these events would be unacceptable, as it would overwhelm the DAQ system with background events. With its large rest mass, the decay products of the W boson are highly boosted in the transverse plane. Such high-P_T objects have low backgrounds and can be selected with acceptable trigger rates. Considering the two W decay products, the $\not{E}_T$ resolution of a neutrino depends upon the proper calibration of the entire detector and upon resolving the z position of the interaction. With the limited processing time of the hardware trigger, it is difficult for online discrimination and a lower threshold would be necessary in order to accomplish a high efficiency.

The charged lepton produces a signal in both the calorimeter and the tracker that can be matched in coincidence. The trigger for $W \rightarrow e\nu$ events is therefore based upon the high energy electron or positron. For electrons in the central calorimeter, events are selected using only this single object selection. For W decays with electrons in the forward calorimeter, the tracking coverage does not allow for coincidence between the calorimeter and tracking information. To overcome this, a trigger decision based on both the electron calorimeter information and missing transverse energy is used to select events. Using these two triggers, the data events were selected for analysis as $W\gamma$ candidates. The detailed requirements of each trigger path are described in the next section.

5.1.1   Central Electron Trigger

The central electron trigger selects electron candidates with E_T greater that 18 GeV. The average event rate during the data taking period was 1 Hz, which corresponds to a cross section of approximately 50 nb. In order to have well understood trigger

efficiencies, a strict trigger path requirement was used in the analysis. This means that for an event to be considered at L2, it must have passed the prerequisite L1 trigger. Similarly at L3, the event must have passed the prerequisite L2 trigger. The trigger efficiency is then the simple product of the individual trigger efficiencies.

- Level 1: (L1_CEM8_PT8) This requires a central electromagnetic (EM) cluster with $E_T^{EM} > 8$ GeV and $E_{HAD}/E_{EM} < 0.125$ for clusters with energy less than 14 GeV. An XFT track with $P_T > 8$ GeV/c must be matched to the trigger tower containing the EM cluster.

- Level 2: (L2_CEM16_PT8) This requires a central EM cluster with $E_T^{EM} > 16$ GeV and the ratio $E_{HAD}/E_{EM} < 0.125$ for all clusters. An XFT track with $P_T > 8$ GeV/c must be matched to the L2 cluster.

- Level 3: (L3_CENTRAL_ELECTRON_18) The final filter requires a central EM cluster with $E_T^{EM} > 18$ GeV and $E_{HAD}/E_{EM} < 0.125$. A fully reconstructed 3D track with $P_T > 9$ GeV/c must be matched to the seed tower of the EM cluster.

5.1.2   Forward Electron Trigger

The forward electron trigger selects events with both a high-E_T electron candidate and missing transverse energy. The average event rate during the data taking period was 0.5 Hz, which corresponds to a cross section of approximately 25 nb. Again, a strict trigger path was required for simplicity of efficiency calculation.

- Level 1: (L1_EM8_MET15) This requires an electromagnetic (EM) cluster with $E_T^{EM} > 8$ GeV and $E_{HAD}/E_{EM} < 0.125$ for clusters with energy less

than 14 GeV. The $\not{E}_T$ must be greater than 15 GeV with the z coordinate of the interaction assumed to be zero.

- Level 2: (L2_PEM20_MET15) This requires a forward EM cluster with E_T^{EM} > 20 GeV and the ratio E_{HAD}/E_{EM} < 0.125 for all clusters. There is an implicit cut on the $\not{E}_T$ since only events passing the L1_EM8_MET15 trigger are considered for L2.

- Level 3: (L3_PEM20_MET15) The final filter requires a forward EM cluster with E_T^{EM} > 20 GeV and E_{HAD}/E_{EM} < 0.125. The $\not{E}_T$ as calculated in the L3CdfMet module using $z =0$ must be greater than 15 GeV.

For events passing these two trigger paths, the raw data was written to permanent storage for processing at a later time.

5.2   Event Reconstruction

All events recorded from the detector are processed offline with an event reconstruction program. During this process the raw detector data is calibrated and constructed into objects that are analyzed for particle identification. Some of these basic objects are electromagnetic (EM) clusters, jets, tracks, and muon stubs. At CDF, the offline reconstruction processing is performed by object-oriented software written for use by all collaborators. The details of the different reconstruction modules give insight into the objects and quantities available for particle identification. The focus of this section is on the modules used in the selection and analysis of $W\gamma$ $\rightarrow e\nu\gamma$ events.

5.2.1 Calorimeter Clustering

The energy deposition of a final state particle is very rarely contained within a single calorimeter tower. (*e.g.* a typical single tower is 0.1 in η and 15° in ϕ.) Therefore, the lead tower and the adjacent towers must be clustered together for an accurate measurement of the incident particle and its kinematics. There are several clustering strategies within the event reconstruction that combine individual towers into a single object. The two strategies used in this analysis are EM clusters and jet clusters. Here, the term "jet" refers to the collection of a particles created when a quark or gluon hadronizes into a shower of particles. Each strategy has been optimized toward a specific final state particle and the details are discussed below.

Electromagnetic Clustering

The electromagnetic clustering is optimized to reconstruct objects that will be identified as either an electron or photon [27]. The EM clusters generated from clustering have a measured energy resolution of $1.7\% + \frac{13.5\%}{\sqrt{E}}$ in the CEM and $1\% + \frac{16\%}{\sqrt{E}}$ in the PEM. The initial step in the clustering is to apply tower-to-tower calibrations and to sort the towers by E_T considering only towers with greater than 100 MeV of energy. At this stage the event vertex is assumed to be located at $z = 0$ for all transverse calculations. Starting with the highest E_T tower, a tower is considered a seed tower if its E_T is greater than 2 GeV. The neighboring towers are now considered for addition to the cluster. For a tower to be added to the cluster it must be located within the same detector as the seed tower. (e.g. PEM towers are not considered for CEM clusters, and vice versa.) Because the geometry of the detectors is different, the clustering strategy varies between the two detectors and the candidate neighboring towers are different in the CEM and PEM. Although the

exact shape of the towers varies between the central and forward, the typical size of a cluster is the same in both, 0.2 in η and 15° in ϕ.

In the CEM, only towers that neighbor the seed tower in η are considered for the cluster. Therefore a CEM cluster will be completely contained within a single wedge. If the neighbor tower has an E_T greater than 100 MeV it is added to the cluster. For this criteria, both EM and hadronic energy is considered so that the tower would contribute to any future cut on hadron/EM energy ratio. This tower is now removed from the possible seed list, and will not be considered as a seed for a separate EM cluster. After considering all neighbor towers, a CEM cluster will have 1, 2, or 3 towers contained in the cluster.

In the PEM, all towers sharing a border or corner with the seed tower are considered neighbor towers. There are then 8 possible neighboring towers that can be added to the seed tower. These 8 towers are sorted by EM E_T. If it has an E_T greater than 100 MeV, the highest E_T tower is selected as the seed tower's daughter. The clustering now searches for a pair of towers to combine with the seed and daughter towers to make a 2 × 2 tower cluster. It considers all 2 × 2 combinations, and selects the one with highest E_T. If the additional pair of towers has an E_T greater than 100 MeV, then the towers are added to the cluster. This algorithm most commonly produces 4 tower clusters in a 2 × 2 configuration.

The electromagnetic clusters formed by these algorithm are the starting point for the identification of photons and electrons.

Shower Maximum Clustering

To provide better position resolution and multi-particle discrimination, the shower maximum signal from an EM object is reconstructed. The showermax response to a

particle is normally distributed across several channels. Thus, to accurately resolve the response, channels must be grouped into clusters. Since the central and forward shower max detectors are different, the details of the clustering vary, but the general strategy is the same. For a given view, the channels in a wedge are scanned for a channel above threshold. (In the CES, the views are perpendicular to each other and the cluster location is measured in z and ϕ coordinates. In the PES, the two views are oriented $45°$ to each other and the cluster location is determined in x and y coordinates.) When a channel is found above threshold, the surrounding channels are scanned to see if they are above the shoulder threshold. If so, they are added to the cluster with a maximum channel width of 11 in the CES and 9 in the PES. Once all of the surrounding channels have been considered, the profile of the shower shape is then compared with profile templates of single particle test beam. Finally, the centroid of the shower max cluster is measured and used as the location of the electromagnetic cluster in the view considered. The showermax clusters in each detector are reconstructed with a position resolution of 1 mm, and when associated with an EM cluster, allow for a precision measurement of the candidate particle's position.

Jet Clustering

The jet clustering is designed to cluster many particles together as a single object within the event. In offline reconstruction, several different jet clustering algorithms are available [30], but this analysis used a seeded, cone-based algorithm exclusively. This clustering algorithm produces jets with an energy resolution of $\frac{68\%}{\sqrt{E}}$ [31]. The clustering begins with seed towers, where all of the towers with energy greater than 1 GeV in the calorimeter are considered as possible jet seeds. Once a seed tower

has been chosen, the center or the tower becomes the geometric center, (η_C, ϕ_C), of a cone of radius R. A tower, t_i, is added to the jet cluster if it lies within the radius R as show in Equation 5.1.

$$\sqrt{(\eta_i - \eta_C)^2 + (\phi_i - \phi_C)^2} \leq R \tag{5.1}$$

For this analysis, a cone radius of 0.4 is used. After adding the towers inside of the cone to the cluster, the E_T-weighted centroid of the cluster is calculated and the geometric center of the cluster is set to this centroid. The procedure is then iterated with the new geometric center, until a stable configuration is found, producing a jet object. Both the electromagnetic and hadronic energy is used in the creation and measurement of a jet since the hadronization produces both hadronic and electromagnetic particles.

5.2.2   Missing Energy

When a neutrino traverses the detector, the chance of energy deposition is extrememly small. But conservation of momentum requires that such an "invisible" particle be recognized by an energy imbalance or missing energy. The missing transverse energy for an event is calculated from all of the calorimeter towers within the region $|\eta| < 3.6$, both central and forward calorimeters. The towers are required to have greater than 100 MeV of energy to contribute to the calculation. Both the hadronic and electromagnetic energies are used in calculating $\not{E}_T$. As with the other basic clustering algorithms, the event vertex is initially assumed to be at $z = 0$ in the trigger and offline, and is later corrected for the measured event vertex from the electron or muon from the W decay. For events containing reconstructed muons,

the calorimeter response from the muon is removed, and the $\not{E}_T$ corrected with the P_T of the muon track. The last correction to the $\not{E}_T$ is applied after correcting the measured energy of jets in the event. The equation for the corrected missing transverse energy is the negative vector sum of the transverse energy of the corrected jets and the towers as shown in

$$\not{\vec{E}}_T = -\sum_i^{jets} E_T^i(corr)\hat{\phi}^i - \sum_j^{tow} E_T^j\hat{\phi}^j \qquad (5.2)$$

Here, $\hat{\phi}$ is a unit vector in the $r - \phi$ plane pointing to the center of the jet or calorimeter tower. E_{Ti}^{jet} is the corrected transverse energy of the ith jet, and E_T^j is the corresponding transverse energy measured in the jth unclustered calorimeter tower. The jets corrections are discussed in detail in Section 5.2.5. The resolution of the $\not{E}_T$ is dependent upon the response of the entire calorimeter and is measured to be $(0.646 \pm 0.016)\sqrt{\sum E_T(GeV)}$ [28].

5.2.3 Track Reconstruction

Tracks are a key component in the identification of particles. Having efficient and precise reconstruction is crucial for the analysis of events. Two tracking algorithms are use to identify charged particles traversing the detector in the offline reconstruction. For particles that cross the central calorimeter and COT, a hit-based, unseeded tracking reconstruction is used. But particles that enter the forward calorimeter cross only a small section of the COT, and so a seeded tracking algorithm based upon an event vertex and calorimeter objects is used to reconstruct tracks in the SVX detector. This seeded SVX tracking algorithm is called Phoenix tracking. The details of the two algorithms are now discussed.

COT Tracking

The central track reconstruction algorithm uses several different strategies to form 3-dimensional charged-particle tracks [29]. The resulting 3D tracks have a transverse momentum resolution of $\sigma(P_T) = 0.15\% P_T^2$ with unit of GeV/c. The reconstruction begins with individual hits of the COT channels. After timing calibration, the initial segment-finding algorithm groups hits in the axial super layers (SLs) into segments based upon both the hit location within the cell and the timing of the hits. During the initial segment-building procedure, hits in a SL may be shared by two different segments. But after the processing is finished within the SL, only the segment with the greater total hits retains the shared hit. After completing the construction of the axial segments, a histogramming algorithm is run to create additional segments that the initial segment finder may have missed. The second set of segments is then merged together into the initial segment link. Once segments have been formed in all of the axial SLs, these segments are linked together to form 2D tracks in the $r - \phi$ plane. The segment finding algorithm is then repeated in the stereo layers. These additional segments are now considered for addition to the 2D tracks in order to provide z information. If a 2D track does not have any stereo hits after the stereo segment linking, the individual hits in the stereo layers are considered for addition to the track. If enough stereo hits are successfully matched to the track, the hits are retained for track z information. After the addition of the stereo segment, the tracks now have full P_T and 3D orientation information. The efficiency of the COT tracking reconstruction was measured using central electron W events triggered without any track requirement. It was found to be 99.3% [50] for these high-P_T isolated tracks.

Phoenix Tracking

While the COT tracking is a general-purpose tracking algoritm, the Phoenix track-ing is designed specifically for forward high-P_T electromagnetic objects. The algo-rithm begins by looking for an event vertex, discussed shortly, that is resolved from COT tracks. After finding a candidate vertex, the algorithm looks for electromag-netic clusters in the event. If a cluster is found, the location is determined from the shower maximum detector and the cluster E_T measured from the calorimeter energy deposition. Using the event vertex location, the cluster location, and the E_T of the cluster, two roads are constructed between the two points, one for a positive particle and one for a negative. The SVX detector is then scanned along these two paths for hits that match the possible particle trajectory. The result is a high-precision track of the particle in the busy environment next to the interaction point. Since track-ing in the forward region is seeded by the calorimeter, the momentum resolution is highly correlated with, and dominated by, the energy resolution of the calorimeter. While the position resolution of the track is very precise, the transverse momentum resolution for high-P_T tracks is highly correlated to the PEM cluster resolution. This is due to the fact that the PEM cluster seeds the Phoenix algorithm. The efficiency of the Phoenix tracking algorithm is measured from $Z \rightarrow ee$ events and determined to be $83.2 \pm 1.0\%$ [51].

5.2.4   Event Vertex Reconstruction

For events with a well-reconstructed central, high-P_T track, the track is used to set the z location of the interaction. But for events without such a track, such as forward electron events, the vertex must be constructed from a more global reconstruction of the event. Without an accurate event vertex, it is impossible to know at what

point along the beam path the hard scatter took place. Once this is determined, the event kinematic quantities can be calculated correctly. A COT track based vertex algorithm is used to reconstruct the location of the hard scattering in the $p\bar{p}$ collision. Tracks reconstructed in the COT are grouped together based upon their $z0$ when projected to the beam spot. For tracks to be added to the vertex they must be within 1 cm of the vertex seed. The vertex location is then calculated by a weighted average of the tracks that have been grouped into a vertex. If there are multiple vertices in an event, then the vertex with the highest sum of associated track P_Ts is chosen as the event vertex.

5.2.5   Calibration and Alignment

During normal operation of the detector, the response of the detector changes slowly. In order to compensate for this chance in response, the detector is calibrated during the offline processing. The calibrations correct for both geometric response and time dependent effects. The corrections are measured from low background, tightly selected control samples. The procedure to determine each correction is discussed below.

Central Electromagnetic Response

The energy of the electrons and photons in the central region comes from the response of the central EM calorimeter. To improve the precision of the CEM measurement, we correct the energy for three effects: response variations based upon the x and z location within the tower, time-dependent tower-to-tower variation, and the overall scaling.

The response of the CEM is not constant across the face of the entire wedge.

As a shower gets closer to the edge of a tower, the calorimeter response decreases. Using 1994 test beam data, a "face correction" was determined from the measured response map [32]. The light attenuation in the scintillator and light loss into the wavelength shifting fibers is also accounted for in the correction. This initial correction is applied to all central EM objects in the data and simulated data. Within the data, an additional correction to the face correction was found to be needed. Using early electron events collected prior to the data sample for this analysis, the average E/P for each tower is calculated in the range $0.8 - 1.25$ [33]. Here, E is the energy measured in the calorimeter, and P is the momentum of the COT track associated with the CEM cluster. The average E/P value was found to depend upon the local x coordinate within the tower. To correct for this, the following correction was applied to the data

$$E_T^{corr} = \frac{1.015}{1 + 0.000157x^2} \times E_T \qquad (5.3)$$

Here, x is the distance from the center line of the tower in cm.

To correct for response variation between individual towers, a tower-to-tower correction is measured from the data. Using an electron similar to that used for the face correction but spanning the full data sample, the average E/P distribution in a tower was measured over time. The inverse of this average value is applied to the data so that the final measured average E/P is unity. The tower-to-tower correction is only applied to the data since the tower response in the simulated data is uniform. A 5% improvement in the energy resolution is seen after applying the correction.

While the other calibrations make the CEM response flat in time and local coordinates, the absolute energy scale must still be calibrated. In order to do this,

the energy scale is set by selecting a highly pure sample of $Z \rightarrow ee$ candidates in the central detector. With the Z mass very accurately determined by many experiments, the di-electron invariant mass spectrum is fit to a Gaussian distribution within one decay width of the Z boson mass. The CEM response is then iteratively tuned such that the fitted distribution matches the Z mass of 91.18 GeV/c^2.

These calibrations are applied to both electrons and photons in the central region, since the response to either particle should be identical within the calorimeter sampling section.

Forward Electromagnetic Scaling

For the forward electromagnetic calorimeter, a face response and a time dependent energy scale correction is applied. The face response of the forward calorimeter was performed using a 57 GeV e^+ beam [34], and scanning across the face of one wedge covering 60°. The towers within a wedge vary in size, and so a separate correction is determined for each tower. This map is then applied to all ϕ regions as no significant variation between ϕ wedges was found.

Studying the response of the PEM during the data taking period, a time dependent degradation of the measured energy is found. At two points during the data taken, extended access to the detector allowed for the degradation to be corrected with online calibration procedures. Even with these corrections, measuring the mass of di-electron events with one electron in the forward calorimeter showed that the absolute scale was incorrect. Therefore, using the same method as performed in the central, the PEM scale was iteratively scaled in three time periods so that the di-electron invariant mass matches the Z mass [35]. The scaling applied to the PEM energy is listed in Table 5.1 and the resulting Z mass distribution shown in

Figure 5.1.

Calor. Side	Run < 159600	159600>= Run < 163600	Run > 163600
East	1.036	1.071	1.089
West	1.031	1.066	1.071

Table 5.1: Run dependent energy calibrations for the east and west forward electromagnetic calorimeters. This measurement was done including the PPR energy in the EM cluster. This analysis does not include the PPR energy when calculating the energy of a PEM cluster, and so an additional scale of 1.026 in the East, and 1.020 in the West was measured. This additional scaling is applied independent of run number.
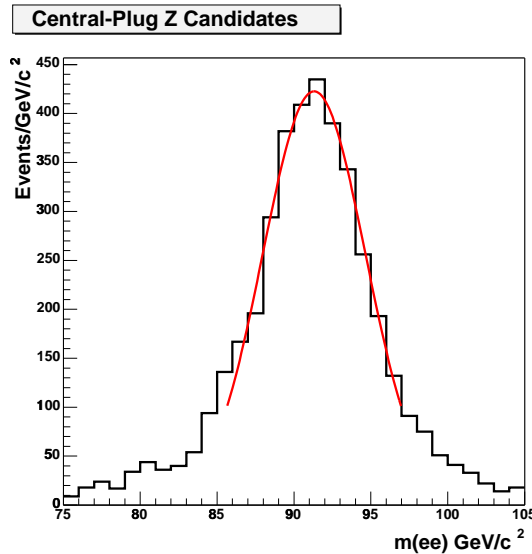
Figure 5.1: The invariant mass of di-electron candidates with one electron in the central calorimeter and one in the forward calorimeter. The data is fit to a Gaussian distribution with a mean value of 91.2 GeV/c^2 and a width of 3.3 GeV/c^2. This resolution matches well with the predicted resolution seen in Monte Carlo samples.

Beam Constrained Tracking

For tracks in the COT associated with electron candidates, the track is constrained to have originated from the x and y coordinate of the beam spot. Since W bosons

have extremely short decay times, we model the decay products as being generated at the location of the hard scattering. To implement this in the reconstruction, an additional "hit" located at the beam spot is attached to the track. The beam spot is measured for each Tevatron store, and is calculated as the average of the point of closest approach to the beam for all tracks in the store. The measured error on the x and y coordinates of the beam spot location is about 30 μm. Once the beam spot has been attached to the track, all of the fit parameters are recalculated and show improved precision.

Curvature Correction

When measuring the E/P distribution, a bias is seen as a function of azimuthal angle ϕ. The effect is mirrored between electrons and positrons. The bias is caused by misalignment within the COT, and the misreconstruction of COT hits in the offline processing. The signed transverse momentum, Q/P_T, is corrected using

$$\frac{Q}{P_T^{corr}} = \frac{Q}{P_T} - 0.00037 - 0.00110 \times \sin(\phi + .28) \qquad (5.4)$$

where Q is the charge of the track, P_T the beam constrained transverse momentum in units of GeV/c, and ϕ the azimuthal angle of the track. After applying this correction, the E/P distribution is flat as a function of ϕ, and equal for electrons and positrons.

Jet Corrections

When a jet object is created in the jet clustering algorithm, a large region of the detector is spanned in order to collect all of the energy. But when covering such a large area (a cone of 0.4), the jet cone crosses several cracks within the calorimeter

and also areas that may contain low-energy particles not originally from the final-state parton that created the jet. In order to correct for these problems, five different jet corrections [36] are made:

- The variation in the calorimeter tower response is corrected by applying offline calibrations

- Relative jet-energy corrections correct the jet response to be flat in η. This compensates for both the tower geometry, and for particles that may have entered a detector crack and gone unmeasured.

- The energy from multiple interactions is removed from the jet cone using the number of reconstructed vertices in the event.

- The absolute energy scale of the jets corrects the E_T of the jet to match the E_T of the partons within the jet cone. The absolute energy scale is measured using photon + jet balancing, measuring the hadronic calorimeter response to muons, and finally tuning the simulation response from parton showers to jets.

These jet corrections are applied to all jets in the event within $|\eta_{jet}| < 3.6$. The corrected jet E_T is then used to recalculate the missing transverse energy described earlier.

5.3   Particle Identification Variables

After the events are processed with the offline reconstruction software, electron and photon candidates are selected. Selection cuts are made based upon quantities derived from reconstructed objects, and associations between these objects. The

identification variables act both to identify a particle, measure the momentum, and define the event topology. Because the sub detectors are constructed differently, the selection is different for central and forward particles. The CEM electron, PEM electron, and CEM photon identification variables are defined in Appendix A, while the applied cuts are listed in the next section.

5.4   Event Selection

$W\gamma$ candidates events are selected by reconstructing the heavy boson leptonic decay, and then selecting at least one isolated photon candidate. Selecting an isolated, high-P_T electron and large missing E_T gives a low background W sample that is used as the base sample for the $W\gamma$ selection. Several cross checks can be performed on the W sample to ensure high purity and good understanding of the selection. The inclusive W cross section is compared to the prediction of NNLO calculations, and the shape of the transverse momentum of the W is compared to that expected from detector simulation. After validation of the base sample, an isolated photon, well separated from the electron, is selected to complete the $W\gamma$ sample.

5.4.1   W selection

Using the objects selected by the high-E_T central and forward trigger, an electron candidate is first selected within either the central calorimeter or the forward calorimeter. The electrons are required to have a high transverse energy deposition in the EM calorimeter, along with being matched to a reconstructed charged particle track. Additionally, the electron candidate must have a shower profile and development consistent with an electron, and be isolated from other activity in the

detector. The detailed requirements and cuts used to identify electron candidates in the CEM are listed in Table 5.2. The corresponding requirements and cuts for electron candidates in the PEM are listed in Table 5.3. The quantities listed in the tables are defined in Appendix A.

Central Electron	
E_T	> 25 GeV
$|\eta|$	< 1.0
P_T	> 10 GeV
N_{Ax}^{track}	> 2
N_{St}^{track}	> 2
Had/Em	$< 0.055 + 0.00045 \cdot E$
E/P	$< 2 || P_t > 50$ GeV
$Isolation/E_T$	< 0.1
χ^2_{strip}	< 10
ΔX	$-3.0 < q \cdot \Delta X < 1.5$ cm
$|\Delta Z|$	< 3 cm
L_{shr}	< 0.2
Fiducial	true

Table 5.2: Cuts used to select electron candidates in the central calorimeter.

Additionally, the event vertex must be located within the fiducial region of the detector, $|Z_{vtx}| \leq 60$ cm. As described in 5.2.4, for central electron events the cut is applied to the high-P_T track $z0$. In forward electron events, the vertex reconstructed from central drift chamber tracks is required to be within 60 cm.

After this selection, the $\not{E}_T$ of the event is required to be greater than 25 GeV. Then the transverse mass of each candidate is computed, since the longitudinal component of the neutrino momentum cannot be measured. The equation for the transverse mass is shown in Equation 5.5.

$$M_T = \sqrt{2p_T^l \not{E}_T (1 - \cos \phi)} \qquad (5.5)$$

Forward Electron	
E_T	> 25 GeV
Had/Em	<0.05 if $(E <= 100)$
	$< 0.05 + 0.026 \cdot \ln(E/100)$ if $(E > 100)$
$Isolation/E_T$	< 0.1
PES 5×9 u and v	$> 0.65 \lVert E_T > 100$ GeV
Fiducial base on PES	$1.2 < \lvert \eta \rvert < 2.6$
PEM3x3 χ^2	< 10
PEM FitTowers	> 0
Matched Phoenix Track	true
NSvx Hits	$>=3$

Table 5.3: Cuts used to select electron candidates in the forward calorimeter.

Here, ϕ is the difference in azimuthal angle between the lepton momentum and the missing transverse momentum vector. The transverse mass distribution for the full dataset before cuts is shown in Figure 5.2. For the W boson selection, M_T is required to be in the range $30 < M_T < 120$ GeV/c^2. The total number of central and forward W events is listed in Table 5.7.

As a validation of the W selection, the measured cross section for inclusive W production is calculated. The cross section is calculated from the following equation

$$\sigma = \frac{N_{cand}^W - N_{BG}}{A \cdot \epsilon_{ID} \cdot \epsilon_{trig} \cdot \int \mathcal{L}} \tag{5.6}$$

The background in the central (forward) electron sample is calculated to be 3.5% (5.8%). The background was determined for fake electron candidates, $Z \to ee$ events where one electron escaped the detector, and for $W \to \tau\nu$ events where the τ decayed leptonically. The acceptance (A) and particle identification efficiency (ϵ_{ID}) are measured from the detector simulation, while the trigger efficiency (ϵ_{trig}) is measured in the data. The same procedure is used to calculate the $W\gamma$ cross section, and is described in more detail in Chapter 9. The NNLO inclusive prediction comes
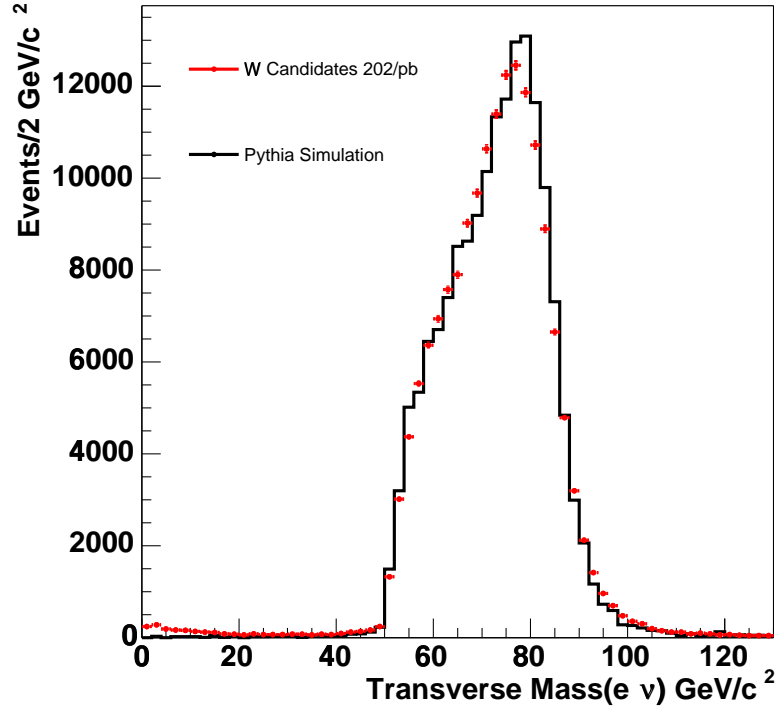
Figure 5.2: The transverse mass, defined in Equation 5.5, for events selected with a high-P_T electron and large missing transverse energy. The distribution is shown in both the data sample and for simulated inclusive W production from the Pythia generator. The transverse mass is required to be within $30< M_T <120$ GeV/c^2 for the $W\gamma$ event selection.

from Stirling, *et. al.* [43]. The measured cross section in the $W\gamma$ base sample is show in Table 5.4. The measured value for the base sample agrees well with both the predicted NNLO cross section and the cross section listed in the soon to be published inclusive W production analysis [44].

5.4.2 Photon Selection

After finding a W candidate event, an isolated, central photon is selected with $E_T^\gamma >$ 7 GeV. Starting with all central EM clusters, the photon is required to have energy

Table 5.4: Inclusive W cross section results in the $W + \gamma$ analysis. The published inclusive W cross sections in the central-electron and central- and intermediate-muon channels are also listed for comparison. The published results are based upon a 72 pb^{-1} sub-sample from the dataset discussed in this analysis.

	σ (nb)	Stat	Syst	Lum
NNLO $\sigma(W)$	2.73			
Cen Elec W	2.70	± 0.01	± 0.07	± 0.18
Plug Elec W	2.57	± 0.01	± 0.10	± 0.18
Pub CMUP W	2.781	± 0.019	± 0.102	± 0.166
Pub CMX W	2.755	± 0.028	± 0.076	± 0.165
Pub CE W	2.753	± 0.015	± 0.084	± 0.165

predominantly from the electromagnetic calorimeter. The shower max profile is required to be consistent with a single particle and must be located in a good fiducial region of the calorimeter. To reject charged particles, no 3D tracks can be matched to the cluster or the track P_T must be significantly less that the E_T of the photon. The photon is required to be isolated from other activity in the calorimeter or tracking volume. The detailed values of the cuts are listed in Table 5.5. After passing all of these requirements, the separation between the W electron and the photon is required to be $\Delta R(l, \gamma) \equiv \sqrt{(\eta_l - \eta_\gamma)^2 + (\phi_l - \phi_\gamma)^2} > 0.7$.

5.5 $W\gamma$ Event Selection Summary

After applying the full event selection for $p\bar{p} \to W\gamma + X \to e\nu\gamma + X$ events, 195 $W\gamma$ candidates are found in the data, with 131 electrons in the central and 64 electrons in the forward region. The final kinematic and topological cuts used to select the events are summarized in Table 5.6, and the sequential effects of the event selection are shown in Table 5.7. Using the 160,000 W candidates, the measured W transverse mass distribution matches well with simulated data (see Figure 5.2).

Central Photon	
E_T	> 7.0 GeV
E_{had}/E_{em} (*)	$< 0.125 || < 0.055 + 0.00045 \times E$
CES $(\chi^2_{wire} + \chi^2_{strip})/2$	< 20
CES $|x|$	< 21.0 cm
CES $|z|$	$9.0 < |z| < 230.0$ cm
2nd CES $<$ sliding	$< 0.14 \cdot E_T, (E_T < 18)$
	$< 2.4 + 0.01 \cdot E_t, (E_T > 18)$
Isolation	$Iso/E_T < 0.1, (E_T < 20)$
	$< 2.0 + 0.02 * (E_T - 20.0)$ GeV, $(E_T > 20)$
Number matched tracks	$N3D \leq 1$ and $P_T < 1 + 0.005 \cdot E_T$
Track Isolation	< 2 GeV

Table 5.5: Cuts used to select photon candidates in the central calorimeter with $|\eta_\gamma| < 1.0$.

Also, the measured cross section agrees with the predicted NNLO inclusive W cross section [43]. A dramatic reduction in the event rate is seen from the selection of an associated photon candidate. Applying an isolation cut to the photon candidate reduces the event sample the largest amount with a rejection factor of almost 100. The candidate events contain both the $W\gamma$ signal and backgrounds. The Standard Model prediction for the $W\gamma$ signal is discussed in Chapter 6, and the backgrounds are described in Chapter 8.

Table 5.6: The kinematic and topological cuts used to select $W\gamma + X$ events.

Electron E_T	> 25 GeV
Electron $|\eta|$	< 2.8
$\not{E}_T$	> 25 GeV
Transverse Mass(e,ν)	$30 < M_T(e, \nu) < 120$ GeV/c^2
Photon E_T	> 7 GeV
Photon $|\eta|$	< 1.1
$\Delta R(e, \gamma)$	> 0.7

Table 5.7: The number of events in the data after applying each of the selection cuts. A total of 195 $W\gamma$ candidates events were found in the full dataset.

Selection	Central Electron	ForwardElectron
Electron	267366	219375
Missing Et	104498	60920
Transverse Mass	102518	60333
Central Photon	169	65
$\Delta R(e,\gamma)$	131	64

Chapter 6

Standard Model Prediction

$W\gamma$ and $Z\gamma$ production, with leptonic decay of the W and Z boson, is completely described and calculable at Leading Order (LO) in the Standard Model. In order to compare these calculations with the selected data events, $W\gamma + X$ and $Z\gamma + X$ event generator programs were used to create simulated event samples. These samples were used to determine the expected $W\gamma$ and $Z\gamma$ signal, and were used to predict background contributions that will be discussed later. While generating the events, there are divergences and singularities that must be avoided in order to have consistent and stable predictions. The kinematic limits and the impact of these limits on the simulated samples were measured in detail as discussed below. As well, a correction must be applied to the LO calculation to compensate for Next-to-Leading Order (NLO) terms not included in the LO event generation. The final samples of $W\gamma + X$ and $Z\gamma + X$ events are processed with a full detector simulation and offline reconstruction to determine the expected signal rate.

6.1   Leading Order Generators WGAMMA and ZGAMMA

The LO WGAMMA and ZGAMMA Monte Carlo matrix element generators written by Baur and Berger [11] were used to produce $p\bar{p} \rightarrow W\gamma X \rightarrow l\nu\gamma + X$ and $p\bar{p} \rightarrow$

$Z\gamma X \to l^+l^-\gamma + X$ samples. Here X is any additional particles in the final-state of the event attributed to the remnants of the proton and antiproton and initial state gluon radiation. The calculation is done at tree-level using electroweak helicity amplitudes for $V\gamma$ production and radiative boson decays. The calculation includes the interference from all terms shown in Figure 2.1. The kinematic phase space of the production is divided into an adaptive grid using the VEGAS integration program [37]. The initial parton momentum distributions are determined using the CTEQ5L [40] LO parton distribution function (PDF). Since WGAMMA and ZGAMMA are LO generators, the calculation has no QCD initial state radiation, and the $W\gamma$ or $Z\gamma$ system has no transverse momentum. To correct this, the matrix element generators have been interfaced to PYTHIA (version 6.203) which models the effect of initial state gluon radiation and hadronization, along with a tuned underlying event.

When generating events in the $V + \gamma$ processes, the phase space region must be appropriately limited to ensure accruacy. Loose kinematic and geometrical limits well away from the kinematic selection criteria are used to avoid biasing the event sample. Additionally, two regions of phase space must be removed from the calculation. The cross section grows extremely fast as the photon energy approaches zero due to the infrared divergence. In addition, the region of small opening angle between the lepton and photon, $\Delta R_{l\gamma} \simeq 0$, is divergent because of collinear photon emmision. Therefore when generating events, the following two cuts are applied to the phase space considered, $E_T^\gamma > 5$ GeV and $\Delta R_{l\gamma} > 0.2$.

Using these cuts, samples of approximately 200,000 events each were generated for the $W\gamma$ process in all three W leptonic decay modes, and the $Z\gamma$ channel for the Z electron decay. The LO cross section calculated from the WGAMMA and ZGAMMA

generators are listed in Table 6.1. The Standard Model parameters used to generate the samples are specified in Table 6.2.

Table 6.1: Cross sections for final $W^{\pm}\gamma$ and $Z\gamma$ processes at $\sqrt{s} = 1.96$ TeV calculated at Leading Order.

Process	E_t^{γ}	$\Delta R(l, \gamma)$	$\sigma\,(pb)$
$W^{\pm}\gamma \rightarrow e\nu\gamma$	5.0	0.2	32.4
$W^{\pm}\gamma \rightarrow e\nu\gamma$	7.0	0.7	14.0
$W^{\pm}\gamma \rightarrow \mu\nu\gamma$	5.0	0.2	32.2
$W^{\pm}\gamma \rightarrow \mu\nu\gamma$	7.0	0.7	13.9
$W^{\pm}\gamma \rightarrow \tau\nu\gamma$	5.0	0.2	28.3
$Z\gamma \rightarrow ee\gamma$	5.0	0.2	8.6

Table 6.2: The standard model parameters used in the comparison of the Monte Carlo generators. For the electroweak parameters, inputs are shown in bold fonts, while the other EW parameters are derived.

Beam type	$p\bar{p}$
$\sqrt{s}$ [TeV]	1.96
PDF	CTEQ5L
Q_f^2	parton collision $\hat{s}$
$\alpha_s(M_Z)$	**0.127**
$M(W)$ [GeV]	**80.41**
$M(Z)$ [GeV]	**91.188**
G_F[GeV^{-2}]	**1.6639 $\times$ 10^{-5}**
$\sin^2\theta_W$	0.22242
α_{em}	**1/132.43**
Γ_W[GeV]	2.103
Γ_Z[GeV]	2.514
$M(top)$ [GeV]	**175**

When generating samples, the `WGAMMA` and `ZGAMMA` programs produce weighted events. The event weight is equivalent to the probability that an event with those kinematic quantities will occur. In order to process the events with the detector

simualtion, the events are converted to unit weight. To accomplish this, the maximum event weight is recorded when generating a sample of events. The event weights are normalized to the maximum event weight, w_{max}, and reprocessed using a standard hit-or-miss strategy for unweighting. An event is stored if its weight, w, satisfies:

$$w/w_{max} > \mathcal{R}[0; 1] \tag{6.1}$$

where $\mathcal{R}[0;1]$ donates a random number uniformly distributed between 0 and 1.

The `WGAMMA` program includes mechanisms for introducing non-Standard Model coupling terms, $\Delta\kappa_\gamma$ and λ_γ. Samples with non-zero anomalous couplings were generated for comparison with the data, and for placing limits on the anomalous couplings in the $WW\gamma$ vertex. These samples are generated at value of $\Delta\kappa_\gamma$ and λ_γ equal to -2, -1, 0, 1, and 2 in a 5×5 grid. These samples will be used in the future to produce limits on the anomalous couplings of $W\gamma$ production.

6.1.1 Detector Simulation

After generating unweighted events, the $W\gamma + X$ and $Z\gamma + X$ event samples were processed with a GEANT-based [41] detector simulation. The GEANT program uses a Monte Carlo-based simulation of the interaction between produced particles and detector material. To achieve this, the entire detector is defined within the GEANT framework. Each of the individual sub-detectors are modeled to include exact details such as the geometric design, data acquisition cables, and individual wires within the tracking volume. For each particle within the simulated data, the four momentum is used to describe its path as it traverses the detector simulation. The effect of multiple scattering, bremsstrahlung, and shower development are modeled, and the subsequent generation of secondary particles simulated. Once

the process has been performed for all final-state particles in the event, the simulation outputs data banks that mirror the output from the detector DAQ. These data banks are then processed with the identical offline reconstruction program used for collider data. The result of the simulation is the expected detector response to the events produced from the LO generator. These events, weighted by the E_T^γ dependent k-factor discussed below in Section 6.2, are used to determine the acceptance correction to the measured $W\gamma \to e\nu\gamma$ candidates. The details of this calculation and the necessary correction are presented in Chapter 7.

6.1.2 Uncertainties in the Standard Model Prediction

The choice of input parameters to the generator was optimized to simulate events at the Tevatron, and the error on the LO prediction from these parameter choices determined. Several of the parameters listed in Table 6.2 are Tevatron parameters and are considered exact numbers (e.g. $\sqrt{s}$). While choices such as PDF, factorization scale, and α_s were chosen based upon discussions with the program authors [46]. Determining the variation in the LO prediction from tuning these input parameters gives the error on the Standard Model prediction.

The largest variation in the LO prediction comes from changing the parton distribution function. The initial choice of CTEQ5L was changed to an alternate parameterization, MRST-72 [43]. The geometric and kinematic acceptance calculated from either the CTEQ5L or MRST-72 sample is found to match within statistical errors (difference $< 0.5\%$). The overall predicted production rate for the $W^\pm\gamma$ processes was 5% higher for the CTEQ5L sample. The calculated LO cross section for CTEQ5L (MRST-72) is 32.4 (30.8) pb. This variation is taken as an error on the absolute normalization of the predicted Standard Model $W\gamma$ production cross

section.

The factorization scale determines the lower limit with which the LO calculation probes the strong interactions generating the initial parton distributions and parton hadronization. The factorization scale, q is set to the incoming quark momentum transfer, $\sqrt{\hat{s}}$, in both WGAMMA and Pythia. Again, negligible variation in the acceptance was found when scaling the factorization scale by several values from $1/2\sqrt{\hat{s}}$, $2/3\sqrt{\hat{s}}$, $3/2\sqrt{\hat{s}}$, to $2\sqrt{\hat{s}}$. The calculated cross section increased with a lower factorization scale lower, and decreased with a higher limit. The maximum variation was 2%, and this is taken as the uncertainty on the calculated LO cross section due to the factorization scale.

Having explored the error on the WGAMMA and ZGAMMA predictions associated with tuning the input parameters, the only significant variation comes from the choice of parton distribution function and the factorization scale. These input have no effect upon the kinematic distribution and consequently, no effect on the acceptance. The error on the calculated LO Standard Model cross section for the $W\gamma$ signal is calculated as the sum in quadrature of the PDF error and factorization error. The measured error on the LO cross section is 5.5%.

6.2 $\mathcal{O}(\alpha_s)$ Corrections

Since the WGAMMA and ZGAMMA programs contain only LO terms, the predictions are corrected for additional matrix element terms that include initial state emission of a gluon or quark and gluon loops. Three of the possible matrix element terms are represented by the Feynman graphs shown in Figure 6.1. To measure this correction, the Next-to-Leading Order (NLO) $W\gamma$ and $Z\gamma$ programs [38, 39] are used to make cross section calculations. From the ratio of the differential cross section, $\delta\sigma/\delta E_T^\gamma$, at

NLO and LO, a photon-E_T dependent k-factor is determined. The NLO programs have a limitation in that they do not calculate the final-state lepton radiation , or inner bremsstrahlung, contribution. This is due to technical issues within the theory that are current topics of investigation by several groups (see [47]). A correction for this effect is discussed in the next paragraph. Also, the NLO $W\gamma$ and $Z\gamma$ programs take into account only first-order terms from QCD emission and no second-order electroweak terms. Since for large lepton-photon separation ($\Delta R(l,\gamma)$ >0.2) the QCD correction dominates in proton antiproton processes, it was determined that this was the only correction that we needed to apply to the LO program results.
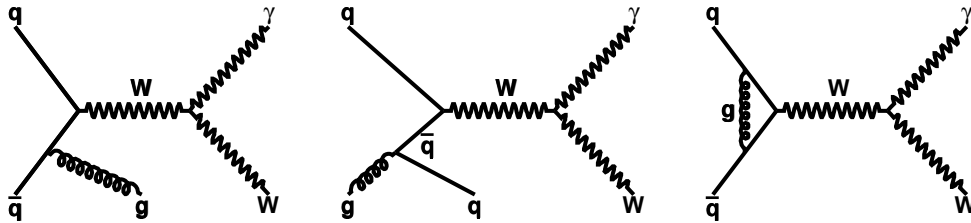
Figure 6.1: Feynman diagrams depicting some of the Next-to-Leading Order terms for $W\gamma + X$ production. The diagrams show the initial state gluon radiation (left), gluon splitting to a quark-anti-quark pair (center), and gluon loop (right) corrections to s-channel $W\gamma$ production. Similar graphs for the u- and t-channel production are included in the NLO calculation.

Because the NLO programs contain only the u-, t-, and s-channels, while the LO programs contain all terms, two NLO corrections are applied based upon the kinematics of the considered LO event. For the $u-$, $t-$, and $s-$channels events, the k-factor measured from the NLO $W\gamma$ program is applied. While the inner bremsstrahlung term is corrected using the inclusive W or Z NLO correction of 1.36 [43]. While an absolute separation is impossible from quantum-mechanical arguments, it is possible to enhance certain terms by considering the di-lepton invariant mass of the decay leptons. Figure 6.2 shows the invariant mass distribution

for the generated $W\gamma$ and $Z\gamma$ events. The dip in the distribution just below the central mass value is created by the minimum photon E_T and ΔR cuts. To separate the sample into $u-$, $t-$, and $s-$channel events and inner-bremsstrahlung events, an invariant-mass cut was chosen at 76 GeV/c^2 for $W\gamma$ events, and 86 GeV/c^2 for $Z\gamma$ events. These values are chosen for two reasons: they are at the minimum of the distributions, and these values are twice the decay width below the mass value of the W or Z [4]. When a generated event is reconstructed, it is weighted with either the inclusive NLO correction of 1.36 or the E_T^γ-dependent k-factor discussed next.
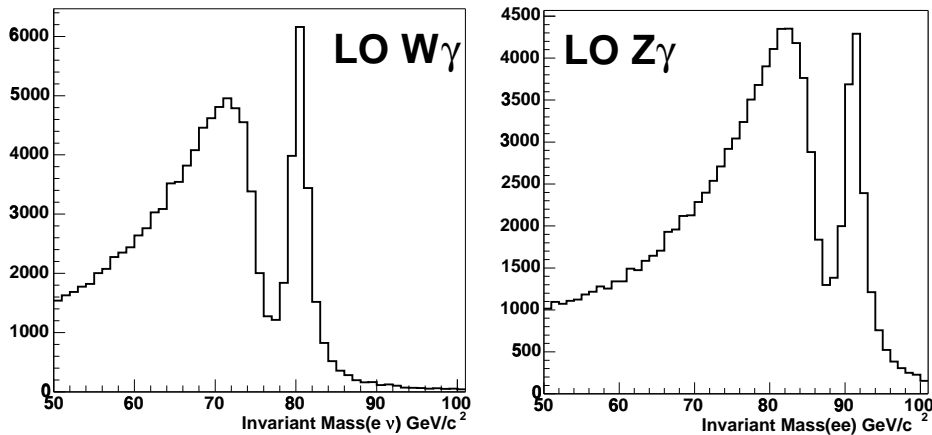
Figure 6.2: Invariant-mass of the unweighted events in $W\gamma$ (left) and $Z\gamma$ samples generated for the analysis. The distribution shows the separation between the u, t, and s channels from the inner bremsstrahlung caused by the E_T^γ and ΔR cuts during event generation.

By taking the ratio of the NLO cross section to the LO cross section, a k-factor correction as a function of photon E_T is measured. The NLO programs calculate a binned cross section for the $W\gamma$ and $Z\gamma$ processes at both LO and NLO level. Since the LO samples are generated with LO PDFs, it is necessary to make sure that the LO cross section uses the LO PDF CTEQ5L. The NLO cross section is determined

using the NLO PDF CTEQ5M. The ratio of the cross sections for $W\gamma$ and $Z\gamma$ and shown in Figure 6.3. The ratios have been fitted with the resulting functions

$$k(W\gamma, E_T^\gamma) = 1.62 + 0.0001E_T^\gamma - 0.386exp(-0.100E_T^\gamma) \tag{6.2}$$

$$k(Z\gamma, E_T^\gamma) = 1.46 + 0.00073E_T^\gamma - 0.125exp(-0.062E_T^\gamma) \tag{6.3}$$

where E_T^γ is in GeV. These k-factors were applied to LO events that had lepton invariant masses above the previously discussed cuts. Integrating the k-factor over all of the generated events, the effective NLO cross section corrections are 1.39 for $W\gamma$ and 1.37 for $Z\gamma$. The NLO corrected cross section for $W\gamma$ production with photon E_T above 7 GeV and $\Delta R(l, \gamma)$ above 0.7 is 19.3 ± 1.3 pb. The estimated error on this value is discussed in the next section.
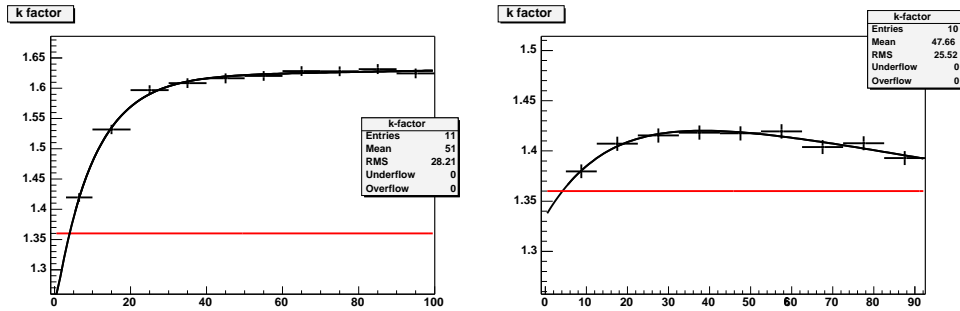
Figure 6.3: k-factor versus E_t^γ for $W\gamma$ (left) and $Z\gamma$ (right) production for the s-, t- and u-channel processes. The red line indicates the value for inclusive W production of 1.36.

6.2.1 $\mathcal{O}(\alpha_s)$ Correction Systematic Errors

The sources of systematic errors on the NLO correction are the statistical variations, acceptance, and choice of factorization and hadronization scale. The maximal vari-

ation from statistical variations in the calculation is found to be $\approx$1%. Therefore 1% is used as a conservative error. Because the QCD correction involves the emission of an additional jet or gluon, the dynamics of the event are different in the NLO and LO calculations and the acceptance may vary.

To study the effect, the acceptance for the analysis cuts at parton level is measured for the NLO and LO calculations. The NLO program cannot be unweighted using the traditional hit-or-miss method, so the acceptance is measured as a ratio of the cross sections. The cross section is calculated for the loose sample cuts described in Section 6.1 and the analysis cuts. Comparing the two calculations, the acceptance for the NLO program is found to be 1.0% higher. This variation is the error on the acceptance from the NLO correction.

Finally, the choice of factorization scale has a considerable effect on the resulting NLO correction. In order to be consistent with the LO generation and the inclusive NLO correction, the factoriation scale was set to $\hat{s}$. From the original paper by Baur and Ohnemus [38], the NLO correction error is measured from Figure 6 by changing the factorization scale up and down by a factor of 2. This variation placed an error on the NLO correction of 3%. Adding these errors in quadrature, the total error on the Standard Model prediction from the NLO correction is 4%, with a 1.0% error on the acceptance.

6.3 Summary of $W\gamma$ and $Z\gamma$ Cross Sections

The Standard Model cross sections for $\bar{p}p \rightarrow W\gamma + X \rightarrow e\nu\gamma + X$ and $\bar{p}p \rightarrow Z\gamma + X \rightarrow ee\gamma + X$ were calculating using the correction to the Leading Order cross section discussed above. The calculated cross sections are listed with the calculated 7% error in Table 6.3. The measured cross section of $W\gamma$ production for

$(E_T^\gamma > 7$ GeV$,\Delta R(e,\gamma) > 0.7)$ will be compared to this Standard Model prediction

in Chapter 9.

Table 6.3: Cross sections for $W\gamma$ and $Z\gamma$ processes predicted by the Standard Model calculation including $\mathcal{O}(\alpha_s)$ contributions.

Process	E_t^γ	$\Delta R(l,\gamma)$	$\sigma(pb)$
$W\gamma \to e\nu\gamma$	5.0	0.2	44.4 $\pm$ 3.1
$W\gamma \to e\nu\gamma$	7.0	0.7	19.3 $\pm$ 1.4
$W\gamma \to \mu\nu\gamma$	5.0	0.2	44.1 $\pm$ 3.1
$W\gamma \to \mu\nu\gamma$	7.0	0.7	19.3 $\pm$ 1.4
$W\gamma \to \tau\nu\gamma$	5.0	0.2	38.8 $\pm$ 2.7
$Z\gamma \to ee\gamma$	5.0	0.2	11.8 $\pm$ 0.8

Chapter 7

Signal Efficiency and Acceptance

The probability for $W\gamma$ signal events to pass the event selection cuts must be measured to accurately predict the expected number of events. The number of predicted events is then the cross section times the integrated luminosity scaled by this probability. The probability to pass the event selection is broken into two terms: the acceptance (A) and the efficiency (ϵ). The equation for the number of predicted signal events is then

$$N_{pred}^{W\gamma} = A \cdot \epsilon_{sim} \cdot \int \mathcal{L} \cdot \sigma_{gen}^{W\gamma} \qquad (7.1)$$

The acceptance is the percentage of generated events from a signal sample that pass the geometric and kinematic cuts. The efficiency comes from two terms: the probability that a final state electron or photon will pass the particle identification selection, and the probability that the event will be selected by the online trigger, $\epsilon = \epsilon_{trigger} \times \epsilon_{ID}$. The efficiency of the online trigger to select $W\gamma$ events is measured with the data. The identification efficiency is measured in simulated data and corrected for variations between data and the detector simulation. The number of events is then scaled by the product of the acceptance, the trigger efficiency, and the corrected ID efficiencies. A summary of these factors is shown in Table

7.1. Additionally, a correction to the integrated luminosity is required since the CLC detector is sensitive to interactions outside of the active detector volume. This chapter describes the determination of A, $\epsilon_{trigger}$, ϵ_{ID}, while the results of the calculation of the expected event rate is presented in Chapter 9.

Table 7.1: Summary of the acceptance, trigger efficiency, and particle identification efficiency for the $W\gamma \to e\nu\gamma$ signal sample. The particle identification efficiency is measured in simulation and is later tuned to match the efficiency in data samples.

	Central Electron	Forward Electron
A	0.0487±0.0003	0.0297± 0.0003
ϵ_{sim}	0.238±0.01	0.232±0.01
$\epsilon_{trigger}$	0.961±0.01	0.973±0.008

7.1 Acceptance

The acceptance, A, is simply defined as the fraction of the $W\gamma$ events generated that meet the geometric and kinematic requirements of the analysis. The kinematic cuts are listed in Table 5.6. Using the Leading Order $W\gamma$ generator described in Chapter 6, a signal sample with kinematic limits $E_T^\gamma > 5$ GeV and $\Delta R(e, \nu) > 0.2$ was created. The signal acceptance for the analysis cuts of $E_T^\gamma > 7$ GeV and $\Delta R(e, \nu) > 0.7$ is calculated as the ratio

$$A = \frac{N_{passed}}{N_{generated}} \qquad (7.2)$$

The acceptance is determined separately for the central and forward region, where the central electron η range is $|\eta_e| < 1.0$ and the forward electron η range contains $1.2 < |\eta_e| < 2.8$. The central $W\gamma \to e\nu\gamma$ acceptance is 0.0487 ± 0.0005, and

the forward $W\gamma \to e\nu\gamma$ acceptance is 0.0297 ± 0.0003. The acceptance after each kinematic cut is shown in Table 7.2. The calculation of the error on the acceptance is discussed in Chapter 6.

Table 7.2: The acceptance, A, of the Standard Model $W\gamma \to e\nu\gamma$ signal for the kinematic cuts in Table 5.6. Also listed is the acceptance for inclusive $p\bar{p} \to W + X \to e\nu + X$ events.

Cut	$W\gamma \to e\nu\gamma$ Central $|\eta_e| < 1.0$	$W\gamma \to e\nu\gamma$ Forward $1.2 < |\eta_e| < 2.8$	Incl W Central $|\eta_e| < 1.0$
η_e	0.496	0.352	0.508
$E_T^e > 25$ GeV	0.146	0.1774	0.267
$\not{E}_T > 25$ GeV	0.133	0.1618	0.249
$30 < M_T(e,\nu) < 120 \text{GeV}/c^2$	0.131	0.158	0.245
$|\eta_\gamma| < 1.1$	0.072	0.062	-
$E_T^\gamma > 7$ GeV	0.051	0.031	-
$\Delta R(e,\nu) > 0.7$	0.0487	0.0297	-

7.2 Trigger Efficiency

The trigger efficiency is the probability that a $W\gamma \to e\nu\gamma$ signal event meeting the kinematic cuts will be accepted by the trigger. The efficiency for an event to pass the trigger requrement is measured in samples containing the trigger object but not biased by the analysis trigger requirements. Using trigger paths parallel to the analysis path, the trigger response is determined offline from high purity objects. The measured efficiency is then applied to the simulated signal sample to correct the predicted number of events. The efficiency of each trigger is measured separately for the L1, L2, and L3 efficiencies and then the product of these is taken as the overall efficiency. The central electron trigger efficiency is found to be $96.1 \pm$

1.0%. The forward W trigger efficiency is dependent upon the electron P_T and the $\not{E}_T$, with an integrated efficiency of $97.3 \pm 0.8\%$. The details of each measurement are discussed in Appendix B.

7.3 Particle ID Efficiency

The efficiency of the $W\gamma \rightarrow e\nu\gamma$ signal events to pass the particle identification selection is measured in the detector simulation. The particle identification selects an electron and a photon in each event, and the efficiency for each is measured separately and combined as a product. The total ID efficiency measured in the simulation (ϵ_{sim}) is 0.238 ± 0.005 for central events, and 0.232 ± 0.008 for forward events. These particle ID efficiencies have been tuned to match the detector response in data. A detailed discussion of the tune measurement is presented in the next section.

7.4 Detector Simulation Tuning

Traditionally, the particle ID efficiency (ϵ_{ID}) is determined exclusively in the data using a highly pure sample of final state particles. For high-E_T leptons, such highly pure samples are readily available from the decays of the Z boson. Pure samples of final state photons, though, are difficult to obtain, because true photons are hard to distinguish from background. For the current analysis selection, the low E_T^γ cut of 7 GeV makes a direct efficiency calculation from the data impossible. Therefore, the detector simulation is used to measure the efficiency of both electrons and photons, and then tuned to match the response in data samples. The equation for the applied

efficiency is then

$$\epsilon_{ID} = \epsilon_{sim} \times Corr \tag{7.3}$$

where $Corr$ is the correction determined from variations between data and simulation. The calculation of this tuning for central electrons, forward electrons, and central photons is described below.

7.5 Electron ID Efficiency

The efficiency for an electron to pass the particle identification cuts is measured in a sample of simulated $Z \to ee$ events [53, 54] generated using Pythia [24]. A data sample collected using the central electron trigger is compared to the simulation. These data and simulation samples provide a highly-pure source of electrons, and they are used to evaluate detector response for both central and forward electrons. A central electron is selected with the criteria in Table 5.2, and another electron, either central or forward, is selected with loose requirements. The loose selection is shown in Table 7.3. The invariant mass of the two electrons is calculated and required to be consistent with the mass of the Z, $75 < M_{ee} < 105$ GeV. From these highly pure high-P_T electrons, the electron identification efficiency is calculated. A correction for QCD background contamination is subtracted using a same-sign di-electron sample [53].

For events with the loose electron in the central calorimeter, the efficiency is calculated using:

$$\epsilon_c^i = \frac{N_{Ti} + N_{TT}}{N_{CC} + N_{TT}} \tag{7.4}$$

where N_{TT} is the number of events where both legs pass the tight central cuts, N_{CC} is the number of central-central Z candidates, and N_{Ti} is the number of events

Table 7.3: Loose electron selection used to calculate the electron ID efficiency in the the central and forward detector.

Variable	Central	Forward
E_T	20 GeV	20 GeV
$|\eta|$	<1.0	$1.2 < |\eta| < 2.8$
Had/Em	<0.125	<0.125
Track P_T	> 10 GeV/c	no cut
Fiducial	CEM	PEM
charge	opposite	no cut

where one leg passes tight selection cuts and the second leg passes the ith central electron ID cut. For forward electrons, the electron ID efficiency is calculated using:

$$\epsilon_f^i = \frac{N_i}{N_{CF}} \tag{7.5}$$

where N_i is the number of events passing the ith forward electron ID cut, and N_{CF} is the total number of central-forward Z events.

The efficiency was measured for both the data and generated, and a correction factor for the simulated data is calculated as the ratio of the two efficiencies. The results for the central electron ID efficiency are shown in Table 7.4. The ratio of the two central efficiencies (data/simulation) is $Corr_{ID}^c = 0.964 \pm 0.01$, and this was applied as a correction to the simulated electron efficiency for central electron events. The results for the forward electron ID efficiency are shown in Table 7.5. The correction applied to the forward electron selection is $Corr_{ID}^f = 0.942 \pm 0.025$.

7.5.1 Electron Tracking Efficiency

Separate from the electron indentification selection, the tracking reconstruction efficiency is compared between the data and detector simulation. For the central

Table 7.4: Efficiency of the central electron identification cuts, as percentages, measured using the $Z \rightarrow ee$ events in the data and Pythia Monte Carlo. The errors shown are statistical errors and result in an error of ± 0.01 on the Monte Carlo correction factor of 0.964.

Variable	Data (%)	Detector Simulation (%)
Had/Em	99.3	98.9
E/P	91.2	93.1
$Isolation/E_T$	97.6	98.0
L_{shr}	98.9	97.2
$Q * \Delta X$	98.2	98.7
$|\Delta Z|$	99.4	99.6
χ^2_{strip}	96.2	98.3
N^{track}_{Ax}	99.6	99.8
N^{track}_{St}	97.4	99.4
Total ε	82.5 $\pm$0.5	85.6 $\pm$0.2

Table 7.5: Efficiency of the forward electron identification cuts, as percentages, measured in the $Z \rightarrow ee$ events in the data and Pythia Monte Carlo. The errors shown are statistical errors and result in an error of ± 0.02 on the Monte Carlo correction factor of 0.941.

Variable	Data (%)	Detector Simulation (%)
PEM3x3 χ^2	91.2	98.6
$Isolation/E_T$	98.6	98.2
Had/Em	98.9	98.7
PES 5×9 u	99.3	99.6
PES 5×9 v	99.2	99.7
Total ε	85.9 $\pm$0.9	91.2 $\pm$0.2

electron tracking, the COT tracking reconstruction is measured using a W no-track sample. The efficiency that a high-P_T track is reconstructed for a central electron with $E_T > 25$ GeV is found to be $100 \pm 0.4\%$ in both the data and the simulation. Therefore, no correction is needed.

A correction for the Phoenix tracking efficiency in simulation is calculated in the previously discussed $Z \rightarrow ee$ samples. After first requiring a tight central electron and a tight forward electron with no track requirement, the forward tracking efficiency is calculated as the ratio of forward electrons with and without a matched Phoenix track. The efficiency as a function of electron η is shown in Figure 7.1. The efficiency in the simulation is slightly higher; a correction factor between data and simulation is calculated to be $Corr_{trk}^{Phoenix} = 0.986 \pm 0.015$.
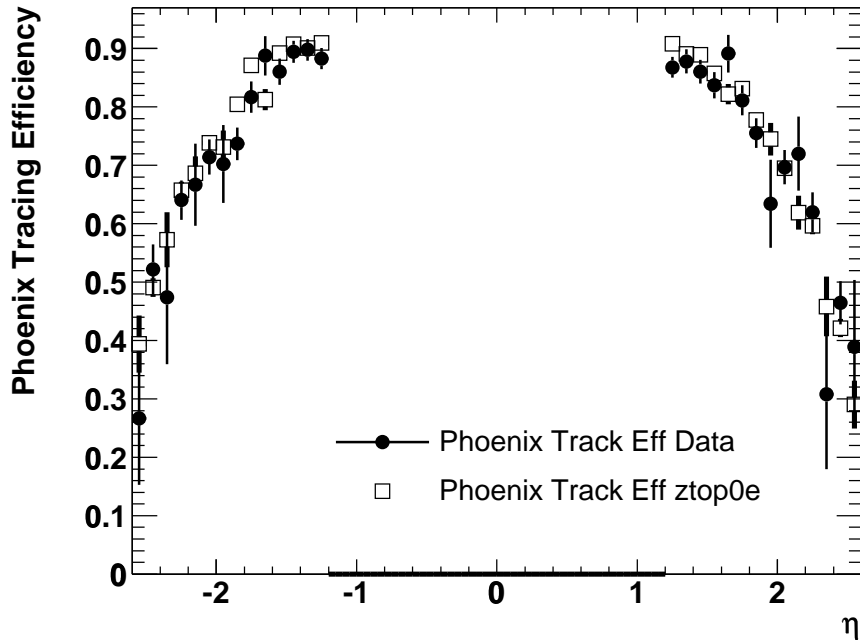
Figure 7.1: Phoenix tracking efficiency measured in $Z \rightarrow ee$ data and Monte Carlo samples as a function of η. The ratio of efficiency in the simulation to the data is 98.6%, and is applied to the $W\gamma$ simulation.

For the forward electron analysis, the Phoenix track requirement implies that a z-vertex was found in the event. The efficiency of the z-vertex reconstruction is calculated in data and simulated $Z \to ee$ samples. The track from the central electron is removed from the algorithm, and a reconstructed vertex matched to the forward decay electron is required. The resulting efficiency for reconstructing the event vertex is $\epsilon_{vtx}^{data} = 93.1 \pm 0.3$ for any vertex. In the detector simulation, the measured efficiency is $\epsilon_{vtx}^{sim} = 96.5 \pm 0.1\%$ for any vertex. Thus, a correction factor for the simulation efficiency is

$$Corr_{vtx} = \epsilon_{vtx}^{data}/\epsilon_{vtx}^{sim} = 0.965 \pm 0.005 \qquad (7.6)$$

The equations for the corrected electron ID efficiency in the central and forward detector are shown below. The central ID efficiency is corrected only for variation in the cut efficiency between data and simulation. In the forward detector, the two correction factors for the Phoenix tracking and the vertex reconstruction efficiency are combined with the forward electron ID efficiency correction.

$$\epsilon_{ID}^c = \epsilon_{sim}^c \cdot Corr^c \qquad (7.7)$$

$$\epsilon_{ID}^f = \epsilon_{sim}^f \cdot Corr^f \qquad (7.8)$$

Where the correction factor, $Corr^c$, in the central electron simulation is 0.964 ± 0.01, and the forward electron correction is 0.896 ± 0.03 and calculated from

$$Corr^f = Corr_{ID}^f \cdot Corr_{trk}^{Phoenix} \cdot Corr_{vtx} \qquad (7.9)$$

7.6 Photon Efficiency

The efficiency of the photon identification selection cuts is measured using electron and other data samples, since selecting a pure sample of photons with $E_T^\gamma > 7$ GeV is not feasible. The photon identification cuts are divided into two groups: isolation and shower quality cuts. The efficiency of the isolation cuts is measured using random cones within inclusive W and minimum bias datasets. (Here, minimum bias response to a minimum amount of activity in the CLC detector described in Chapter 4.) An E_T^γ dependent correction is applied to the simulated data. The efficiency of the shower shape cuts is measured using highly pure electron samples, since the calorimeter response should be mirrored between photons and electrons. Again, a correction for the simulated detector response is determined and applied to the Standard Model event predictions.

$$Corr^\gamma = Corr_{Iso}^\gamma \cdot Corr_{shower}^\gamma \tag{7.10}$$

7.6.1 Photon Isolation Efficiency

The photon isolation cuts assure that the measured properties of the photon candidate have not been biased by underlying activity in the event. To study this underlying activity, random cones of radius 0.4 ($R = \sqrt{\eta^2 + \phi^2}$) are selected in data events, and the isolation cuts are applied to the cone. The efficiency of this cone to pass the isolation cuts is measured and compared with the detector simulation. The ratio of the two efficiencies is applied to simulated data. The study is performed in several data samples to assure consistency.

Random Cone Strategy

Events are selected with either a W candidate, a jet, or a minimum bias event. Once an event is selected, the trigger object determines the location of the test cone. For a W candidate event, the ϕ of the cone is set to $\phi_e + 90^o$ and the η set to a random value [-1.1,1.1]. A schematic of the random cone selection is shown in Figure 7.2. The same determination is done in the jet sample, except that the ϕ of the leading jet is used. Because there is no trigger object in a minimum bias event, both a random η and ϕ are chosen. Since the cone itself has no E_T, an arbitrary E_T is assigned to the cone in order to apply cuts that are ratios or sliding. The E_T values are 7, 10, 15, 20, 25, 30, 35, 40, 45, and 50 GeV. The cuts are then applied in the order listed in Table 5.5 and the efficiency defined as the simple ratio:
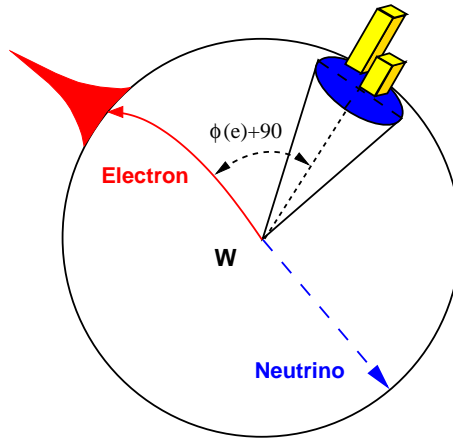
Figure 7.2: A schematic showing the selection of a random cone for studying the efficiency of photon isolation cuts. A cone of radius 0.4 is selected 90° in ϕ from the electron in inclusive W events.

$$\epsilon = \frac{Num_{Cones}^{Passed}}{Num_{Cones}^{Total}} \qquad (7.11)$$

As the fiducial cuts are solely geometric, they are assumed to have an efficiency of 100%. No requirement is applied such that the cone cannot point at a reconstructed object. Thus, the effect of a jet "clobbering" a photon is measured along with the effect of underlying event.

The isolation cut has two corrections that are applied based upon the topology of the event. The largest and most important correction is due to additional underlying event energy from multiple interactions. This correction is a linear function dependent on the number of reconstructed vertices in the event. The multiple interaction correction is then subtracted from the cone of 0.4 surrounding the photon. To determine the slope of the correction, the total energy in the cone versus the number of vertices is fitted. Figure 7.3 shows the data for W, Jet20, and minbias events, and Equation 7.12 gives the final fit for the multiple interaction correction in W events.

$$V_{Corr} = 0.28 \pm 0.01 \text{GeV} \cdot (N_{vertices} - 1) \qquad (7.12)$$

Applying the same technique to jet20 data gave an equivalent fit within errors, while the fit to the slope in the minimum bias data was lower by 0.03 GeV. This is expected because the minimum bias data is not luminosity weighted, while the W data is biased towards higher luminosity. The correction shown above is applied in all subsequent analysis of photon candidates. With this correction applied, we measure the efficiency of the photon cuts in data and simulation.
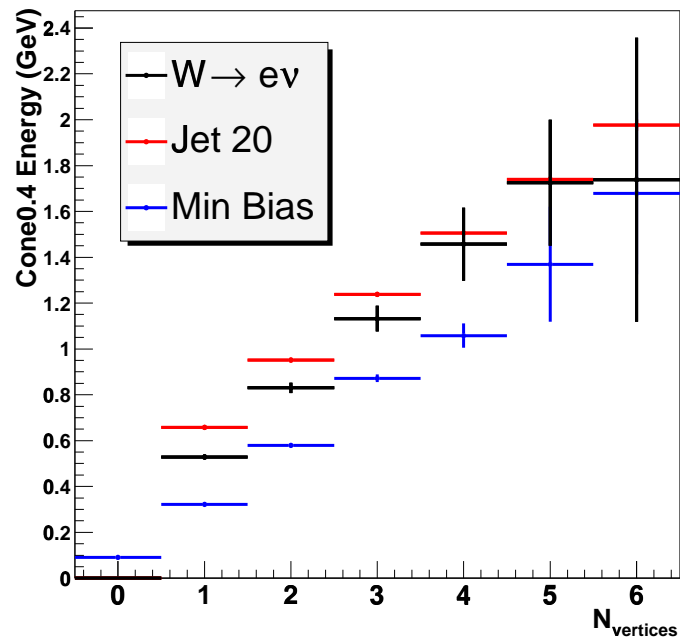
Figure 7.3: Isolation energy in a cone of 0.4 (Iso) versus the number of vertices in the event for $W \to e\nu$, Jet20, and Minbias events.

Calorimeter Isolation Efficiency

The efficiencies of the calorimeter isolation in data and simulation are plotted in Figure 7.4. The ratio of the two efficiencies is plotted in Figure 7.5 and is fitted with a third-order polynomial to give the correction to the simulated efficiency as a function of photon E_T. The results of the fit are given in Eq 7.13, where the E_T is in GeV. The events in the simulated $W\gamma$ signal are reweighted based upon the photon E_T in the event.

$$Corr_{Iso} = 0.884 + 0.0178E_T^{\gamma} - 0.00102E_T^{\gamma 2} + 0.00002E_T^{\gamma 3} \qquad (7.13)$$
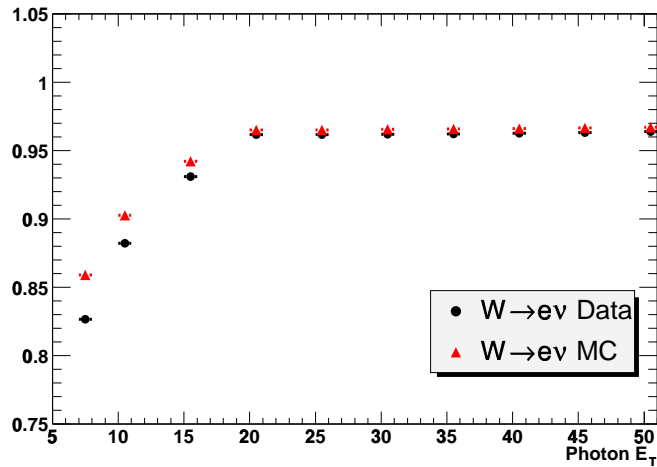
Figure 7.4: The isolation efficiency is plotted versus the assumed photon energy in $W \to e\nu$ data and simulated events. The data is for any number of vertices, while the simulation has only one vertex.
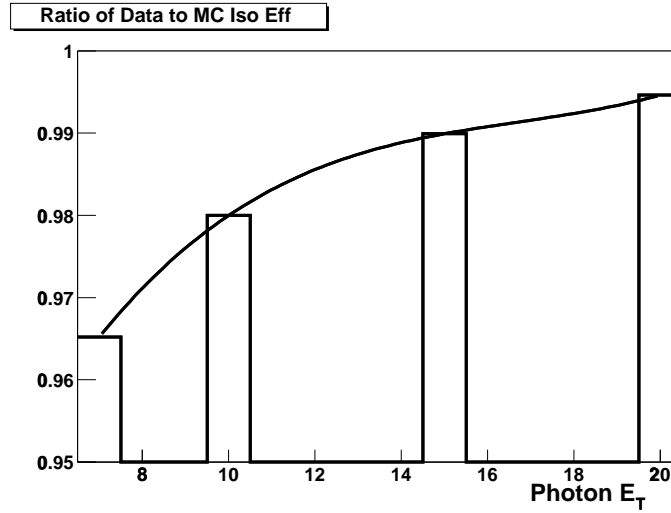
Figure 7.5: The ratio of the calorimeter isolation efficiency in W data events to the efficiency of events in the simulation. The ratio is fit with a third order polynomial up to 20 GeV, above which the ratio is 99.4%.

N3D Efficiency

After applying the calorimeter isolation cut to the random cone, the number of 3D tracks pointing at the cone was counted. For a track to be counted, it was required to point at either the central tower, or one of the two shoulder towers in the center of the cone. (These three towers normally make up the EM Cluster that is considered as a photon candidate.) Also, the z_0 of the track must be within 5 cm of the event vertex. If only one track is matched to the "cluster" towers, then a P_T cut is applied. The efficiency of the cut was found to be very high, and matched between data and simulation within errors. Fig 7.6 shows the efficiency for both samples. The high efficiency is due to the strong correlation between calorimeter isolation and the number of final state particles traversing that area of the detector. Therefore, no correction for the N3D cut is made to the efficiency in the simulation.
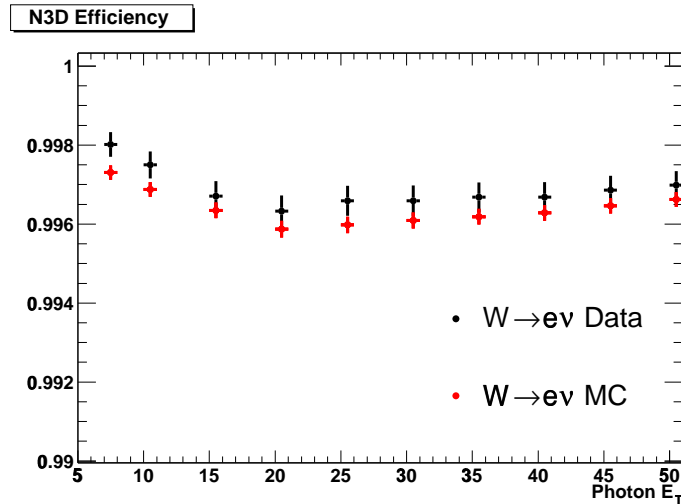
Figure 7.6: The efficiency of the N3D cut for data and MC versus photon E_T. This plot shows the full cut including the sliding cut on P_T if N3D is 1.

Track Isolation Efficiency

The final cut studied using the random cone strategy is the total sum P_T of tracks inside the cone of 0.4. As mentioned previously, for a track to be added to the sum P_T, the z_0 of the track must be within 5 cm of the event vertex. The sum all of the tracks within the cone of 0.4 is then calculated with no cut on the minimum track P_T. The cut is found to be very efficient and the measured values in data and simulation match within errors, and no correction is needed.

Summary of Isolation Efficiencies

After measuring the isolation cut efficiency in the data and simulation, it was determined that only the calorimeter isolation required a correction in the detector simulation. Table 7.6.1 lists the measured efficiency of each cut and the correction, if any. The other cuts matched within errors, and so are measured directly from the simulation. The measured correction for the underlying energy in events with

multiple interactions is determined and used throughout the analysis. The final correction to the photon isolation efficiency in the detector simulation of W events for is shown in the follow equation.

$$E_T < 20.0 GeV \quad , \quad Corr_{Iso} = 0.884 + 0.0178 E_T^{\gamma} - 0.00102 E_T^{\gamma 2} + 0.00002 E_T^{\gamma 3}$$

$$E_T > 20.0 GeV \quad , \quad Corr_{Iso} = 0.994 \tag{7.14}$$

$$\tag{7.15}$$

Cut	$W \to e\nu$ Simulation	$W \to e\nu$ Data	Correction	Error
Cal Iso	91.9%	90.3%	F(E_T)	1.0%
N3D & P_T	99.6%	99.7%	None	0.3%
Track Iso	98.1%	98.0%	None	0.1%

Table 7.6: The measured efficiencies of various photon ID cuts in simulation and data. The measured correction is listed along with the error.

7.6.2 Photon Shower Shape Efficiency

The shower quality cuts for a photon require a well-reconstructed electromagnetic cluster. The efficiency to pass these cuts is measured using clean electron samples. Since electrons and photons shower purely through electromagnetic processes, the shower development in the calorimeter should be very similar. This assumption is confirmed by comparing single photon and electron samples in simulated data. To be sensitive to the entire E_T spectrum, electron samples are collected in pair production from photon conversion and from the decay of a Z boson. The ratio of the efficiency of shower shape cuts in data and simulation is found to be 0.960 $\pm$

0.025 and the simulation is corrected by this factor to match the data. The details of the determination of this correction factor are presented below.

Conversion Electron Studies

The photon shower shape efficiency in the low-E_T^γ region is studied using electrons from photon conversion. To avoid biasing the calorimeter information, the conversion electrons are selected solely based upon track quantities. The data sample is collected with a low-E_T electron trigger listed in Table 7.7, while single photon simulated samples were generated with Pythia and the detector simulation.

To identify a photon conversion, the following cuts were applied to the low-E_T electron sample. The event is required to contain more than two central electromagnetic clusters, where the tracks matched to the clusters are oppositely charged. The separation of these two tracks must be small, with $\Delta \cot \theta$ <0.03, and the distance of closest approach in the x-y plane should be smaller than 0.1 cm. In order to ensure that the conversion occurred outside of the SVX but within the COT inner radius, the conversion radius must be within the range, 5 cm < r_{conv} < 42 cm. Finally, the two conversion legs are required to extrapolate to different wedges in the calorimeter.

To measure the efficiency, one of the conversion legs is selected randomly, and required to pass the L3 trigger cuts (Table 7.7). The other leg from the conversion is regarded as an unbiased electron and used to measure the shower shape cut efficiency. To minimize the effect of bremsstrahlung, the unbiased electron must have 0.9< E/p <1.1 and must satisfy the photon selection criteria listed in Table 5.5. The isolation, N3D and track isolation cuts are not applied, because most of the second conversion legs fall into the neighboring CES wedges and the cuts would

Table 7.7: Level 3 trigger requirements for ELECTRON_CENTRAL_4 dataset.

ELECTRON_CENTRAL_4 trigger requirement
$E_T \geq 4$ GeV
Track $p_T \geq 4$ GeV
Had/Em ≤ 0.08
Lshr ≤ 0.2
$\chi^2_{strip} \leq 10$
$\chi^2_{wire} \leq 15$
$\Delta X \leq 2$
$\Delta Z \leq 3$

remove real electrons. Instead of isolation cuts, the number of tracks in a cone of 0.4 is required to be less than 3. After selecting one of the electrons from the photon conversion, the efficiency is calculated for the CES χ^2, 2nd CES Strip Energy, and 2nd CES Wire Energy. The results are shown in Table 7.8. The efficiencies are those for the specific selection cut after previous cuts have been applied and are calculated as

$$\epsilon^i = \frac{N^i}{N^{i-1}} \tag{7.16}$$

$Z \to ee$ Studies

The efficiency of the photon shower shape cuts in the high-E_T^γ region is studied using electrons from the decay of Z bosons. The events are selected from the same high-E_T central electron trigger used for the $W\gamma$ analysis. Using the same simulated sample of $Z \to ee$ events generated with Pythia for the electron ID efficiencies was used as a source of unbiased electrons. To select the events, a tight central electron is required in the event, with the second electron leg passing the previously discussed loose electron cuts (Table 7.3). Additionally, to improve the purity of the sample the invariant mass of di-electron is required to be $85 <$ M(e,e) < 95 GeV/c^2, to
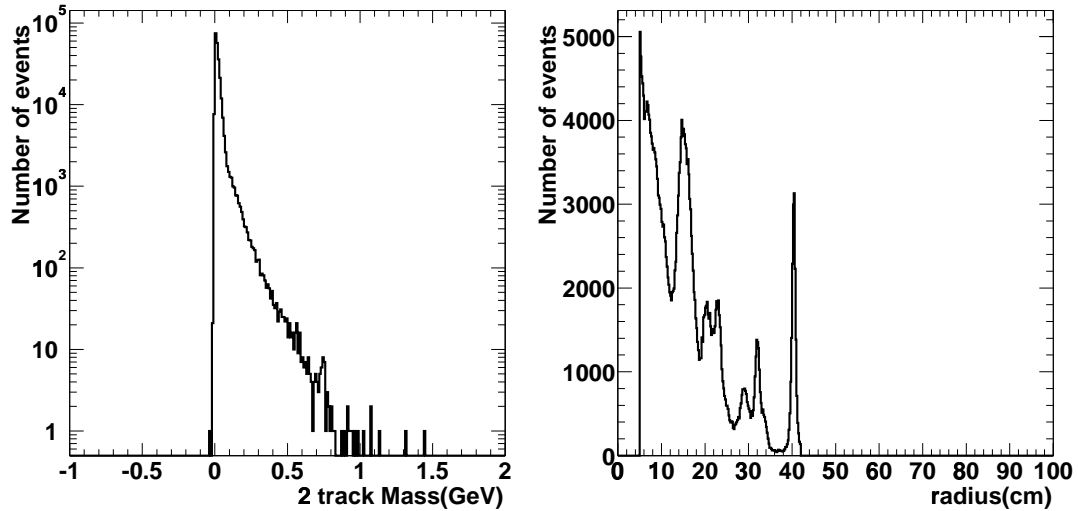
Figure 7.7: The invariant mass of the two conversion tracks, and radius of conversion for the electron pair using 4 GeV triggered electron data.

eliminate background. To avoid jets faking leptons, events containing more than 2 loose electron are removed.

To remove any trigger bias, one electron is randomly selected and required to pass the tight electron cuts as defined in Table 5.2. If it passes, the other electron from the Z decay is regarded as an unbiased electron and used for photon ID efficiency study. Additionally, the unbiased electron should pass $0.9 <E/P< 1.1$ cut to suppress radiative electrons. A modified set of the photon baseline cuts listed in Table 5.5 is applied. As the object of interest is an electron and not a photon, the requirements in Table 5.5 are modified to match an electron from Z decay. The changes are $E_T > 25$ GeV, not 7 GeV, N3D should be ≤ 2, instead of ≤ 1, and the electron track (highest p_T track) is subtracted from the track isolation. Finally, the background from QCD events is subtracted using a same-sign di-electron samples, see ref [53].

After applying the above cuts, the efficiency of the photon shower shape is

defined by

$$\epsilon^i = \frac{N^i(opp) - N^i(same)}{N^{i-1}(opp) - N^{i-1}(same)},\qquad(7.17)$$

where, "opp" means a pair of oppositely charged electrons and "same" is a pair with the same charge. The correction to the shower shape efficiency is the ratio of this efficiency in data and simulation.

$$
\begin{aligned}
Corr_{shower} &= \frac{\epsilon^{data}_{shower}}{\epsilon^{sim}_{shower}} = 0.98 \pm 0.01 \\
&= Corr_{CES\chi^2} \cdot Corr_{2^{nd}CESW} \cdot Corr_{2^{nd}CESS}
\end{aligned}
$$

A correction was calculated for the photon ID cuts on CES χ^2, 2nd CES strip, and 2nd CES wire. The corrections are listed individually in 7.8.

7.6.3 Photon ID Efficiency Summary

The measured cut efficiencies in data and simulation are listed in Table 7.8. The six correction factors applied to the photon ID efficiency in simulation are listed in Table 7.8.

Table 7.8: A summary of the photon ID efficiency correction factors measured between data and simulation that are used to scale the $W\gamma$ signal.

Cut	Min. bias	$Z \to ee(1)$	conv(γ)	Correction
Iso	f(E_T)$\pm$0.01	1.01$\pm$ 0.005	–	f(E_T)$\pm$0.01
N3D	1.0 $\pm$ 0.003	0.977$\pm$ 0.006	–	0.99$\pm$0.01
Trk Iso	1.0 $\pm$ 0.003	0.988$\pm$ 0.005	–	0.99$\pm$0.005
CES χ^2	–	0.980$\pm$ 0.004	1.01 $\pm$ 0.005	0.98$\pm$0.01
2nd CES st.	0.995$\pm$ 0.01	1.00 $\pm$ 0.003	1.01 $\pm$ 0.019	1.01$\pm$0.01
2nd CES wi.	–	0.990$\pm$ 0.004	0.987$\pm$ 0.013	0.99$\pm$0.01

7.7 Photon Conversion Rejection

The photon selection rejects photon conversions to e^+e^- pairs by vetoing tracks matched to the calorimeter CEM cluster. The photon conversion rate measured in the simulation is $10.21 \pm 0.25\%$. However, the material in the version of the simulation used for this analysis is known to be underestimated by about 30%. The amount of material in the inner tracking volume at $R < 42$ cm is $15\%X_0$ in the simulation, while the measured value in data indicates another $4.5 \pm 1.5\%X_0$ is present [55]. Therefore, the true photon conversion probability in the detector is estimated to be $13.3 \pm 1.0\%$. A correction factor is applied to the detector simulation to correct for this additional absorption of photons: $Corr_{conv} = (100 - 13.3)/(100 - 10.2) = 0.97$ with a systematic error of 1.5%.

7.8 $W\gamma \to e\nu\gamma$ Signal Efficiency Summary

The corrections applied to the $W\gamma \to e\nu\gamma$ signal efficiency from the detector simulation are listed in Table 7.9. The corrections are applied to all simulated samples and correct for deviations in detector response between the simulation and data. Using these factors, the number of $W\gamma$ events predicted by the cross section times integrated luminosity is scaled by the product $A \cdot \epsilon_{ID} \cdot \epsilon_{trigger}$. The complete equation for the corrected acceptance and efficiency is shown below. Along with the backgrounds discussed in Chapter 8, this scaled prediction rate gives the complete experimental signal.

$$A \cdot \epsilon = A \cdot \epsilon_{trigger} \cdot \epsilon_{sim} \cdot Corr_{ID}^e \cdot Corr_{ID}^\gamma \cdot Corr_{conv} \qquad (7.18)$$

Table 7.9: Corrections applied to the $W\gamma \to e\nu\gamma$ signal efficiency in the detector simulation. (*) This correction factor depends on E_T: given here is the value excluding the E_T-dependent factor (see 7.14).

Efficiency Correction	Central	Forward
Electron ID	0.964 ± 0.01	0.942 ± 0.02
Track Reconstruction	1.00 ± 0.0	0.986 ± 0.015
Vertex Reconstruction	1.00 ± 0.0	0.965 ± 0.01
γ ID(*)	0.961 ± 0.02	0.961 ± 0.02
γ Conversion rate	0.970 ± 0.015	0.970 ± 0.015

7.9 Luminosity Correction

While the CLC reports the integrated luminosity of the entire $p\bar{p}$ luminous region, the event selection requires the vertex to be reconstructed within the region $|z_{evt}| < 60$ cm. The efficiency for a hard collision to occur within $|z_{vtx}| < 60$ cm and pass this requirement is measured in data. Using data collected with a minimum bias trigger, the z profile of the luminous region is determined from the z_{vtx} distribution as reconstructed from COT tracks only. The calculated ratio of events within 60 cm to the total integral of events is $Corr_{lum} = 0.950 \pm 0.001$. The CLC measured luminosity prediction is then multiplied by this factor to obtain the corrected integrated luminosity for our measured $p\bar{p} \to W\gamma + X$ events.

Chapter 8

Backgrounds to $W\gamma$ Signal

Background contamination to the $W\gamma$ signal comes from both fake electrons and photons and event misreconstruction. The dominant background contribution is W events where an associated quark or gluon jet mimics an isolated photon in the central calorimeter. This background is estimated using a jet $\rightarrow$ photon fake rate calculated using jet data, and then applied to $W + jet$ data. Another source of background is events not fully reconstructed in the detector that mimic the electron-photon-$\not{E}_T$ signature of a $W\gamma$ event. The total background prediction is summarized in Section 8.4 and tabulated in Tables 8.3 and 8.4. The details of each calculation are discussed in the following sections.

8.1   QCD Background

The dominant background to the $W\gamma$ signal is from events where quark or gluon jets fake an isolated photon. The most likely situation in which a jet appears as a photon is when the jet hadronizes to a leading π^0 or ρ meson. The π^0 or ρ then decays to two photons that are highly colinear and produce a tightly clustered signal in the calorimeter similar to a single prompt photon. Additionally, other mechanisms of greater complexity (η or K_s^0 production) can produce a fake photon. Because of the

imprecision of the theoretical modeling of hadronization and the limited capability of the detector simulation, a measurement from simulation is unreliable. In order to be independent of these theoretical uncertainties, the jet $\rightarrow$ photon fake rate is calculated directly from data [49].

The jet $\rightarrow$ photon fake rate is applied to the inclusive W sample to estimate the background contribution from $W + jet$ events. Each jet in the sample is assigned a weight based upon the total transverse energy (electromagnetic + hadronic) of the jet, and an estimated E_T^γ. The sum of these weights gives the number of jet background events. The equation for calculating the number of background events in the $W\gamma$ selection is given by

$$N_{BG}(E_T^\gamma) = \sum_{}^{N_{evt}^W} \sum_{i}^{njets} P_{jet\rightarrow\gamma}^W(E_T^i) \times z(E_T^\gamma, E_T^i) \qquad (8.1)$$

The two sums shown in the equation are: a sum over all events in the data sample containing a W candidate, and a sum over all jets in these W candidate events. $P_{jet\rightarrow\gamma}^W(E_T^i)$ is the probably that a jet produced in a W event will fake an isolated photon. $z(E_T^\gamma, E_T^{jet})$ is a matrix that gives the probability for a jet of energy E_T^{jet} to be measured as a photon of E_T^γ. The determination of these two functions, $P_{jet\rightarrow\gamma}^W(E_T^i)$ and $z(E_T^\gamma, E_T^{jet})$, are the crux of determining the QCD background and will be discussed in detail shortly.

The result of the summation shown in Equation 8.1 is the predicted number of background events as a function of E_T^γ. Integrating over all E_T^γ, the jet background for the central electron selection is 36.1 $\pm$ 11.1 events, and accounts for 27.6% of the candidate events. The jet background for the forward electron selection is 23.4 $\pm$ 7.0 events, which is 36.6% of the candidate events. The fake rate is discussed

first, and then the matrix that transforms between E_T^{jet} and E_T^γ is discussed next.

8.1.1   Jet $\rightarrow \gamma$ Fake Rate

The probability of a jet to fake a photon, $P_{jet\rightarrow\gamma}^{jet}$, is measured in an inclusive jet-triggered data sample. The fake rate is defined simply as

$$P_{jet\rightarrow\gamma}^{jet} = \frac{N_{jet\rightarrow\gamma}}{N_{jet}} \qquad (8.2)$$

Here $N_{jet\rightarrow\gamma}$ is the number of jets passing the isolated photon selection, and N_{jet} is the number of jets considered. It should be noted that this quantity is not strictly the same as the probability that appears in Equation 8.1. Since the measurement is made in a jet-triggered sample, the quark and gluon fraction in the jet sample may vary from the fraction in the W sample. The possible bias from different quark-gluon fractions was explored, and the small deviation was included as a systematic error.

Additionally, the E_T spectrum of the jet samples is compared with the spectrum in W candidate events. Figure 8.1 shows the E_T^{jet} distribution for W data and for the 2nd and 3rd, 4th, 5th etc. ("3-4-5th") highest E_t jet in the jet triggered samples. For the 3-4-5th jet in the jet samples, the E_T^{jet} distribution is very similar to that in the W sample. We thus use the 3-4-5th jet sample for our main result and use the 2nd jet sample for systematics cross checks only.

Unfortunately, the inclusive jet sample contains prompt photons that are produced in the hard interaction. These prompt photons are indistinguishable from a jet faking a photon, and contribute to $N_{jet\rightarrow\gamma}$. Therefore, the simple ratio shown in Equation 8.2 must be corrected for this contribution. The fractional contamination
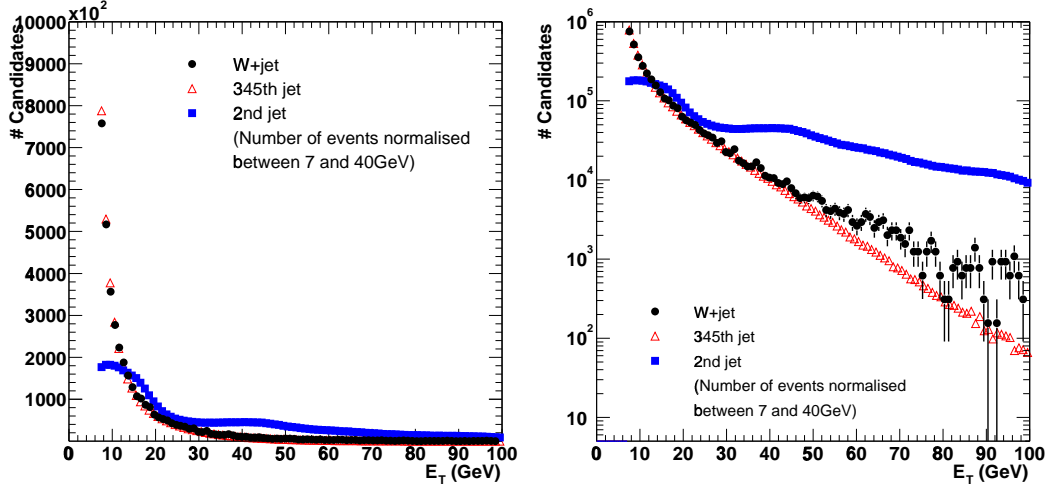
Figure 8.1: The E_T^{jet} distribution for jets in the W sample (black points), the 2nd jet in the jet samples (blue squares) and the 3-4-5th jet in the jet samples (red open triangles).

from prompt photons to the photon candidates in the jet sample is then

$$F_\gamma = \frac{N_\gamma}{N_\gamma + N_{jet \to \gamma}} = \frac{N_\gamma}{N_{\gamma-candidates}} \quad (8.3)$$

And by construction, the definition of the fraction of fake photons from QCD processes is

$$F_{QCD} = \frac{N_{jet \to \gamma}}{N_{\gamma-candidates}} = 1 - F_\gamma \quad (8.4)$$

The jet $\rightarrow$ photon fake rate is now

$$
\begin{aligned}
P^{jet}_{jet\rightarrow\gamma} &= \frac{N_{\gamma-candidates}}{N_{jets}} \times \frac{N_{jet\rightarrow\gamma}}{N_{\gamma-candidates}} \\
&= \frac{N_{\gamma-candidates}}{N_{jets}} \times F_{QCD} \tag{8.5}
\end{aligned}
$$

$$\tag{8.6}$$

Processing the inclusive jet sample selecting isolated central photons gives the two quantities $N_{\gamma-candidates}$ and N_{jets}. The critical component for determining the fake rate is calculating F_{QCD} from the measurement of F_γ and is discussed in detail below.

8.1.2   Determination of F_{QCD}

The fraction of prompt photons in the inclusive jet sample is measured statistically using three independent methods taking advantage of the shower development measurement in the calorimeter. The first method uses the uncorrelated variables *Isolation* and $\chi^2 Mean$ (see discussion in Appendix A) to project the QCD photon background into the signal region. The second uses a weighting procedure calculated from the central shower maximum (CES) detector response. The final method weights each event according to the charge measured in the central preradiator (CPR). The three methods are averaged together and the deviations taken as a systematics. The details of the three methods is discussed below, along with their results and the combination.

$Isolation$ **vs.** $\chi^2 Mean$

This method is designed to project the background rate from a background domi-
nated region into the signal region. This projection is based upon the assumption
that these two variable are not correlated. The two variables were studied in sim-
ulated data and found to be uncorrelated as shown in Figure 8.2. In the two
dimensional plane of $Isolation$ vs. $\chi^2 Mean$, four regions are defined: A, B, C, and
D. The limits of each region are defined in Table 8.1 and can be seen in Figure 8.2.
Assuming that there is no signal in D and that the two observables are uncorrelated,
the background in the signal region is predicted as:

$$N_{BG} = \frac{N_B \cdot N_A}{N_D} \tag{8.7}$$

and thus

$$F_{QCD} = \frac{N_{BG}}{N_C} = \frac{N_B \cdot N_A}{N_D \cdot N_C} \tag{8.8}$$

is the fraction of background in the sample.

Region	$E_T^\gamma > 20$ GeV		$E_T^\gamma < 20$ GeV	
A	$\frac{(Iso-2)}{(20-E_t)} > 0.06$	$\chi^2 Mean < 20$	$Iso/E_t > 0.2,$	$\chi^2 Mean < 20$
B	$\frac{(Iso-2)}{(20-E_t)} < 0.02,$	$\chi^2 Mean > 20$	$Iso/E_t < 0.1,$	$\chi^2 Mean > 20$
C	$\frac{(Iso-2)}{(20-E_t)} < 0.02,$	$\chi^2 Mean < 20$	$Iso/E_t < 0.1,$	$\chi^2 Mean < 20$
D	$\frac{(Iso-2)}{(20-E_t)} > 0.06,$	$\chi^2 Mean > 20$	$Iso/E_t > 0.2,$	$\chi^2 Mean > 20$

Table 8.1: Cut values to define the regions used for the Iso vs. $\chi^2 Mean$ method
for two regions in E_T^γ.
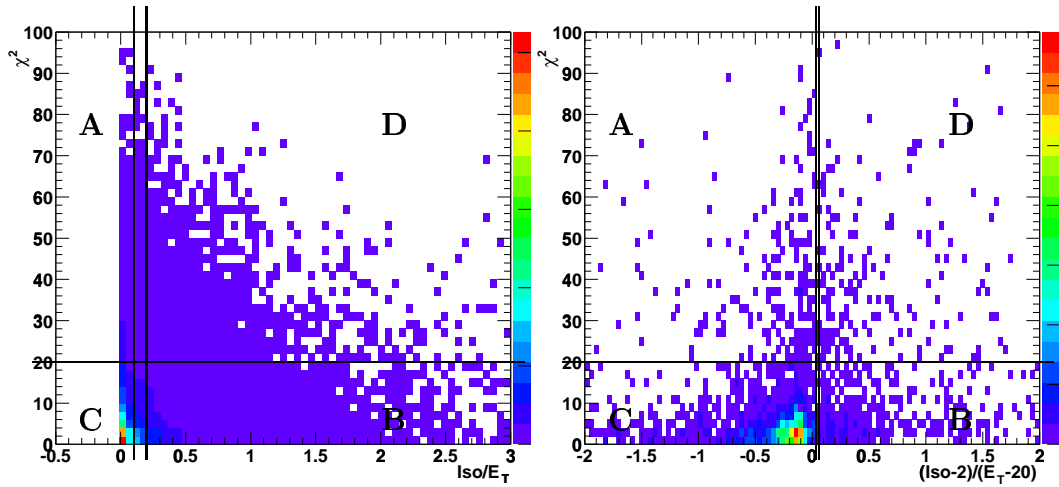
Figure 8.2: Iso/E_t (left) and $(Iso - 2)/(E_T^\gamma - 20)$ versus $\chi^2 Mean$. Illustrated are the four regions A, B, C and D used for determining the QCD background fraction F_{QCD} (see table 8.1)

CES $\chi^2 Mean$ Weighting

The second method of estimating the QCD background fraction, F_{QCD}, is based solely upon the $\chi^2 Mean$ of the photon candidates. For each photon candidate, the average χ^2 fit to the CES response is input into a weighting function. The weight returned from the function is a statistical measure of how photon-like the photon candidate appears in the CES. The weighting function is based upon the fact that the two-photon decay of a meson will have a wider shower profile in the CES, and therefore larger χ^2 when fitted to a single photon profile. The weighting function for the CES is described in detail in [56]. Summing the weight for all candidates gives the fraction of fake photons from QCD processes.

CPR Weighting

Lastly, a calculation of F_{QCD} is performed using the hit rate in the CPR for photon candidates. Similar to the CES based calculation, each photon candidate is assigned a weight for how photon-like it appears in the CPR. The CPR measures the amount of charge produced as the shower traverses the solenoid. For two photon states (*e.g.* the decay of a π_0 or η), the probability of conversion to an electron pair is twice that for a single prompt photon. Thus, the charged particle hit rate distribution for fake photons is higher that for prompt photons. The charge measured in the CPR for each photon candidate is input into a weighting function, and the sum of the weights gives the fraction of fake photons from QCD processes. The details of the CPR weighting function are given in [56].

Each of the three methods for measuring F_{QCD} as a function of E_T^γ are fit to function of the form $\exp(-a \cdot E_T^\gamma + b)$. The parameters of the three fits are

$$Iso \quad : \quad a_{iso} = 0.060, b_{iso} = 0.22 \tag{8.9}$$

$$CES \quad : \quad a_{ces} = 0.037, b_{ces} = 0.18 \tag{8.10}$$

$$CPR \quad : \quad a_{cpr} = 0.068, b_{cpr} = 0.35 \tag{8.11}$$

The final F_{QCD} function used to predict the background is calculated from the average of the three fits and is:

$$
\begin{aligned}
F_{QCD}^{final} &= \exp(-(a_{iso} + a_{ces} + a_{cpr})/3 \cdot E_T^\gamma + (b_{iso} + b_{ces} + b_{cpr})/3) \\
&= \exp(-0.055 \cdot E_T^\gamma + 0.25) \tag{8.12}
\end{aligned}
$$

$$\tag{8.13}$$

The systematic error on the F_{QCD} is taken to be the quadratic sum of the statistical error on the CES method and the maximum deviation to any of the individual methods. The fractional uncertainty of F_{QCD} is about 10% at low E_T^γ values, increasing to an upper limit of 250% of the measured F_{QCD} at $E_T^\gamma = 70$ GeV. While this error appears large, it should be remembered that this uncertainty is on F_{QCD}. After applying this factor to the measured fake rate and convoluting with the jet spectrum in $W + jet$ events, the overall uncertainty of the background is small at high E_T^γ.

The final probability for a jet to fake an isolated photon is show in Figure 8.3. This fake rate is then used to calculate the background from jets faking photons within W events.

8.1.3 E_T^{jet} Fragmentation

. To determine the number of jets as function of E_T^γ, the measured E_T^{jet} value must be translated into a E_T^γ value. In Eq. 8.2, this function is called $z(E_T^\gamma, E_T^i)$ and Figure 8.4 shows the ratio of E_T^{jet} and E_T^γ for photon candidates in simulated data. The distribution is Gaussian with a small tail on the low side. Since the majority of the events are well modeled by a Gaussian distribution, this functional form is used to transform between E_T^{jet} and E_T^γ. The average value 0.934 is set as the center of the gaussian and assign a systematic error of 0.003 for the mean. For the resolution we use 4% and assign a systematic error of 1%. This fitted curve is sampled once for each jet considered, and the returned scale factor multiplied by the E_T^{jet} to give the fake E_T^γ.
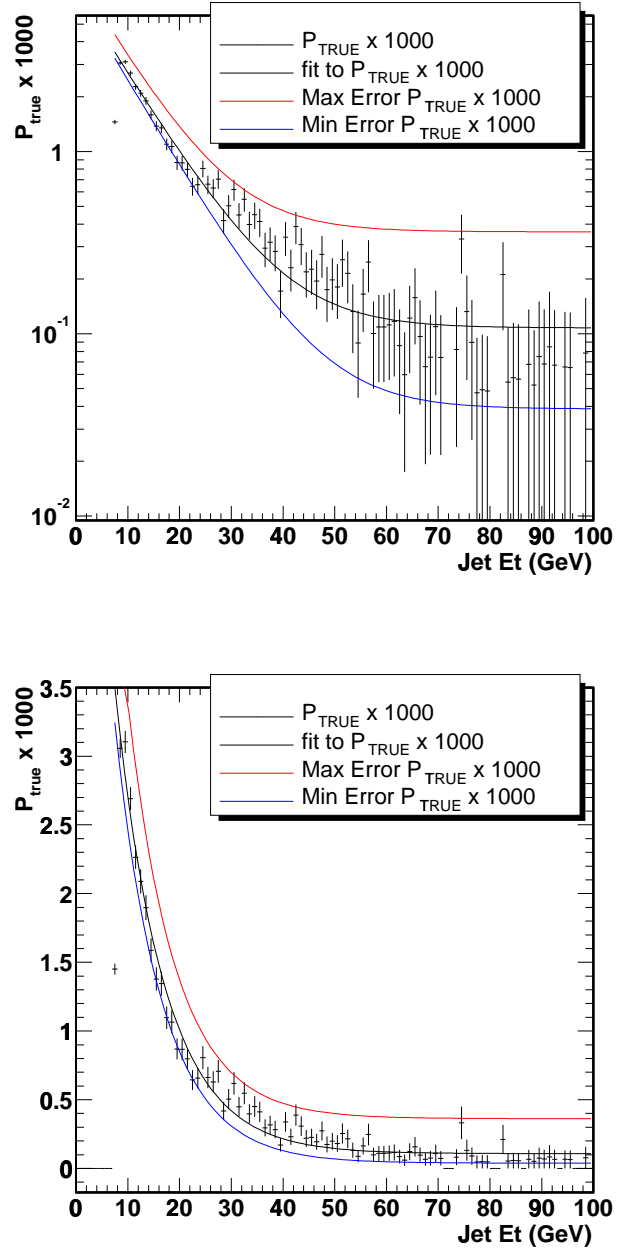
Figure 8.3: The corrected "true" fake rate $P_{jet \to \gamma}(E_T^{jet})$ for the 3-4-5th jet sample. The error-bands due to the choice in F_{QCD} method is shown. The result is shown on a linear (left) and logarithmic scale (right).
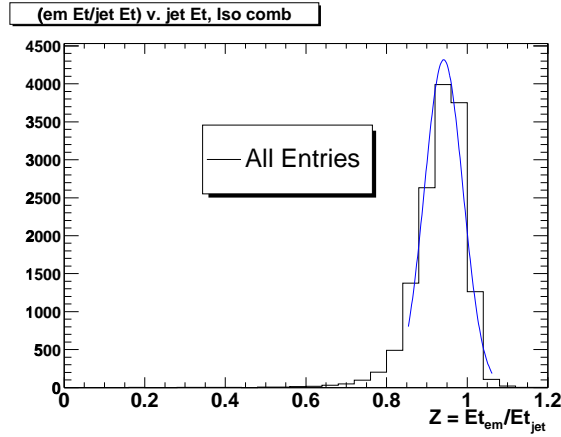
Figure 8.4: The distribution of $Z = E_t^{\gamma}/E_t^{jet}$ for all events in the simulated jet data. Shown is a Gaussian fit to the distributions.

8.1.4 Systematic Error on $Jet \rightarrow \gamma$ Background

The error on the predicted number of $Jet \rightarrow \gamma$ backgrounds event was estimated from five sources (F_{QCD} error, EM Object-based fake rate, quark-gluon fraction, 2nd vs 3-4-5th jet, and fragmentation) and are discussed from largest to smallest. The largest systematic error comes from the determination of the F_{QCD} correction. The difference between the three methods is discussed in the previous section and contributes a fractional error on the fake rate of approximately 20% at low E_T^{jet} rising to 300% at an E_T^{jet} of 70 GeV. Next, the fake rate was calculated using strictly Electromagnetic objects instead of jets to avoid the problem of transforming between E_T^{jet} and E_T^{γ}. This method suffers from significantly limited statistics, and the deviation from the jet determined fake rate of 15% is taken as the systematic error. The difference in the quark-gluon fraction between the inclusive jet sample where the fake rate is measured, and the $W + jet$ sample where the fake rate is applied was measured. The measured fake rate for quarks in simulation is an order of magnitude higher than for gluons. Convoluting this change in the fake rate with

the predicted difference in quark-gluon fraction between the two samples gives a difference in the final fake rate of 20% at an E_T^{jet} of 20 GeV. The fake rate measured in only the 2nd jet sample varies from the fake rate in the 345th jet sample by as much as 40% at E_T^{jet} of 35 GeV. Finally, the fragmentation matrix was varied by the measured resolution and gave an maximal error of 30% at an E_T^{jet} of 30 GeV. The individual errors are combined in quadrature giving a total error on the jet $\rightarrow$ photon fake rate of 30% at E_T^{jet} of 10 GeV and 300% at E_T^{jet} of 70 GeV. The total error and the individual contributions are shown in Figure 8.5.

8.2   Standard Model Backgrounds

Additional background comes from the misreconstruction of other production processes. The two processes considered are $Z\gamma \rightarrow ee\gamma$ and $W\gamma \rightarrow \tau\nu\gamma$. The predicted rate of these backgrounds is calculated using Standard Model predictions.

8.2.1 $Z\gamma \rightarrow ee\gamma$

The production of a $p\bar{p} \rightarrow Z\gamma \rightarrow ee\gamma$ event can mimic the $W\gamma$ signal if one of the final state electrons escapes the detector without reconstruction. The "disappearance" of this final state electron through a crack in the detector will contribute to the missing transverse energy of the event. A $Z\gamma$ event will then be reconstructed as a single lepton, missing transverse energy, and a photon.

The background for this process was measured in simulated data generated with ZGAMMA, following the same procedure as described in Chapter 6. The event selection was applied to the simulation sample, and the predicted amount of background calculated from the measured acceptance rate. The background from $Z\gamma$ for the
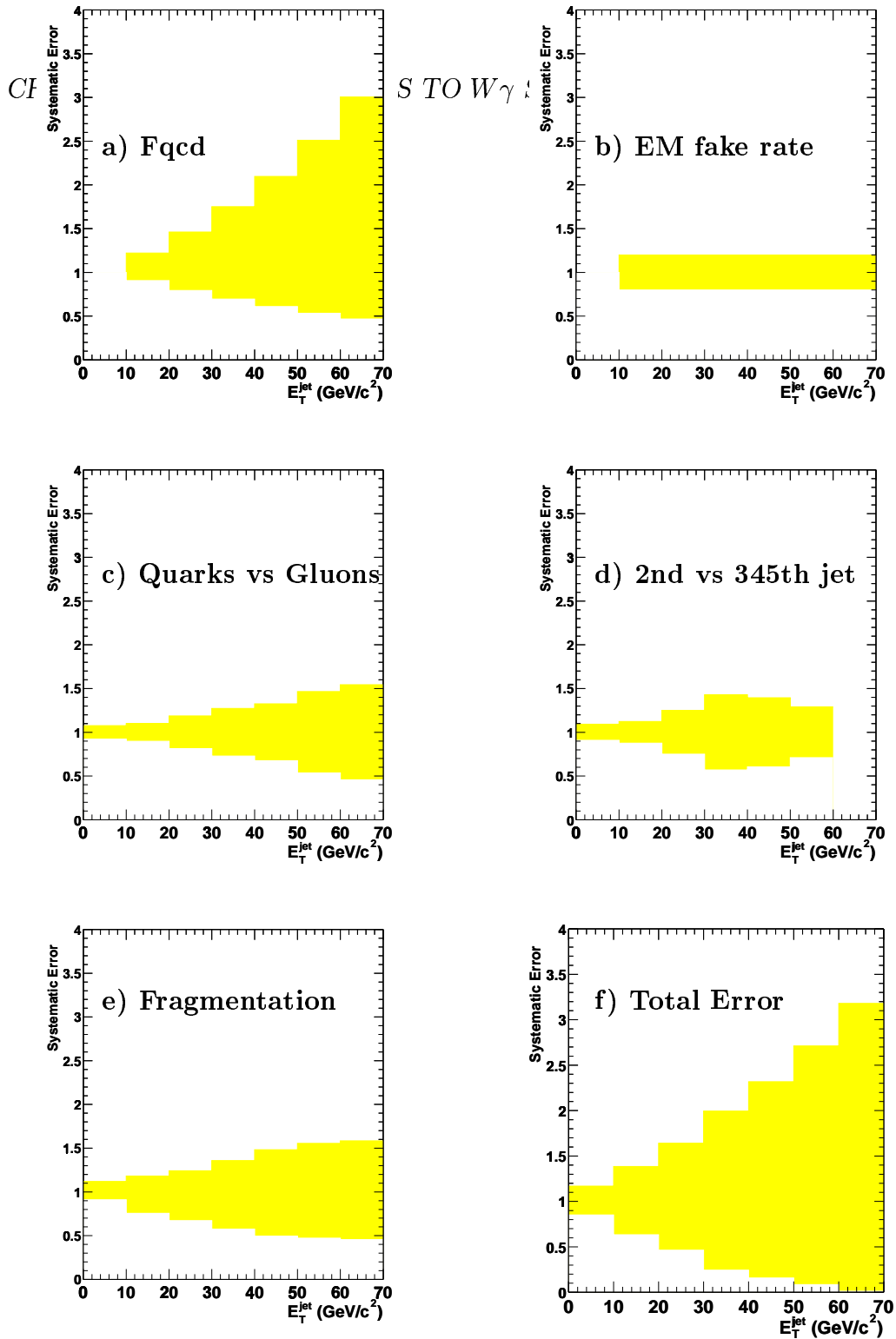
Figure 8.5: Fractional systematic error on the fake rate due to a) the mthod for determining F_{QCD}, b) using EM objects as denominator, c) the difference of between quark and gluon jets, d) the difference between the 2nd and 3-4-5th jet, e) varying the fragmentation and f) the quadratic sum of all those components versus E_T^{jet}.

central region is 5.0 ± 0.32 events, and 1.3 ± 0.1 events in the forward region. In the central region this accounts for 3.8% of the $W\gamma$ candidate events, and 2.0% of the forward $W\gamma$ candidate events.

8.2.2 $W\gamma \to \tau\nu\gamma$

In the production of $W\gamma$ events, the W can decay to a τ and a ν_τ, with the τ subsequently decaying to several particles. While the τ has many hadronic decay channels, the branching ratio for the $\tau \to e\nu_e\nu_\tau$ is considerable at 17.8%. When this decay occurs, the three neutrinos appear as a single missing transverse energy along with the single final state electron. Therefore, if the τ decays with the proper kinematics, a high-P_T electron and high missing transverse energy will be reconstructed in the detector. Fortunately, the phase space for this to occur is rather small, and most of the τ decay products are soft (low-P_T) and fail the kinematic requirements of the event selection.

To determine the background from this process, samples of $p\bar{p} \to W\gamma \to \tau\nu\gamma$ are generated with $W\gamma$, following the same procedure as described in Chapter 6. For these samples, the events are interfaced to the TAUOLA program [48] which performs the decay of the τ leptons. The τ is allowed to decay to all channels in order to assure that all possible fake electron signals are accounted. The background from $W\gamma \to \tau\nu\gamma$ production is calculated to be 0.93 ± 0.16 events in the central, and 0.60 ± 0.11 events in the forward region. This background is 0.71% of the central electron $W\gamma$ candidates, and 0.94% of the forward electron $W\gamma$ candidates.

8.3   Other Backgrounds

While the background from a jet faking a photon dominates, the possibility of a jet faking a W signature is also considered. There are four possible scenarios for the source of the $W\gamma$ signature, and these are shown in Table 8.2. The category "real W + real γ" is the $W\gamma$ signal measured in this analysis, and predicted using the simulated data described in Chapter 6. The application of the jet$\to \gamma$ fake rate described in Section 8.1 uses all W candidates in the data, real and fake. Therefore both the "real W + fake γ" and "fake W + fake γ" categories are accounted for in the measurement of the jet$\to \gamma$ background. This leaves only the background where a real prompt photon is produced in association with a jet, and the jet mimics the signature of a $W \to e\nu$ decay. This background is found to be negligible, and the determination of the upper limit on this background is now discussed.

Table 8.2: The four possible categories of $W\gamma$ candidates in terms of a "fake" or "real" reconstructed particle.

real W + real γ	real W + fake γ
fake W + real γ	fake W + fake γ

To measure the background from fake W, the technique of scaling the measured background from a background dominated kinematic region to the signal region is used. The background is assumed to scale in the same way for the W and $W + \gamma$ samples between the low-$\rlap{\,/}E_T$ and signal regions. Defining the low-$\rlap{\,/}E_T$ region as $\rlap{\,/}E_T < 10$ GeV, and the signal region as $\rlap{\,/}E_T > 25$ GeV, the relation of background events in the different regions is

$$\frac{\#\ \text{fake } W \text{ BG in } W\gamma}{\#\ \text{fake } W \text{ BG in inclusive } W} = \frac{\#\ (W\gamma - (jet \to \gamma)\ \text{BG) at } \rlap{\,/}E_T < 10}{\#\ \text{of inclusive } W \text{ BG at } \rlap{\,/}E_T < 10} \qquad (8.14)$$

The fake W + real γ background is now calculated as

$$N_{fakeW+real\gamma} = \frac{N_A - N_B}{N_C} \times N_D \qquad (8.15)$$

where

- N_A : Events fulfilling $W\gamma$ event selection with $\displaystyle{\not}E_T < {\displaystyle{\not}E_T}^{cut}$ GeV

- N_B : Events fulfilling $W + fake\gamma$ event selection with $\displaystyle{\not}E_T < {\displaystyle{\not}E_T}^{cut}$ GeV

- N_C : Events fulfilling inclusive W event selection with $\displaystyle{\not}E_T < {\displaystyle{\not}E_T}^{cut}$ GeV

- N_D : QCD Background calculated for inclusive W production [44].

The choice of the cut on missing transverse energy, ${\displaystyle{\not}E_T}^{cut}$, was set to several values, 5, 10, and 15 GeV, and the calculated background varied from -0.2 $\pm$ 2.3 to 1.5 $\pm$ 1.4 events. To confirm that this estimate is correct, a large sample of simulated inclusive photon events were analyzed. No events were found to pass the event selection requirement in the central electron or forward electron channel. Therefore, an upper limit of 2.7 events (or 1.38% of $W\gamma$ candidates) at 95% confidence limit was placed on the additional background from fake W + real γ. All indications are that the background is negligible, and so is not included within the predicted event rate calculation.

8.4   Background Summary

The background contribution to the signal is summarized for the central and forward electron channels in Table 8.3 and 8.4. The largest background contribution is events with a W produced in association with a jet that hadronizes to fake a photon,

and is measured with data. The two additional backgrounds from $W\gamma \to \tau\nu\gamma$ and $Z\gamma \to ee\gamma$ were measured from Standard Model predictions. The background is then added to the predicted Standard Model $W\gamma$ signal to give a total experimental signal prediction. This prediction is compared with the data in Chapter 9. Calculating the ratio

$$S/B = \frac{Candidates - Background}{Background} \tag{8.16}$$

the signal-to-background for the central electron selection is 2.23, and for forward electron selection is 1.63.

Table 8.3: The predicted background contribution in events to the experimental signal for central $W\gamma \to e\nu\gamma$ signal. The errors shown are statistical and systematic. The ratio of the background events to the total candidate events is calculated.

Background	Central Electron (events)	BG/Candidates (%)
W+jet	$36.1 \pm 0.10(\text{stat}) \pm 11.1(\text{syst})$	27.6
$Z\gamma \to ee\gamma$	$5.03 \pm 0.19(\text{stat}) \pm 0.26(\text{syst})$	3.8
$W\gamma \to \tau\nu\gamma$	$0.93 \pm 0.15(\text{stat}) \pm 0.05(\text{syst})$	0.71
Total BG	$42.1 \pm 0.3(\text{stat}) \pm 11.3(\text{syst})$	32.1

Table 8.4: The predicted background contribution in events to the experimental signal for forward $W\gamma \to e\nu\gamma$ signal. The errors shown are statistical and systematic. The ratio of the background events to the total candidate events is calculated.

Background	Forward Electron (events)	BG/Candidates (%)
W+jet	$23.40 \pm 0.10(\text{stat}) \pm 7.0(\text{syst})$	36.6
$Z\gamma \to ee\gamma$	$1.31 \pm 0.10(\text{stat}) \pm 0.1(\text{syst})$	2.0
$W\gamma \to \tau\nu\gamma$	$0.60 \pm 0.10(\text{stat}) \pm 0.04(\text{syst})$	0.94
Total BG	$25.3 \pm 0.17(\text{stat}) \pm 7.2(\text{syst})$	39.5

Chapter 9

Experimental Results

This chapter discusses the results of the $W\gamma$ selection, the expected signal, and the cross section extracted from the data. Several kinematic distributions from the $W\gamma \to e\nu\gamma$ data sample are compared with theoretical predictions. Additionally, the results of the $W\gamma$ analysis in the muon channel are included to present the complete $W\gamma \to l\nu\gamma$ sample measured at CDF. The $W\gamma \to \mu\nu\gamma$ analysis was done in parallel to the electron analysis and performed by Naho Tanimoto of Okayama University. The details of this analysis can be found in [57].

9.1 Predicted Event Rate

The expected number of $W\gamma$ candidate events is the sum of the predicted signal and background.

$$N_{exp}^{W\gamma} = N_{pred}^{W\gamma} + N_{BG} \tag{9.1}$$

The details of the background calculation are discuss in Chapter 8. The $W\gamma$ signal predicted by the Standard Model is given by:

$$N_{pred}^{W\gamma} = A \cdot \epsilon \cdot \sigma_{gen}^{W\gamma} \cdot \int \mathcal{L} dt \tag{9.2}$$

In equations that follow, the symbol $\mathcal{L}$ will represent the full integrated luminosity, $\int \mathcal{L}dt$. The acceptance and efficiency, $A \cdot \epsilon$, are discussed in Chapter 7. The quoted cross section, $\sigma_{gen}^{W\gamma}$, is the Standard Model cross section for the generated $W\gamma$ sample which is described in Chapter 6. The integrated luminosity is 202 pb^{-1} for the central electron sample, and 168 pb^{-1} for the forward electron sample. The muon analysis is based upon samples of 192 pb^{-1} in the central muon (CMUP) and 175 pb^{-1} in the intermediate muon (CMX). Table 9.1 and Table 9.2 list the number of events predicted from signal and background along with the number of candidate events seen in the data.

Table 9.1: Expected and observed numbers of events in the $W\gamma \to e\nu\gamma$ analysis for central and plug electrons. Given are the statistical and the experimental systematic error. A separate error of 6% on predictions from generated samples due to error on the luminosity is included in the analysis but not listed in this table.

	Number of Events	
	Central Electron	Forward Electron
$W\gamma \to e\nu\gamma$	$85.5 \pm 1.49(\text{stat}) \pm 4.45(\text{syst})$	$41.1 \pm 1.0(\text{stat}) \pm 2.3(\text{syst})$
$W + jet \to \gamma$	$36.1 \pm 0.10(\text{stat}) \pm 11.0(\text{syst})$	$23.4 \pm 0.10(\text{stat}) \pm 7.0(\text{syst})$
$W\gamma \to \tau\nu\gamma$	$0.93 \pm 0.15(\text{stat}) \pm 0.05(\text{syst})$	$0.6 \pm 0.1(\text{stat}) \pm 0.04(\text{syst})$
$Z\gamma \to ee\gamma$	$5.03 \pm 0.19(\text{stat}) \pm 0.26(\text{syst})$	$1.3 \pm 0.1(\text{stat}) \pm 0.1(\text{syst})$
Total N_{exp}	$127.6 \pm 1.5(\text{stat}) \pm 11.8(\text{syst})$	$66.4 \pm 0.94(\text{stat}) \pm 7.3(\text{syst})$
Data	131	64

In all channels, a total of 323 $W\gamma$ candidates are found in the data sample. The expected number of events from signal and background is 336.4 ± 21.3. From these predictions and the number of candidates, the cross section for $W\gamma$ production is calculated.

Table 9.2: Expected and observed numbers of events in the $W\gamma \to \mu\nu\gamma$ analysis for CMUP and for CMX muons. Given are the statistical and the experimental systematic error.

	Number of Events	
	CMUP	CMX
$W\gamma \to \mu\nu\gamma$	$63.6 \pm 1.17(\text{stat}) \pm 3.17(\text{syst})$	$31.60 \pm 0.87(\text{stat}) \pm 1.57(\text{syst})$
$W + jet \to \gamma$	$17.89 \pm 0.10(\text{stat}) \pm 4.90(\text{syst})$	$9.69 \pm 0.10(\text{stat}) \pm 2.63(\text{syst})$
$W\gamma \to \tau\nu\gamma$	$1.44 \pm 0.17(\text{stat}) \pm 0.07(\text{syst})$	$0.86 \pm 0.14(\text{stat}) \pm 0.05(\text{syst})$
$Z\gamma \to \mu\mu\gamma$	$11.72 \pm 0.26(\text{stat}) \pm 0.60(\text{syst})$	$5.62 \pm 0.19(\text{stat}) \pm 0.33(\text{syst})$
Total N_{exp}	$94.66 \pm 1.21(\text{stat}) \pm 6.17(\text{syst})$	$47.78 \pm 0.91(\text{stat}) \pm 2.75(\text{syst})$
Data	93	35

9.2 Cross Section Calculation

The cross section for $W\gamma$ production in the kinematic range $\Delta R(l, \gamma) > 0.7$ and $E_T^\gamma > 7$ is extracted from the predicted and measured number of events. The cross section is given by

$$\sigma^{W\gamma} = \frac{N_{Data} - N_{BG}}{A \cdot \epsilon \cdot \mathcal{L}} \tag{9.3}$$

where N_{Data} is the number of observed events, N_{BG} the number of background events, A the acceptance for this kinematic range and ϵ_{sim} the efficiency in simulated data and corrected to reproduce the data efficiency (see Chapter 7).

With

$$N_{pred}^{W\gamma} = A \cdot \epsilon \cdot \mathcal{L} \cdot \sigma_{gen}^{W\gamma} \tag{9.4}$$

being the expected number of $W\gamma$ events, this simplifies to

$$\sigma^{W\gamma} = \frac{N_{Data} - N_{BG}}{N_{pred}^{W\gamma}} \cdot \sigma_{gen}^{W\gamma} \tag{9.5}$$

for the kinematic range of the generated sample created with the WGAMMA simulation. In order to correct to the kinematic range of the measurement, we scale this equation

by the ratio of the theoretical cross section in the two kinematic regions:

$$\frac{\sigma_{gen}^{W\gamma}(E_T > 7\text{GeV}, \Delta R > 0.7)}{\sigma_{gen}^{W\gamma}(E_T > 5\text{GeV}, \Delta R > 0.2)} = \frac{19.3 \text{ pb}}{44.7 \text{ pb}} = 0.432 \tag{9.6}$$

Thus the cross section in the kinematic range $\Delta R(l, \nu) > 0.7$ and $E_T^\gamma > 7$ GeV is given simply by

$$\begin{aligned} \sigma^{W\gamma} &= \frac{N_{Data} - N_{BG}}{N_{exp}^{W\gamma}} \cdot \sigma_{gen}^{W\gamma}(E_T > 5, \Delta R > 0.2) \cdot \frac{\sigma_{gen}^{W\gamma}(E_T > 7, \Delta R > 0.7)}{\sigma_{gen}^{W\gamma}(E_T > 5, \Delta R > 0.2)} \\ &= \frac{N_{Data} - N_{BG}}{N_{exp}^{W\gamma}} \cdot \sigma_{gen}^{W\gamma}(E_T > 7\text{GeV}, \Delta R > 0.7) \end{aligned} \tag{9.7}$$

$$\tag{9.8}$$

The cross sections results for $\bar{p}p \to W^{\pm}\gamma + X \to l\nu\gamma + X$ are

$$\text{Central Elec: } \sigma \times \mathcal{B} = 20.1 \pm 2.6(\text{stat.}) \pm 2.7(\text{syst.}) \pm 1.2(\text{lum.}) \text{ pb}$$

$$\text{Forward Elec: } \sigma \times \mathcal{B} = 18.4 \pm 3.8(\text{stat.}) \pm 3.4(\text{syst.}) \pm 1.1(\text{lum.}) \text{ pb}$$

$$\text{CMUP Muon: } \sigma \times \mathcal{B} = 18.8 \pm 2.9(\text{stat.}) \pm 1.8(\text{syst.}) \pm 1.1(\text{lum.}) \text{ pb}$$

$$\text{CMX Muon: } \sigma \times \mathcal{B} = 11.5 \pm 3.6(\text{stat.}) \pm 1.8(\text{syst.}) \pm 0.7(\text{lum.}) \text{ pb}$$

resulting in an average cross section from the electron and muon samples of $\sigma \times \mathcal{B} = 18.1 \pm 1.6(\text{stat.}) \pm 2.4(\text{syst.}) \pm 1.1(\text{lum.})$ pb. The correlations within the systematics errors are fully accounted for when combining the results. The systematic errors and their propagation between electron and muon channels for $W\gamma$ analyses are summarised in Tables 9.3. The theoretical expectation of the cross section is $19.3 \pm 1.4(\text{th.})$ pb. The measured cross section is consistent with the Standard Model prediction.

Table 9.3: Systematic error summary for $W\gamma$. 'x' means that channel needs to take into account its systematic uncertainty.

source	(%)	Central	plug	CMUP	CMX
Jet fake	~30.	x	x	x	x
Z_0 cut eff	1.	x	x	x	x
photon cut eff	2.	x	x	x	x
energy scale(γ)	3.	x	x	x	x
conversion rate uncertainty	1.5	x	x	x	x
momentum scale(μ)	2.			x	x
acceptance	1.	x	x		
acceptance	2.			x	x
central e ID	1.	x			
central e trigger	1.	x			
Energy scale (e)	1.	x	x		
plug e ID	2.5		x		
plug trig e	1.		x		
plug e vertex eff	1.		x		
plug e track eff	1.5		x		
cosmic	0.01			x	x
COT track reconstruction	0.4	x		x	x
CMUP ID	0.7			x	
CMUP reconstruction	0.6			x	
CMUP trigger	0.7			x	
CMX ID	0.8				x
CMX reconstruction	0.3				x
CMX trigger	0.6				x
luminosity	6.	x	x	x	x

The calculation of the $W\gamma$ cross section uses several assumptions based upon the Standard Model. The cross section that is calculated is the cross section for the full W decay phase space, while the candidate events are for lepton and neutrino transverse energies above 25 GeV. As well, the photon selection is limited to the central calorimeter region, $|\eta_\gamma| < 1.1$, while the cross section is extrapolated to the full photon η region. This scaling is calculated from the ratio of cross sections within the selection criteria to the quoted cross section for $E_T^\gamma > 7$ GeV and $\Delta R(l, \nu) > 0.7$. Calculating the ratio of cross sections, the phase space covered by the event selection is 5.3% of the reported cross section phase space.

9.3   Kinematic Distributions

Several kinematic distributions for the $W\gamma$ candidates are compared with the experimental prediction. The central electron candidate events are shown in Figure 9.1, and the forward electron candidate events are shown Figure 9.2. The central electron and forward electron data are plotted separately to demonstrate that the distributions match well in both detector regions. The complete electron and muon data samples are also shown in Figure 9.3. The distributions shown are the photon transverse energy (E_T^γ), lepton-photon separation $(\Delta R(l, \gamma))$, and transverse mass, $(M_T(l, \nu))$. Additionally, the cluster transverse mass, $(M_{CT}(l\gamma, \nu))$, is plotted, but since this is not a standard quantity it will be discussed in detail after the other distributions. In the figures shown, the open histogram is the combined contribution from the Standard Model $W\gamma$ signal and the background. The data is displayed with the statistical error in each bin. Each of the different background sources is shown separately with the largest background contribution coming from the jet→photon prediction.

The photon transverse energy (E_T^γ) and lepton-photon separation $(\Delta R(l, \gamma)$ distributions are sensitive to presence of non-Standard Model physics. As discussed in Chapter 2, if anomalous couplings contribute to $W\gamma$ production, the transverse energy distribution will be enhanced at high values of E_T^γ. The $\Delta R(l, \gamma)$ distribution would also show an enhancement at large lepton-photon separation from non-Standard Model production. If either of these deviations were observed, it would suggest that at least one of the anomalous couplings $(\Delta\kappa, \lambda, \tilde{\kappa}, \tilde{\lambda})$ were non-zero. Such deviations would be evidence of possible Standard Model extensions (*e.g.* W compositeness). The data is in excellent agreement with the Standard Model prediction in both distributions, and there is no evidence for new physics.

As discussed in Chapter 6, the three body invariant mass, $M(l\nu\gamma)$, is effective in distinguishing radiative W decays from the more interesting Wγ production. However, because of the invisiblity of the neutrino, $M(e\nu\gamma)$ can not be determined unambigously in the event reconstruction. The cluster transverse mass [14] M_{CT} is more useful:

$$M_T^2(e\gamma; \not{E}_T) = [(M_{e\gamma}^2 + |\vec{p}_T^{\;\gamma} + \vec{p}_T^{\;e}|^2)^{1/2} + \not{E}_T]^2 - |\vec{p}_T^{\;\gamma} + \vec{p}_T^{\;e} + \not{\vec{E}}_T|^2, \qquad (9.9)$$

where $M_{e\gamma}$ denotes the invariant mass of the $e\gamma$ pair. The cluster transverse mass can also be constructed for the Wγ system by regarding $P_z(\nu)$ as a free parameter and setting it to zero. The cluster transverse mass is plotted versus the transverse mass of the lepton-$\not{E}_T$ system in Figure 9.4. Were an event to be reconstructed completely, the events would be divided between final state radiation and the other production terms. But the distribution shows a continuum of reconstructed cluster transverse mass and transverse mass which indicates how the $P_z(\nu)$ ambiguity affects event reconstruction. This makes separating the candidate events between $u-$,

$s-$, and $t-$channels and the final-state radiation impossible. Instead, the final-state radiation candidates are predominantly clustered around a $M_{CT}(l\gamma, \nu)$ of 80 GeV/c^2, and the other channels distributed at higher $M_{CT}(l\gamma, \nu)$. While complete separation is not possible, the contribution from the $u-$, $s-$, and $t-$channel to the $W\gamma$ sample can be enhanced by requiring that $M_{CT} > 90$ GeV/c^2. This cut is used to reduce the final state radiation contribution in the charge signed rapidity distribution in hopes of distinguishing the $W\gamma$ Radiation Amplitude Zero.

As mentioned in Chapter 2, the charged-signed rapidity distribution is sensitive to the presence of a Radiation Amplitude Zero in the differential cross section of $W\gamma$ production. After requiring that the $M_{CT}(l, \nu) > 90$ GeV/c^2, the charged-signed rapidity for the central electron and muon samples is shown in Figure 9.5. The forward electron sample is excluded from the distribution because the acceptance in the forward detector is shaped to artificially enhance the predicted zero. This sculpting is due to the minimum η separation between a forward electron and central photon. This occurs when the electron has an η of 1.2, and the photon has an η of 1.1, giving a minimum $\Delta\eta$ of 0.1. For this reason, only the central electron and muon samples are included. Unfortunately, the limited statistics of the sample, 71 candidates, make a statement on the presence of a RAZ impossible.

All of the distributions shown for the $W\gamma$ candidates are found to be in excellent agreement with the Standard Model prediction. The agreement of both the measured cross section and kinematic distributions with Standard Model theory gives strong support to the accuracy of the Standard Model in describing the $p\bar{p} \rightarrow l\nu\gamma$ process.
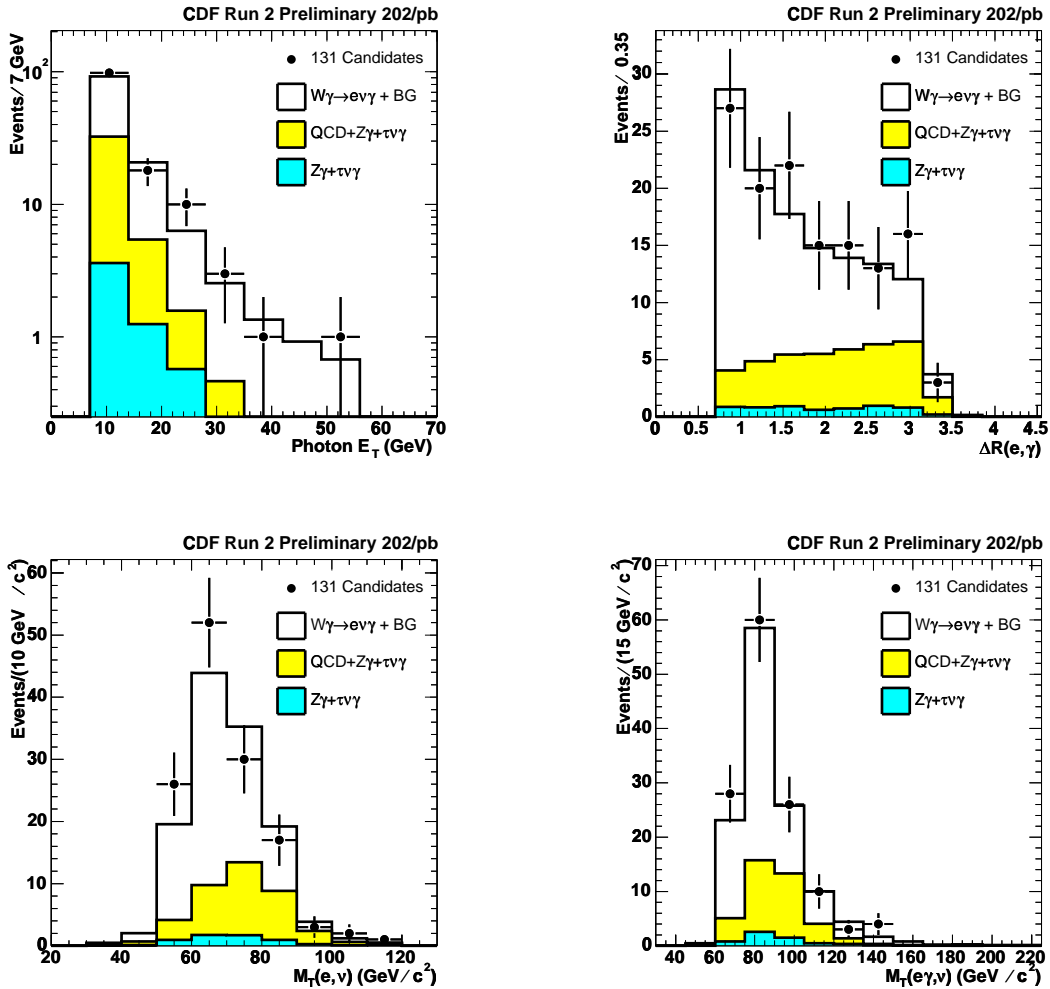
Figure 9.1: Kinematic distributions for the data (points) is plotted along with the Standard Model prediction (histogram) in the $W\gamma \rightarrow e\nu\gamma$ central electron channel. The turquoise histogram is the contribution for $W\gamma \rightarrow \tau\nu\gamma \rightarrow \bar{\nu}\nu\nu e\gamma$ and $Z\gamma \rightarrow ee\gamma$, the yellow the sum of all background contributions (QCD, $Z\gamma$ and $W\gamma \rightarrow \tau\nu\gamma$) and the open histogram the sum of the background and the $W\gamma \rightarrow e\nu\gamma$ signal expectation.
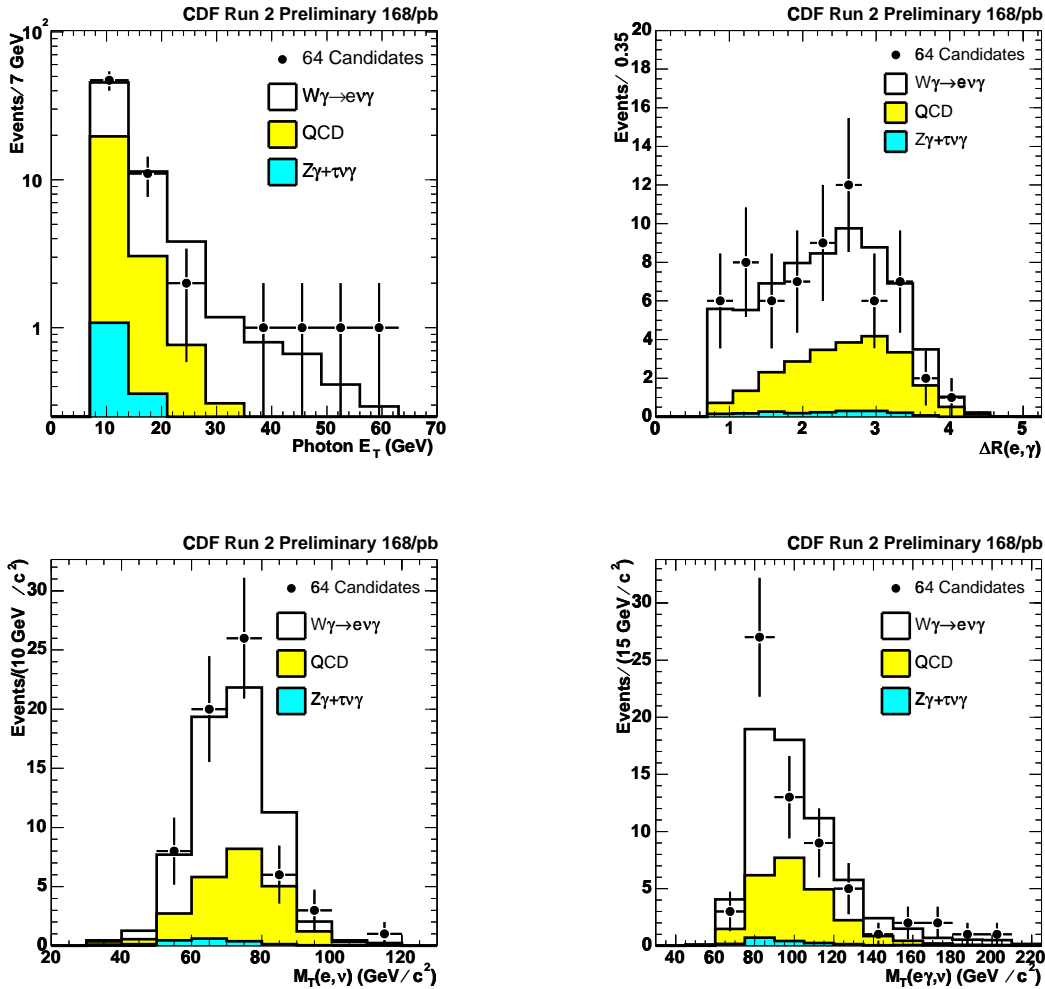
Figure 9.2: Kinematic distributions for the data (points) is plotted along with the Standard Model prediction (histogram) in the $W\gamma \rightarrow e\nu\gamma$ forward electron channel. The turquoise histogram is the contribution for $W\gamma \rightarrow \tau\nu\gamma \rightarrow \bar{\nu}\nu\nu e\gamma$ and $Z\gamma \rightarrow ee\gamma$, the yellow the sum of all background contributions (QCD, $Z\gamma$ and $W\gamma \rightarrow \tau\nu\gamma$) and the open histogram the sum of the background and the $W\gamma \rightarrow e\nu\gamma$ signal expectation.
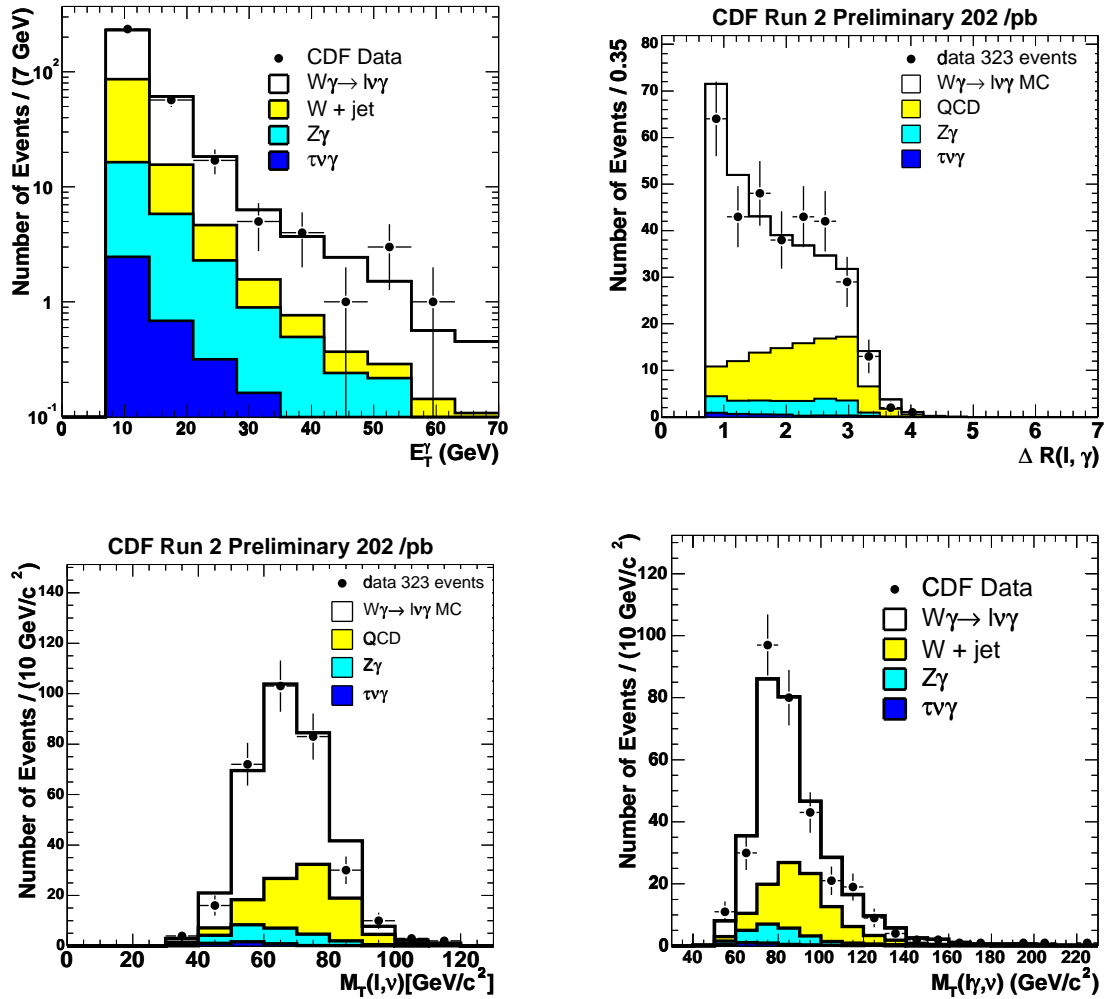
Figure 9.3: Kinematic distributions for the data (points) is plotted along with the Standard Model prediction (histogram) in the $W\gamma \to l\nu\gamma$ channel. The dark blue histogram is the contribution for $W\gamma \to \tau\nu\gamma \to \bar{\nu}\nu\nu l\gamma$, the turquoise the sum of that and $Z\gamma \to ll\gamma$, the yellow the sum of all background contributions (QCD, $Z\gamma$ and $W\gamma \to \tau\nu\gamma$) and the open histogram the sum of the background and the $W\gamma \to l\nu\gamma$ signal expectation.
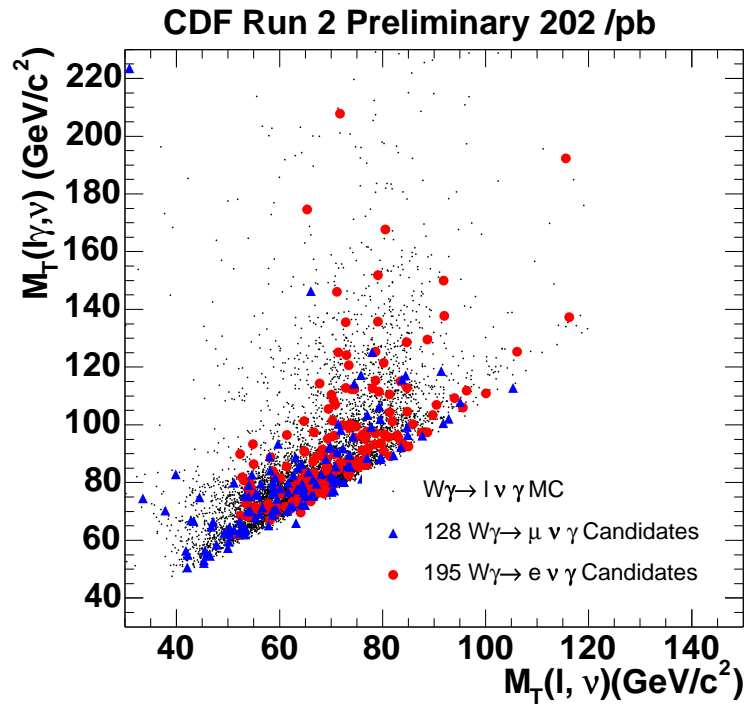
Figure 9.4: The cluster transverse mass $M_{CT}(l\gamma, \nu)$, plotted versus the transverse mass of $W\gamma \to l\nu\gamma$ candidate events. The muon candidate events are shown as blue triangles, and the electron candidate events are shown as red squares. The signal distribution after detector simulation and reconstruction is also shown with the small black dots.
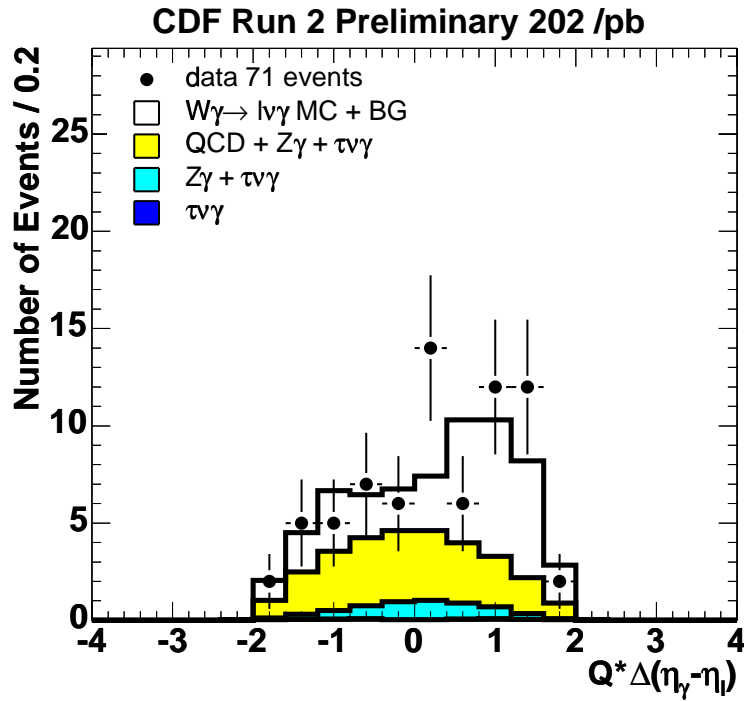
Figure 9.5: The charge signed rapidity difference between the photon and lepton in $W\gamma \to l\nu\gamma$ candidate events. The cluster transverse mass is required to be greater 90 GeV/c^2 in order to enhance the u-, s-, and t-channel $W\gamma$ production. This cut minimizes the contribution from final state lepton radiation (or inner bremsstrahlung) to the charge signed rapidity distribution.

9.4 Cross Section Ratios

The measurement of a cross section is often plagued by large systematic errors. This systematic error arises from the event selection, luminosity measurement, background prediction, and the error in calculating the theoretical predicition. In order to minimize the effect of systematic errors, the practice of measuring ratios of cross section provides a more precise test of theory predictions. In many cases, a systematic error of two measurements will be identical and will cancel in the ratio calculation. Thus, a small overall error may be obtained for both the experimental measurement and the theoretical prediction. A correlated systematic error for two measurements will fluctuate higher or lower in parallel for both measurements. When the two measurements are combined in a ratio, the effect of the possible fluctuation is minimized since the deviations from the true values change symmetrically. Confirming the correlation of the systematic errors and determining the minimized effect is then the crutial part of reducing the error in a cross section ratio measurement.

9.4.1 Ratio of $\sigma(W\gamma)$ to $\sigma(Z\gamma)$

The previously discussed Radiation Amplitude Zero for $W\gamma$ candidates is not directly observable within the current analysis, but the interference and cancelation that creates the RAZ can be seen in the cross section ratio [59]

$$\mathcal{R}_{\gamma,l} = \frac{\mathcal{B}(W \to l\nu) \cdot \sigma(W^{\pm}\gamma)}{\mathcal{B}(Z \to l^+l^-) \cdot \sigma(Z\gamma)} \tag{9.10}$$

The production diagrams for $p\bar{p} \to Z\gamma \to ll\gamma$ are shown in Figure 9.6 and a measurement of the $Z\gamma$ production cross section in Run 2 at CDF has been performed

in parallel to this analysis [58]. The significant difference between $W\gamma$ and $Z\gamma$ production is the lack of a $ZZ\gamma$ vertex. Therefore, the interference and cancelation between the $u-$, $s-$, and $t-$channels in $W\gamma$ production does not occur for $Z\gamma$. The ratio of the $Z\gamma$ and $W\gamma$ cross sections is then sensitive to the cancelation in the $W\gamma$ system. When the ratio $\mathcal{R}_{\gamma,l}$ is compared with the theory prediction of the ratio of inclusive Z and W cross sections, the interference becomes evident. (In this analysis, only the ratio of electron selected events will be considered.) The calculated theoretical ratio is $\mathcal{R}_{\gamma,l}^{th} = 4.26 \pm 0.34$. This prediction is calculated using the $W\gamma$ and $Z\gamma$ production calculation discussed in Chapter 6. The 8% error is dominated by parton distribution parameterizations[1] and was determined by Baur, Errede, and Ohnemus [59].
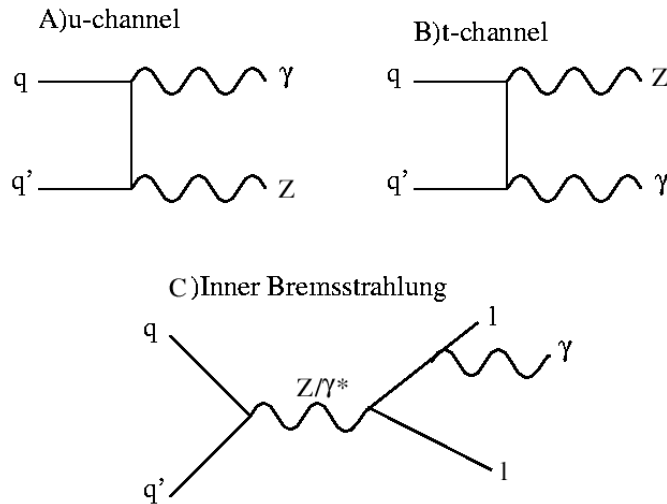
Figure 9.6: The tree level Feynman diagrams for $Z\gamma$ production with the Z decaying to two leptons.

---

[1] The parton distribution parameterizations used to make this measurement are MRSS0, MRSD, GRVLO, MTLO, and D01.1 and details may be found in [59]. While these are not the identical parton distribution functions used for this analysis, the error estimate is expected to still be accurate.

The cancellation of many of the systematic errors in the ratio calculations is either by construction or was confirmed using simulated data samples. The equation for calculating the measured cross section ratio is

$$\mathcal{R}_{\gamma,l} = \frac{N_{cand}^{W\gamma} - BG}{N_{exp}^{W\gamma}} \cdot \frac{N_{exp}^{Z\gamma}}{N_{cand}^{Z\gamma} - BG} \cdot \frac{\sigma_{SM}^{W\gamma}}{\sigma_{SM}^{Z\gamma}} \tag{9.11}$$

The most straightforward systematic to cancel for both ratios is the systematic error on the integrated luminosity. Since the luminosity measurement method for all cross sections is identical, the systematic error on the measurement will always be the same fraction. When calculating the error on the ratio from the luminosity, the error is determined by rescaling the N_{exp} by 6%. But as this scaling affects both the numerator and denominator the same, the luminosity error cancels. A small error does remain due to the contribution of the luminosity error from the Standard Model processes contribution to the $W\gamma$ background. This error though is less than 0.1%, and is neglected.

For $\mathcal{R}_{\gamma,l}$, the largest systematic is the measured jet→photon fake rate and its contribution to the background. Since the same background calculation is used in both analyses, the error on the background is exactly correlated. (*e.g.* if the background is too large, it will be too large by the same rate in both $W\gamma$ and $Z\gamma$) But since the the background fraction in the $W\gamma$ analysis (35%) is larger than in the $Z\gamma$ analysis (12%), the error due to the QCD background is estimate by fluctuating both backgrounds in the same direction. This gave an error on the ratio of 10.0% for a high fluctuation of the background, and 10.2% for a low fluctuation.

For measurements using the central electron $W\gamma$ sample, almost all of the other systematic errors for the two cross sections ($W\gamma$ and $Z\gamma$) are determined from a

single estimation.[2]   These systematics will then also cancel in the ratio as they appear as a scaling of N_{exp} in the numerator and denominator, similar to the luminosity error. The systematics that cancel are: the central electron trigger efficiency, electron identification efficiency, electron energy scale, COT track reconstruction, acceptance, photon identification efficiency, photon energy scale, photon conversion rate, and luminosity scaling ($z0$ cut). The systematics that do not cancel are the forward electron identification (2.5%), and the forward tracking efficiency(1.5%). Table 9.4 lists the sources of systematic error and the cancelation or contribution from each. Added in quadrature, the uncertainty on the central electron selection gives an error on the central cross section ratio of 2.9%.

For the forward electron selected $W\gamma$ sample, the photon related systematics will again cancel. But since the forward electron is the primary selection for the $W\gamma$ candidates, (it is the central electron selection in the $Z\gamma$ selection) the systematic errors on the central electron selection will not cancel. They must be therefore be included in the calculation of the error on the cross section ratio. The systematic errors on the ratio then come from: the central electron trigger efficiency(1%), the central electron identification efficiency(1%), the forward electron trigger efficiency(1%), the forward vertex efficiency(1%), and the COT track reconstruction(0.4%). Table 9.4 lists the sources of systematic error and the cancelation or contribution from each. Combined in quadrature, the error on the forward cross section ratio from the forward electron selection is 2.1%.

Finally, the statistical error on the cross section calculations are completely uncorrelated and must be considered in the error on the ratio (17%). Combining this

---

[2]The event selection of a $Z\gamma$ candidate event is based upon the same tight central electron selection as the $W\gamma$ sample. An additional "loose" central or forward electron is selected as the second decay product of the Z. The same tight central photon selection from the $W\gamma$ analysis is used in the $Z\gamma$ selection.

final error on the ratio with the error from the background estimation (10%) and the event selection error (2.1% or 2.9%) gives the total experimental error on the cross section ratio for $W\gamma$ to $Z\gamma$ to be 23.5%. As the ratio gives asymmetric errors for the different statistical errors, the final error on the ratio is quoted asymmetrically.

Table 9.4: The cancelation of systematic errors in the measurement of $\mathcal{R}_{\gamma,l}$, the ratio of $W\gamma$ to $Z\gamma$ cross sections. An "x" signifies that the systematic error cancels in the ratio, otherwise the percent contribution is listed.

Source	Central electron	Forward electron
Jet Background	x	x
Z_0 cut eff	x	x
Photon cut eff	x	x
Energy scale(γ)	x	x
Conversion rate uncertainty	x	x
Acceptance	x	x
Central e ID	x	1%
Central e trigger	x	1%
Central energy scale (e)	x	0%
Forward e ID	2.5%	x
Forward trig e	0%	1%
Forward energy scale (e)	x	x
Forward e vertex eff	0%	1%
Forward e track eff	1.5%	x
COT track reconstruction	x	0.4%
Luminosity	x	x
Total	2.9%	2.1%

The ratio of the measured cross sections, $\mathcal{R}_{\gamma,l}$, and the Standard Model prediction of the ratio of cross sections is shown in Table 9.5. Excellent agreement with the theoretical prediction is found in both the central and forward event samples. The inclusive W and Z production in $p\bar{p}$ collisions does not contain interference terms as in $W\gamma$ production. Comparing $\mathcal{R}_{\gamma,l}$ to the ratio of inclusive W to inclusive Z cross sections, the large difference in the ratios is apparent and attributed to the

supression of the $W\gamma$ production terms. The agreement between the theoretical prediction and the large difference in the ratio when compared to inclusive production supports the presence of interference among the $W\gamma$ production diagrams.

To improve upon the ratio measurement, the largest improvement will come with additional integrated luminosity since this will quickly reduce the statistical error. The systematic error on the ratio is dominated by the background prediction. This measurement would also be improved by additional integrated luminosity since this would reduce the large error from prompt photon subtraction at large E_T^γ. Unfortunately, there is a limit to the accuracy of the fake rate prediction from the design of the detector and the nature of the fake process. For π^0 and η^0 hadrons with large enough transverse energy, the final state photons will be completely collinear and indistinguishable from prompt photons.

Table 9.5: Cross section ratio for $\sigma_{W\gamma}(E_T^\gamma > 7\text{GeV}, \Delta R_{l,\gamma} > 0.7)$ to $\sigma_{Z\gamma}(E_T^\gamma > 7\text{GeV}, \Delta R_{l,\gamma} > 0.7)$. The ratio is sensitive to the suppression of $W\gamma$ production caused by the interference of the $u-$, $s-$, and $t-$channels. The $Z\gamma$ calculation has no such interference terms making the ratio smaller than the inclusive W to Z ratio. The measured and theoretical prediction for the ratio of inclusive W and inclusive Z production at $\sqrt{s} =$1.96 TeV is shown for comparison [43, 44].

Central $\mathcal{R}_{\gamma,l}$	$4.37^{+0.94}_{-0.87}$
Forward $\mathcal{R}_{\gamma,l}$	$3.96^{+1.1}_{-1.0}$
SM Theory $\mathcal{R}_{\gamma,l}$	4.26 ± 0.34
CDF Run 2 $\frac{\sigma(W)}{\sigma(Z)}$	10.55 ± 0.21
SM Theory $\frac{\sigma(W)}{\sigma(Z)}$	10.90 ± 0.18

9.4.2 Ratio of $\sigma(W\gamma)$ to $\sigma(W)$

The ratio of the $W\gamma$ and inclusive W cross sections is

$$\mathcal{R}_{W\gamma} = \frac{\mathcal{B}(W \to \ell\nu) \cdot \sigma(W^{\pm}\gamma)}{\mathcal{B}(W \to l\nu) \cdot \sigma(W^{\pm})} \tag{9.12}$$

The branching ratios, $\mathcal{B}(W \to \ell\nu)$, in this cross section ratio are identical and independent of any model and cancel exactly by construction. Therefore, this ratio is a more direct measure of the cross sections with fewer theoretical assumptions. While the statistical error in the numerator will not differ from the ratio $\mathcal{R}_{\gamma,l}$, the denominator will have smaller statistical error from the large inclusive W sample.

When calculating the ratio of the $W\gamma$ cross section to the inclusive W cross section measurements, it is the electron selection systematics that cancel to make the ratio measurement more precise than the individual cross section measurements. The large uncertainty on the photon selection and the jet$\to$photon fake rate are not part of the measurement of the inclusive W cross section and therefore will not cancel. Critical to the calculation of the cross section is the estimate of the background. Since the background determinations are drastically different for the $W\gamma$ and inclusive W measurements, the systematic errors for the backgrounds will also not cancel and contributes an error of 13% to the ratio $\mathcal{R}_{W\gamma}$.

Additionally, the systematic errors in the central and forward detector regions are uncorrelated, and for the ratio to be effective in canceling systematic errors these two regions of the detector must be analyzed separately. In the central electron selection, the systematic error attributed to uncertainty in the luminosity scaling (z0 cut), calorimeter energy scaling, COT tracking reconstruction, central trigger efficiency, acceptance, and central electron identification efficiency will cancel. These

cancelations have been confirmed by measuring the effect of fluctuating the source of error in simulated data for both $W\gamma$ and inclusive W samples. In the forward electron sample, the systematic error attributed to uncertainty in the trigger efficiency, luminosity scaling, vertex reconstruction, acceptance, calorimeter energy scale, forward electron identification efficiency, and Phoenix tracking efficiency all cancel. The systematic error on the ratio comes from the error on photon selection, photon conversion rate, photon energy scale, and acceptance. Combing these in quadrature gives an error on $\mathcal{R}_{W\gamma}$ from the photon selection of 4%.

Table 9.6: The cancelation of systematic errors in the measurement of $\mathcal{R}_{W\gamma}$, the ratio of $W\gamma$ to inclusive W cross sections. An "x" signifies that the systematic error cancels in the ratio, otherwise the percent contribution is listed.

Source	Central electron	Forward electron
Jet Background	13%	13%
Z_0 cut eff	x	x
Photon cut eff	2%	2%
Energy scale(γ)	3%	3%
Conversion rate uncertainty	1.5%	1.5%
Acceptance	x	x
Central e ID	x	0%
Central e trigger	x	0%
Central energy scale (e)	x	0%
Forward e ID	0%	x
Forward trig e	0%	x
Forward energy scale (e)	0%	x
Forward e vertex eff	0%	x
Forward e track eff	0%	x
COT track reconstruction	x	0%
Luminosity	x	x
Total	14%	14%

The theoretical calculations for the inclusive W and $W\gamma$ production also have systematic uncertainties that should be considered for cancelation. The largest

source of uncertainty on the theoretical prediction comes from the variation of the parton distribution function. Using the same PDF distribution in the calculation of the inclusive W cross section and $W\gamma$ cross section should allow for a cancelation to occur. When comparing the $\mathcal{O}(\alpha_s)$ calculations for inclusive W production with $W\gamma$ production, the variation from the PDF variation does not exactly cancel as the magnitude of the variations is different. The inclusive W cross section from the CTEQ5M PDF calculation is 2% higher than the calculation from the MRST PDF. In the calculation for the $W\gamma$ production, the variation in the cross section from the choice of PDF is larger (5%) between the CTEQ5M and MRST PDFs. Therefore, a 3% error on the cross section from the choice of parton distribution parameterization remains.

The measured ratios $\mathcal{R}_{W\gamma}$ for the central and forward electron samples are listed in Table 9.7. The measured value has a total systematic error of 14% with the error on the theoretical prediction of 3%. The measured ratio is in excellent agreement with the theoretically predicted ratio. The statistical error again dominates the total error on the ratio and this will improve with greater integrated luminosity. The systematic error is dominated from the error on the background predictions from a jet faking a prompt photon. Improvements on the prediction will come with greater luminosity but the overall accuracy will be limited by the capabilities of the detector.

Table 9.7: Cross section ratio for $\sigma_{W\gamma}(E_T^\gamma > 7\text{GeV}, \Delta R_{l,\gamma} > 0.7)$ to σ_W. The ratio provides a branching independent measure of the production cross sections for the two final states. The theoretical prediction is given using $\mathcal{O}(\alpha_s)$ calculations for $W\gamma$ and inclusive W production at $\sqrt{s} = 1.96$ TeV [38, 43]. The quoted error of 3% comes from the variation of in the ratio from the choice of parton distribution function.

Central $\mathcal{R}_{W\gamma}$	$0.0075^{+0.0015}_{-0.0014}$
Forward $\mathcal{R}_{W\gamma}$	$0.0072^{+0.0019}_{-0.0018}$
SM Theory $\mathcal{R}_{W\gamma}$	0.0074 ± 0.0002

Chapter 10

Summary and Conclusion

A study of the process $p\bar{p} \to W\gamma \to e\nu\gamma$ is presented and compared with the prediction of Standard Model theory. An examination of $W\gamma$ production tests the non-Abelian structure of the $SU_L(2) \times U_Y(1)$ Electroweak theory. Excellent agreement is found in both the measured cross section and kinematic distributions. There is no evidence for new physics in the $p\bar{p} \to l\nu\gamma$ process.

The analysis is based on the ability to efficiently identify the leptonic decay products of the W and then select an isolated photon. The events are triggered using the decay lepton from the W in the central region, and using both the electron and missing transverse energy in the forward region. A W candidate is then reconstructed from tightly selected leptons and corrected missing transverse energy. After selecting a W candidate, a central, isolated photon with $E_T^\gamma > 7$ GeV and well separated from the electron ($\Delta R(\ell, \gamma) > 0.7$) is required.

The data sample is taken from approximately 200 pb^{-1} of proton-antiproton collisions at $\sqrt{s} = 1.96$ TeV produced at the Fermilab Tevatron and recorded with the Collider Detector Facility. Techniques were developed to predict the efficiency of selected $W\gamma$ signal events, and a calculation developed for generating $W\gamma$ events based upon Standard Model predictions. The background from fake photons is estimated using the measured probability for a quark or gluon to be detected as a

163

photon. Additionally, other Standard Model processes are studied for contribution to the $W\gamma$ candidates.

Using these techniques, the $\mathcal{B}(W \to \ell\nu) \cdot \sigma(W\gamma)$ is measured from the selected candidates and compared to the theoretical prediction. The kinematic distributions of the candidate events are also compared with the predicted distributions.

For the kinematic region $E_T^\gamma > 7$ GeV, $\Delta R(\ell, \gamma) > 0.7$, and full W decay phase space, the measured cross section for central electron candidate events is 20.1 ± 3.9 pb. The measured cross section for forward electron candidate events is 18.4 ± 5.2 pb. Combining the W electron decay channel with the W muon decay channel, the measured cross section is 18.1 ± 3.1 pb. Theoretical prediction for the cross section is $\mathcal{B}(W \to \ell\nu) \cdot \sigma(W\gamma) = 19.3 \pm 1.4$ pb. The kinematic distributions of the candidates events are found to be in good agreement with the theoretical prediction.

10.1   Event Selection

The event selection first requires a W candidate in the electron and muon decay channel. Electron events are are required to have $E_T^e > 25$ GeV and $\not{E}_T > 25$ GeV for W selection. For muon events, the lepton and missing transverse energy are required to have $E_T^\mu > 20$ GeV and $\not{E}_T > 20$ GeV. These samples form the base sample for the $W\gamma$ analysis. The initial W selection is validated through the measurement of the inclusive $p\bar{p} \to W + X$ cross section, and excellent agreement is found with Standard Model theory. After finding a W candidate, an isolated photon with $E_T^\gamma > 7$ GeV and $|\eta| < 1.1$ is selected. The photon is required to be separated from the electron in the event ($\Delta R(\ell, \gamma) > 0.7$) to suppress contributions from final state radiation.

10.2   Background

The background to the $\ell - \nu - \gamma$ final state is determined from both Standard Model processes and fake photon candidates. The largest background to the $W\gamma$ signal is the contribution from $W + jet$ events where a leading π^0 or η^0 is produced and reconstructed as a photon candidate. A technique was developed using data to predict the contribution of jets faking photons to the measured event rate. The resulting fake rate for a jet to pass all photon selection cuts is about 0.3% at $E_T = 10$ GeV and decreases exponentially to about 0.07% for $E_T = 25$ GeV. The contribution from the Standard Model processes was calculated from a simulated detector response. The background is determined to be approximately 35% of the expected signal rate.

10.3 $\mathcal{B}(W \to \ell\nu) \cdot \sigma(W\gamma)$ Measurement

To calculate the cross section for $W\gamma$ production, the efficiency and acceptance for signal events is determined using a detailed simulation of the detector. The simulated $W\gamma$ events are compared with data samples to measure a correction to the simulated detector response. The response to isolated photons was a critical step in the efficiency, and several correction applied based upon underlying event, multiple interactions, and additional radiative material in the inner detector. These corrections are applied to generated $W\gamma$ simulation samples to predict the signal event rate.

The Standard Model $W\gamma$ signal prediction is calculated from Uli Baur's $W\gamma$ event generator [11] and then corrected for $\mathcal{O}(\alpha_s)$ contributions. A photon transverse energy dependent correction is applied to the generated events to account for

the initial state QCD contributions. Using this correction, a Standard Model cross section prediction for $p\bar{p} \to W\gamma + X$ production is calculated. This cross section prediction is compared with the measured $W\gamma$ cross section.

The measured cross section for $W\gamma$ production for this kinematic region ($E_T^\gamma > 7$ GeV, $\Delta R(\ell, \gamma) > 0.7$) is $\mathcal{B}(W \to \ell\nu) \cdot \sigma(W\gamma) = 18.1 \pm 3.1$ pb in the combined electron and muon selection channels. The predicted Standard Model cross section is 19.3 $\pm$ 1.4 pb. Several distributions for the $W\gamma$ events were compared to the Standard Model prediction and excellent agreement was observed. The photon transverse energy spectrum is sensitive to new physics in the region $E_T^\gamma > 20$ GeV, but no significant excess is seen in the data. The cluster transverse mass distribution is also sensitive to new physics above the W mass pole and shows no signs of new physics contributions.

The excellent agreement between the measured $W\gamma$ cross section and the predicted value gives support to the accuracy of the Electroweak theory. As well, the cross section ratio of $W\gamma$ to inclusive W production when compared with the ratio of $Z\gamma$ to inclusive Z production shows the suppression of $W\gamma$ events caused by the interference of production terms. The charge-signed rapidity difference distribution lacks the statistics to make a definite statement as to the presence of a Radiation Amplitude Zero, but does within the experimental errors show agreement with the Standard Model prediction. The results of this thesis along with two others have been submitted to Physical Review Letters and should be published shortly.

10.4 Future Prospects

As the Tevatron continues to produce proton-antiproton collisions even larger samples of $W\gamma$ events will soon be available from the CDF detector. With this oppor-

tunity, strong limits on anomalous couplings will be possible that are competitive with the best current limits obtained from the LEP2 experiments. The most exciting result from the Tevatron will be the possible measurement of the Radiation Amplitude Zero. With the future completion of the Large Hadron Collider (LHC) at CERN, even larger samples of $W\gamma$ events will be available for analysis. The production mechanism at the LHC though is dominated by gluon-gluon fusion, and so the currently useful quantity of charge-signed rapidity difference will not show the asymmetry available at the Tevatron. The confirmation of this kinematic distribution would very nicely support the non-Abelian $SU_L(2) \times U_Y(1)$ symmetry of the Standard Model's electroweak theory.

Appendix A

Particle ID Variables

A detailed definition of the variables used to identify central electron, forward electron, and central photon candidates is given below.

A.1 CEM Electron Variables

- E_T^e

  The transverse energy of the electron candidate is $E \times \sin\theta_e$. E is the energy of the two most energetic towers in the calorimeter cluster, and θ_e is the angle at the beam spot of the COT track matched to the seed tower of the CEM cluster.

- Had/Em

  The ratio of the total hadronic to total electromagnetic energy in the calorimeter cluster. For this quantity, all three towers in the CEM cluster are used to calculate the ratio.

- $Isolation$

  The electron isolation is the ratio $E_T^{iso}/E_T^{cluster}$. Here E_T^{iso} is sum of the total energy in a cone of 0.4 centered on the CEM cluster, with the three towers in the CEM cluster excluded from the sum.

- P_T

  The transverse momentum of the electron comes from the COT-only, beam constrained track that is matched to the CEM cluster.

- E/P

  The ratio of the cluster energy to the track momentum. The two tower energy and the COT-only, beam constrained track quantities are used to calculate the ratio.

- $TrackQualityCuts$

  Cuts are applied on the number of segments used to construct the track. This ensures that the track has well constructed 3D information and accurate momentum resolution.

- $CES\ Strip\ \chi^2$

  The CES shower profile is compared with test beam templates for the CES cluster matched to the CEM cluster. The shower profile is only compared in the z direction since bremsstrahlung commonly distorts the ϕ profile. The χ^2 is scaled with an energy dependent factor since the shower profile is known to change with electron $E_T(\text{GeV})$ while the template is based upon single 50 GeV electrons.

$$\chi^2_{corr} = 0.1792 \times 2.11^{ln(E_{elec})}\chi^2 \qquad (A.1)$$

- $CES - Track\ Match$

  The track and CES cluster that are associated with an CEM cluster are compared for consistency. The track is extrapolated beyond the solenoid and out to the radius of the CES detector. The distance between the track and the

CES cluster in both the ϕ and z coordinate is calculated. Since bremsstrahlung has the effect of pulling the CES cluster away from the track trajectory, the ϕ separation is weighted by the charge of the track and also asymmetric.

- *Lateral Shower Shape*

  When an electromagnetic shower deposits energy in the calorimeter, the energy is not expected to be completely contained within a single tower. Instead, the energy is frequently shared across the three towers in the cluster. Test beam data was used to determine an expected sharing between towers for a "true" electromagnetic shower. The lateral sharing function is defined as

  $$L_{shr} = 0.14 \sum_i \frac{E_i^{adj} - E_i^{expected}}{\sqrt{(0.14\sqrt{E})^2 + (\Delta E_i^{expected})^2}} \tag{A.2}$$

  where the sum is performed over only the towers in the cluster with the terms defined as

    - E_i^{adj} is the measured energy in a tower adjacent to the seed tower.

    - $E_i^{expected}$ is the predicted energy in the adjacent tower based upon the parametrized test beam data.

    - $0.14\sqrt{(E)}$ is the error on the energy measurement.

    - $\Delta E_i^{expected}$ is the error on the expected energy from the test beam fit.

- *Fiduciality*

  In order to assure that the particle traverses an active and instrumented region of the detector, fiduciality requirements are applied. The ϕ location of the CES cluster must be within 21 cm of the center of the wedge, and the $|z|$ location

must be between 9 and 230 cm. As well, the seed tower of the cluster must not be located in the highest η tower or in the region containing the solenoid cooling access.

A.2 PEM Electron Variables

- E_T^e

  The transverse energy of the electron candidate is $E \times \sin\theta_e$. E is the energy of the 2×2 tower cluster in the calorimeter, and θ_e is the angle of the Phoenix track matched to the seed tower of the EM cluster.

- Had/Em

  The ratio of the total hadronic to total electromagnetic energy in the 2×2 PEM cluster

- $PEM\ 3 \times 3\ \chi^2\ Fit$

  To ensure that the PEM cluster is consistent with an electron, the energy deposition in the 9 towers centered on the PEM cluster seed tower is fit to electron test beam data. The χ^2 of this fit is used to measure the agreement. The fit is also required to contain at least 1 tower to avoid possible fit divergence and failures.

- $Isolation$

  The electron isolation is the ratio $E_T^{iso}/E_T^{cluster}$. Here E_T^{iso} is sum of the total energy in a cone of 0.4 centered on the electron cluster, with the four towers in the PEM cluster excluded from the sum.

- *PES* 5×9 *Ratio*

  The ratio of the energy measured in the central 5 channels to the energy in the full 9 channels of the PES cluster associated with the PEM cluster. For an electron, the energy should be deposited in the center of the PES cluster, and this removes the multi-particle final states.

- *Phoenix Track*

  The PEM cluster is required to have a matched Phoenix track that has been reconstructed from the matched PES cluster and the event vertex.

A.3 CEM Photon Variables

- E_T^{γ}

  The transverse energy of the photon candidate is $E \times \sin\theta_{\gamma}$. E is the two tower energy of the CEM cluster, and θ_{γ} is the angle defined by the event vertex and the CES cluster location.

- Had/Em

  The ratio of the total hadronic to total electromagnetic energy in the calorimeter cluster. For this quantity, all three towers in the CEM cluster are used to calculate the ratio.

- *Isolation*

  The cluster energy isolation is sum of the total energy in a cone of 0.4 centered on the CEM cluster, with the three towers in the CEM cluster excluded from the sum.

- *Track Isolation*

  The cluster track isolation is the sum of the total transverse momentum of tracks within a cone of 0.4 centered on the CEM cluster, where the $z0$ of the track must be within 5 cm of the event vertex.

- *N3D Tracks*

  The number of reconstructed 3D tracks that are matched to the CEM cluster.

- χ^2 *Mean*

  The CES shower profile is compared with test beam templates for the CES cluster matched to the CEM cluster. The shower profile is only compared in both ϕ and z direction, and the χ^2 of the two views averaged. The averaged χ^2 is scaled with the same energy (GeV) dependent factor used for electron shower profile measurement.

$$\chi^2_{corr} = 0.1792 \times 2.11^{ln(E_{elec})}\chi^2 \tag{A.3}$$

- *2nd CES Energy*

  The energy of the 2nd highest energy CES cluster in the strip and wire views.

Appendix B

Trigger Efficiencies

B.1   Central Electron Trigger Efficiency

As the central electron trigger is the basis of a large number of analyses, the trigger efficiency was performed by several groups within the CDF collaboration. A summary of the results is given here, with more complete details in [52]. The central electron trigger is based upon both calorimeter and tracking quantities, and so the measurement of the efficiency is split between these two systems. The tracking efficiency is measured using a W trigger with no tracking requirements, W_NOTRACK. While the calorimeter efficiencies are measured using data samples collected from muon triggers or prescaled auto-accept triggers. The tracking and calorimeter efficiencies are multiplied together for a total central electron trigger efficiency.

B.1.1   XFT Efficiency

At L1, the central electron trigger requires an XFT track of 8 GeV/c. The trigger efficiency is measured by applying the central event selection, listed in Table 5.2, to the W_NOTRACK trigger sample. After selecting a W candidate event, the L1_XFT_PT8 trigger bit is checked, and the efficiency calculated with Equation

B.1.

$$\epsilon(L1\_XFT\_PT8) = \frac{L1\_XFT\_PT8 \& W\_NOTRACK}{W\_NOTRACK} \tag{B.1}$$

Except for a small dependence upon the η distribution of the electron, the efficiency is independent of kinematic variables, and the integrated L1_XFT_PT8 efficiency is 96.6%.

No additional requirement is made on the tracking at L2, but the efficiency was checked to certify that no errors occurred within the trigger hardware. No such problems were found, and the L2_XFT_PT8 is 100%.

The L3 central electron trigger requires that a 3D track with P_T greater than 9 GeV/c be reconstructed in the COT. Selecting W candidates dataset triggered from the W_NOTRACK trigger, the events are also required to have the passed the L1_CEM_PT8 and L2_CEM16_PT8 triggers to isolate the efficiency at L3 from effects upstream in the trigger. The formula for the L3 tracking efficiency is then given in Equation B.2.

$$\epsilon(L3\_PT9) = \frac{L1\_CEM\_PT8 \& L2\_CEM16\_PT8 \& L3\_CEM18\_PT9}{L1\_CEM\_PT8 \& L2\_CEM16\_PT8} \tag{B.2}$$

No dependence on any kinematic variable is found, and the integrated L3_PT9 trigger efficiency is measured to be 99.6%.

B.1.2 Calorimeter Trigger Efficiency

At L1, the central electron trigger requires a tower with EM $E_T > 8$ GeV, L1_CEM8. Unfortunately, there was no trigger used during the data taking process that used the L1_CEM8 without it being coupled to some other trigger requirement (e.g. track,

$\not{E}_T$, etc.). The L1_EM8 trigger bit is decoupled from other trigger requirements though, and so by requiring minimal activity in the forward calorimeter, the trigger response in the central calorimeter is measured. The control sample was collected using muon triggered events, and the activity in the calorimeter is considered. The energy in the calorimeter towers is combined into the trigger geometry (two physical towers per trigger tower). If an event has a trigger tower with energy greater than 8 GeV, the L1_EM8 trigger bit is checked. The efficiency is found to be 100% for towers with energy greater than 14 GeV, a threshold much lower than the central electron cut of 25 GeV.

The L2 calorimeter trigger requires EM $E_T > 16$ GeV, and its efficiency is measured with a prescaled, auto-accept L2 trigger, L2_PS50_L1_CEM8_PT8. This trigger has the identical path as the central electron trigger with the exception of L2, where no calorimeter requirements are applied. After selecting central W candidates, the efficiency is measured from Equation B.3.

$$\epsilon(L2\_CEM16) = \frac{L2\_CEM16 \& L2\_PS50\_L1\_CEM8\_PT8.}{L2\_PS50\_L1\_CEM8\_PT8.} \qquad \text{(B.3)}$$

The trigger is measured to be 100% efficient within statistical errors for all E_T above 24 GeV, again below the selection cut of 25 GeV.

The L3 central electron trigger efficiency is measured using a sample of lower-E_T, inclusive electron trigger events, ELECTRON_CENTRAL_8. By requiring that the events in the sample have passed the L1 and L2 central electron trigger path, only the effect of the L3 trigger is measured. After selecting central W events, the efficiency is calculated from Equation B.4.

$$\epsilon(L3\_CEM18) = \frac{L3\_CEM18 \& ELECTRON\_CENTRAL\_8}{ELECTRON\_CENTRAL\_8} \qquad \text{(B.4)}$$

Since the full calorimeter reconstruction is performed at L3, the only difference between offline and trigger quantities is the offline calibrations which are no larger than ~10%. The efficiency is therefore expected to be near 100%, and the measured efficiency is found to reach 100% at 23 GeV as suspected.

All of the calorimeter trigger efficiencies are calculated to be 100% for an electron selection with E_T greater than 25 GeV.

The central electron trigger efficiency then comes exclusively from the tracking requirements in the trigger and is measured to be 96.1 ± 1.0%.

## B.2 Forward W Trigger Efficiency

The forward W trigger is based solely on calorimeter quantities, and the control samples collected from prescaled, lower E_T threshold triggers.

At L1, the forward W trigger requires an EM cluster greater than 8 GeV and $\not{E}_T$ in the calorimeter greater than 15 GeV. It is assumed that the EM8 trigger is 100% efficient, and so only the MET15 efficiency is considered at L1. To collect the unbiased sample, a prescaled trigger requiring only a forward electron the was used, PLUG_ELECTRON_20. After selecting events that have passed all of the forward W cuts, the efficiency was measured using Equation B.5. Where if the respective trigger bit was high in an event, it was added to the numerator and/or the denominator.

$$\epsilon(L1\_MET15) = \frac{L3\_MET\_PEM\&PLUG\_ELECTRON\_20}{PLUG\_ELECTRON\_20} \qquad (B.5)$$

The $\not{E}_T$ cut for the W selection was lowered to 15 GeV to measure the trigger turn on effectively, with the results show in Figure B.1. A fit of the form $\epsilon = 1 - ae^{-b\not{E}_T}$

was fit and applied to MC sample.
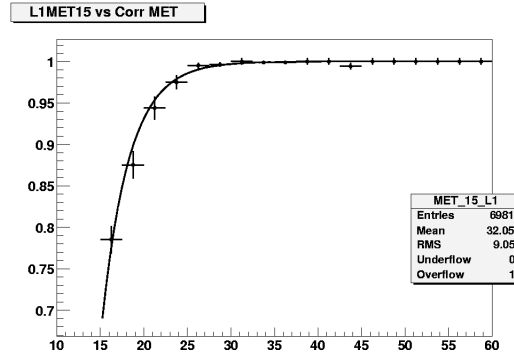
Figure B.1: The L1_MET_15 trigger efficiency as a function of the corrected missing E_T with the form $\epsilon = 1 - 37.8e^{-0.316 E_T}$.

Since the $\not{E}_T$ requirement at L2 does not change from L1, the efficiency between L1 and L2 is 100%. The EM object cut though is raised from 8 GeV to 20 GeV. To measure this efficiency, an unbiased sample was collected using the prescaled trigger, MET_PEM_L1_EM8. This trigger has the same L1 and L3 requirements as the forward W trigger, but no L2 requirements. The only difference between the two triggers is then the L2_PEM20 requirement. Calculating the ratio of events in the MET_PEM sample, to the events in the MET_PEM_L1_EM8_&_MET15 sample gives the efficiency of the L2_PEM20 trigger. Equation B.6 shows the form used.

$$\epsilon(L2\_PEM20) = \frac{L3\_MET\_PEM \& MET\_PEM\_L1\_EM8\_\&\_MET15}{MET\_PEM\_L1\_EM8\_\&\_MET15} \quad (B.6)$$

The E_T cut for the W selection was lowered to study the turn on of the efficiency, and the resulting histogram was fitted using a partial gamma function. Figure B.2 shows the final fit.

The Level3 efficiency of the MET_PEM trigger is the product of the L3_PEM20
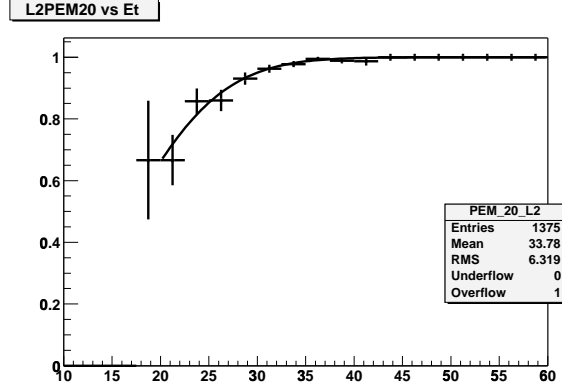
Figure B.2: The L2_PEM_20 trigger efficiency as a function of the EM cluster E_T fitted with a partial gamma function, $\Gamma(55.9, E_T + 38.7)$.

and the L3_MET15 requirement. For the L3_PEM20, there is no change in the cut value from L2, and the efficiency is 100%. But since a reconstructed event vertex is used at L3, the calculated $\not{E}_T$ value can differ from the L2 value and the L3_MET15 must be measured. Using the Level2 MET_PEM requirements and the previously discussed prescaled PLUG_ELECTRON_20 trigger sample, the ratio used to calculate this efficiency is given in Equation B.7. The efficiency for a $\not{E}_T$ cut of 25 GeV is found to be 100%.

$$\epsilon(L3\_MET15) =$$
$$\frac{L3\_MET\_PEM \& PLUG\_ELEC\_20 \& L2\_PEM20\_L1\_EM8\_\&\_MET15}{PLUG\_ELEC\_20 \& L2\_PEM20\_L1\_EM8\_\&\_MET15}$$

With the L3 efficiency 100%, the L1 and L2 efficiencies are combined into a total efficiency given in Equation B.7. Here Γ is the partial gamma function.

$$\epsilon = \epsilon(\displaystyle{\not}E_T)\epsilon(E_T^e) = (1 - 37.8e^{-0.316\displaystyle{\not}E_T})(\Gamma(55.9, E_T + 38.7)) \qquad \text{(B.7)}$$

Then using the measured electron E_T and $\displaystyle{\not}E_T$ of an event, the trigger efficiency is used to reweight the simulated data.

B.2.1 MET_PEM Systematic error

Since the L1_MET15 trigger is so close to an efficiency of 100%, we take half of the inefficiency as the error on the fitted function which gives an error of 0.5%. For the L2_PEM20 trigger systematic error, the same central-plug Z sample used to measure the scaling factors was used to measure the L2_PEM20 efficiency. This is possible since even though the L2_PEM20 trigger is prescaled, the TL2D trigger bank contains the unprescaled trigger bits. An event was considered for the trigger efficiency if it passed the requirements of a CP Z where the plug electron was selected using the tight phoenix electron requirements. The invariant mass of the two electrons was then required to be within $66\,GeV/c^2 < M_{ee} < 106\,GeV/c^2$. If the unprescaled L2_PEM20 bit was high, then the event entered the efficiency profile based upon the corrected E_T of the phoenix electron. The fit shown in Figure B.3 is done with the same function partial gamma function, where the fit results in the function $\Gamma(22.7, E_T + 1.67)$. The difference between the acceptance of W events when the two fitted functions are applied to the an inclusive W Monte Carlo sample is 0.2%. Therefore, we use double this difference, 0.4%, as the systematic error of the L2_PEM20 trigger efficiency. The total trigger efficiency systematic errors is 1.0%.
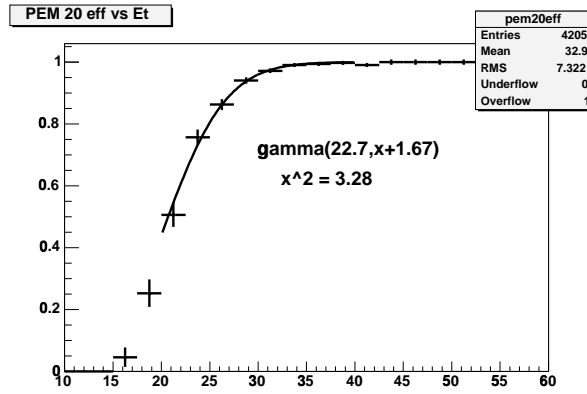
Figure B.3: The L2_PEM_20 trigger efficiency from CP Z candidates as a function of the EM cluster E_T fitted with a partial gamma function, $\Gamma(22.7, E_T+1.67)$.

Bibliography

[1] Ernest Rutherford, Nature, vol 120, p 809, 3 December 1927.

[2] Ernest O. Lawrence and M. Stanley Livingston, "The Production of High Speed Light Ions Without the Use of High Voltages", Phys. Rev. 40, 1935 (1932).

[3] D. H. Perkins, *I*ntroduction to High Energy Physics, Fourth Edition, (Cambridge University Press, Cambridge, UK, 2000), Pp. 242-274.

[4] S. Eidelman *et al.*, Physics Letters B**592**, 1 (2004).

[5] S.L. Glashow, Nucl. Phys. **22**, 579 (1961); A. Salam in *E*lementary Particle Theory, ed. by N. Svartholm (Almqvist and Wiksells, Stockholm, 1968); S. Weinberg, Phys. Rev. Lett. **19**, 1264 (1967).

[6] R. P. Feynman, Phys. Rev. **74**, 939 (1949); J. Schwinger, Phys. Rev. **73**, 416 (1948); S. Tomonaga Phys. Rev. **74**, 224 (1948).

[7] C. N. Yang and R. L. Mills, Phys. Rev. **96**, 191(1954).

[8] F. Halzen and A. D. Martin, *Q*uarks & Leptons: An Introductory Course in Modern Particle Physics, First Edition, (John Wiley & Sons, NY, 1984), Pp. 321-330.

[9] F. Halzen and A. D. Martin, *Q*uarks & Leptons: An Introductory Course in Modern Particle Physics, First Edition, (John Wiley & Sons, NY, 1984), Pp. 170.

[10] S. Eidelman *et al.* "16. Structure Functions", Physics Letters B**592**, 1 (2004).

[11] U. Baur and E.L. Berger, "Probing the $WW\gamma$ vertex at the Fermilab Tevatron Collider", Phys. Rev. D 41, 1476 (1990).

[12] U. Baur, S. Errede, and G. Landsberg. "Rapidity Correlations in $W\gamma$ Production at Hadron Colliders", Phys. Rev. D50, 1917 (1994).

[13] J. C. Wallet, Z. Phys. C **30**, 575 (1986).

[14] E.L. Berger, D. DiBitonto, M. Jacob and W.J. Stirling, "The minimum invariant mass - a technique for heavy quark searches at collider energy", Phys. Lett. 140B, 259 (1984); V. Berger, A.D. Martin and R.J.N. Phillips, "Evidence for the t-quark in $p\bar{p}$ collider data?" Phys. Lett. 125B, 339 (1983).

[15] Doug Benjamin, Ph. D. Thesis (Tufts University), 1993.

[16] ALEPH Collaboration, ALEPH Note 2003-015, CERN Conference Note 2003-011 (2003).

[17] DELPHI Collaboration, DELPHI Note 2003-051, CERN Conference Note 2003-671 (2003).

[18] L3 Collaboration, "Measurement of Triple-Gauge-Boson Couplings of the W Boson at LEP", hep-ex/0402036, 2004.

[19] OPAL Collaboration, "Measurement of charged current triple gauge boson couplings using W pairs at LEP", hep-ex/0308067, 2003.

[20] DELPHI Collaboration, P. Abreu *et al.*, Phys. Letter **B397**, 158 (1997).

[21] The LEP Collaborations, "A Combination of Preliminary Electroweak Measurements and Constraints on the Standard Model", hep-ex/0312023, 2003.

[22] D. Benjamin, "$W\gamma$ and $Z\gamma$ Production at the Tevatron," in 10th Topical Workshop on Proton-Antiproton Collider Physics, edited by R. Raja and J. Yoh, AIP Press p. 370 (1996).

[23] B. Abbott et al., "Studies of WW and WZ production and limits on anomalous WW gamma and WWZ couplings", Phys. Rev. D 60, 072002 (1999).

[24] T. Sjöstransd, L. Lönnbland, S. Mrenna, P. Skands, "Pythia 6.2, Physics and Manual", hep-ph/0108264, LU TP 01-21

[25] D Acosta et. al., "A First Look at the CLC Luminosity Measurements", CDF internal note, 6052, 2002.

[26] J. D. Jackson, "Classical Electrodynamics", John Wiley & Sons, 1999, pg 715.

[27] Robert G. Wagner, "Electron Identification for Run II: Algorithms", Internal CDF Note 5456, 2003.

[28] Andrew Ivanov, Eva Halkiadakis, Andy Hockey, Paul Tipton, " Study of Missing E_T Resolution in the $Z \to \mu^+\mu^-$ Sample, CDF internal note, 6462, 2003.

[29] Chris Hays, Peter Tamburello, Ashutosh Kotwal, Peter Wittich, and Rick Snider, "The COT Pattern Recognition Algorithm and Offline Code", CDF internal note, 6992, 2004.

[30] G. C. Blazey et al., "Run II Jet Physics: Proceedings of the Run II QCD and Weak Boson Physics Workshop". hep-ex/0005012, 2000.

[31] S. Lami, A. Bocci, S. Kuhlmann, G. Latino, "Studies of Jet Energy Resolution",CDF internal note, 5507, 2003.

[32] K. Yasuoka et. al., Nuclear Instruments and Methods, A267 (1984),315.

[33] M. Coca et. al., "A First Look at Run 2 High P_T Electrons", CDF internal note, 5830, 2003.

[34] W.K. Sakumoto and H.S. Budd, "Run II PEM Tower Transverse Response Maps", CDF internal note, 6181, 2003.

[35] Aidan Robson, Giulia Manca, Pete Renton, Greg Veramendi, Young-Kee Kim, "A Measurement of $\sigma \times \text{Br}(Z \rightarrow ee)$ using Run 2 Central and Plug Electrons in 72/pb", CDF internal note, 6642, 2004.

[36] A. Bhatti et al., "Jet Energy Corrections for Run II". CDF internal note, 6565, 2003.

[37] G.P. Lepage, Journ. Comp. Physics 27, 192 (1978).

[38] U. Baur, T. Han and J. Ohnemus,"QCD corrections to hadronic W gamma production with nonstandard W W gamma couplings," Phys. Rev. D **48**, 5140 (1993)

[39] U. Baur, T. Han and J. Ohnemus,"QCD corrections and Anomalous Couplings in $Z\gamma$ Production at Hadron Colliders", Phys. Rev. D **57**, 2823 (1998)

[40] CTEQ Collaboration, J. Huston et al., Eur.Phys.J. C12 **(2000)** 375-392.

[41] "GEANT Detector Description and Simulation Tool", CERN Program Library Writeup W5013, (1994).

[42] J. Pumplin, D.R. Stump, J. Huston, H.L. Lai, P. Nadolsky, W.K. Tung, JHEP **07**, 012 (2002).

[43] A. D. Martin, R.G. Roberts, W. J. Stirling, R. S. Thorne, Eur.Phys. J. **C23**, 73 (2002).

[44] T. Affolder *et al.*, The CDF Collaboration, preprint hep-ex/0406078, submitted to Phys. Rev. Lett.

[45] E.L. Berger, Phys. Lett. **140B**, 259 (1984).

[46] Ulrich Baur, private communication (2002).

[47] S. Frixione, hep-ph/0311223 (2003).

[48] S. Jadach, Z. Was, "The tau deacy library TAUOLA: version 2.4 O(α) QED correctionsin $\tau \rightarrow \mu e \nu \bar{\nu}$ decay modes", Comp. Phys. Commun. 76 (1993) 361 (CERN TH-6793 preprint).

[49] H. Hayward and B. Heinemann, "Update of the Measurement of the Probability of a Jet faking an Isolated photon", CDF internal note, 6838, 2004.

[50] J.Thom, D.Glenzinski, M.Herndon, C.-J.Lin, A.Yagil, "Determination of the Run II COT Tracking Efficiency using the W-No-Track Sample", CDF internal note, 6866, 2004.

[51] D.Glenzinski, P.Merkel, J.Thom, A.Yagil, C.Hill, J.Incandela, C.Mills, N.Lockyer, P.Wittich, P.Savard, R.Tafirout, "Addition of PHX Electrons to the Dilepton Analysis using the Tight Lepton and Isolated Track Sample", CDF internal note, 6787, 2004.

[52] J. Nielsen, L. Tompkins, D. Hoffman, Y.K. Kim, G. Veramendi, "Trigger Efficiencies for High E_T Electrons", CDF internal note, 6234, 2004.

[53] Mircea Coca, Eva Halkiadakis, "Central Electron Identification Efficiencies for the 200 pb^{-1} Run 2 Dataset", CDF internal note, 6262, 2004.

[54] Cigdem Issever, Corrinne Mills, Aidan Robson, Bob Wagner, "Plug Electron Baseline Cuts Defined in Summer 2003 and Cut Efficiencies", CDF internal note, 6789, 2004.

[55] S. Chuang et al., "Estimate of the amount of material in the CDF tracker using high-Pt electrons", internal CDF note, 6573, 2004.

[56] F. Abe et al., The CDF Collaboration, "Prompt photon cross section measurement in p anti-p collisions at $\sqrt{s} = 1.8$ TeV", Phys. Rev. **D 48**, 2998 (1993);

[57] Naho Tanimoto, Ph. D. Thesis, Okayama Univeristy (2004).

[58] Helen Hayward, Ph. D. Thesis, University of Liverpool (2004).

[59] U. Baur, S. Errede, and J. Ohnemus, "Ratios of $W^{\pm}\gamma$ and $Z\gamma$ Cross Sections: New Tools in Probing the Weak Boson Sector at the Tevatron", hep-ph/9304239 (1993).

Biography

Michael Hudson Kirby was born on April 24, 1975 in Seoul, South Korea. He is the second child of David P. and Linda H. Kirby and the younger brother of Jennifer D. Wilson. As a member of an United States Air Force family, he has resided in Seoul, South Korea, San Antonio, TX, Norfolk, VA, Riyadh, Saudi Arabia, Chantilly, VA, Vandenberg, CA, Carlisle, PA, and Bossier City, LA. Michael graduated from Chantilly High School, where he was first introduced to the majesty of physics by Evelyn Euler.

After graduating from high school, Michael attended Virginia Polytechnic Institute and State University where he earned his Bachelor of Science (*cum laude*) in physics in May, 1997. While at VPISU, he received the Robert P. Hamilton Prize and Hugh D. Ussery Scholarship and was a member of $\Sigma\Pi\Sigma$. Michael matriculated to Duke University in the fall of 1997. After completing initial course work, Michael relocated to the suburbs of Chicago, IL in the fall of 1999 to begin work on the upgrade and commissioning of the Collider Detector at Fermilab. In May, 2001, he earned a Master of Arts from Duke University for preliminary work on "$W + \gamma$ couplings at the Tevatron."

Dr. Kirby currently resides in Chicago, IL where he continues to do research in particle physics as part of the D0 collaboration while working for the University of Radboud, Netherlands.